Università degli studi di Padova

Dipartimento di Fisica e Astronomia "Galileo Galilei"

Centre de Nanosciences et de Nanotechnologies - Marcoussis

Corso di Laurea Magistrale in Fisica

Tesi di Laurea Magistrale

Towards a Driven Dissipative Bose-Hubbard Model Simulator with Coupled Polariton Microcavities

Relatore:
Prof. Armando Francesco Borghesani

Relatori Esterni:
Prof. Alberto Amo
Prof. Jacqueline Bloch
Dott. Said R. K. Rodriguez

Laureando: Nicola Carlon Zambon
Matricola: 1103935

Anno Accademico 2015/2016

Contents

Introduction

Back in the fifties, soon after the second world war, electronic computing machines draw increasing interest in the scientific community thanks to their capability to solve problems of unprecedented complexity. In the 1955 milestone article *"Studies of non linear problems"*, E. Fermi, J. Pasta and S. M. Ulam, studied with the MANIAC I computer in Los Alamos labs the dynamics of a linear chain of 64 classical anharmonically coupled oscillators. The simulation highlighted "very little, if any, tendency of equipartition of energy among the degrees of freedom". In his memories Ulam recalls the amazement of Fermi when the first results were plotted and reports Fermi's belief that future fundamental theories may involve nonlinear operators. In absence of closed analytical solution the role of computing machines would have been to lead the physicist where complexity overwhelmed intuition.

In the last fifty years the art of scientific computing grew hand to hand with extraordinary technological improvements and increasing computational power allowing giant steps in the comprehension of nature's complexity. Where a classical Turing machine, like our desktop PC, is well suited to simulate a classical system, a quantum computer is needed to efficiently emulate a quantum system. The core of this idea dates back to 1982 when R. Feynman -with impressive foresight- demonstrated the exponential slowdown of classical boolean algorithms when addressing collective quantum phenomena. This led D. Deutsch to the idea of Universal Quantum Computer in 1985 and to the demonstration in 1996 by S. Lloyd that a quantum computer can be programmed to simulate any local quantum system.

Nowadays an universal quantum computer challenging silicon technology has never been built. While part of the scientific community focus on a bottom-up approach pursuing the search for new Q-bit and Q-gates schemes and works to link them in a quantum network (*Digital Quantum Computing*), another part got interested in *Analog Quantum Emulation*. This latter approach re-

lies on simulating the dynamics of a quantum system of interest with another system that is easier to control and measure. In the last decade various system were successfully implemented such as trapped atoms and ions, superconducting circuit networks and coupled photonic resonators [1]-[2]-[3]-[4].

These systems can emulate some of the most celebrated lattice hamiltonians of manybody quantum physics i.e. Bose-Hubbard [1]-[5] and Heisenberg-Ising ones [6]. In this manuscript we will focus on Bose-Hubbard like systems modeling interacting bosons on a lattice, where a rich phenomenology stems from few fundamental "ingredients": confinement, coupling between sites and on-site interactions. While these requests perfectly fits with ultracold atoms charged in an optical lattice, both superconducting circuits and photonic systems are intrinsically lossy, emulating a more general model recounting for driving and dissipation. This makes these systems complementary to trapped ions or cold atom systems by naturally accessing non-equilibrium physics. Among these photonic systems, cavity polaritons are emerging as a tunable and robust experimental platform.

Polaritons are bosonic quasiparticles arising from the strong coupling of cavity photons and quantum well excitons which can be excited in semiconductor based heterostructures consisting of a Fabry-Peròt Cavity formed by two distributed Bragg reflectors and a spacer embedding a quantum well [7]-[8]. By tuning the energy of a cavity mode in proximity of an optical transition in the quantum well, these two eigenstates may experience energy exchange cycles trough repeated emission and absorption processes. Strong coupling is achieved whether the energy exchange rate exceeds all the losses and the system fundamental excitations can be effectively written in terms of mixed states we call polaritons inheriting properties of both the matter and of the light field. The excitonic component provides effective interactions in the form of a Kerr type χ^3 nonlinearity while the photonic component both provides a way to confine polaritons -if refractive index landscape is engineered- and a probe to measure the system trough its spontaneous emission.

Since their first experimental observation in 1992 exciton-polaritons drew great interest in the scientific community: the polariton states excited in a planar heterostructure can be regarded as a 2D gas of interacting photons with characteristic values of χ^3 much greater than standard nonlinear optical materials. Up to extremely high excitonic densities, polaritons can be treated as bosons with a very low effective mass $\sim 10^{-5}\, m_{e^-}$, inheritance of the cavity photon, thus having large de Broglie wavelength. This allows polaritons to condense [9] and form a macroscopically coherent states in a range of temperatures between few kelvin degrees ad room temperature [10]. Superfluidity [11], topological excitations [12], vortex nucleation [13], solitons [14]-[15], spin Hall effect [16]-[17] and coherent condensate propagation were also observed. Thanks to this rich phenomenology polaritons were given the evocative name of *"Quantum Fluids of Light"*

[8]. Moreover many effects analogue to χ^3 nonlinear optics have been experimentally observed in polariton systems such as optical parametric oscillations [18]-[19]-[20]-[21], squeezing [22]-[23], optical bistability [24] and multistability [25].

Polaritons are intrinsically an out of equilibrium system and all their observables can be measured trough the spontaneous emission since a one to one correspondence between cavity polariton and free space modes is imposed by energy and momentum conservation thanks to the in plane traslational symmetry of the system. Therefore the polariton dynamics can be probed both in real and momentum space and resolved in energy and time by means of optical measurements.

In this manuscript we addressed experimentally the properties of the fundamental building blocks of an analog simulator on a lattice where the sites are embodied by micropillar structures where polaritons get completely spatially confined. The aim of this manuscript is to present gradually all the elements needed to appreciate the two novel results presented hereby:

- We demonstrated that the pillar's on-site Kerr nonlinearity can be tuned by modifying the sample temperature, moreover a semi-empirical but comprehensive theoretical model is presented having the merit of being analytical. This result paves a way to address the intriguing but elusive physics of unconventional photon blockade [26]-[27] which dramatically depends on the absolute value of the nonlinearity.

- We report the first experimental observation of a tunneling-induced parametric instability in the steady state of two coupled micropillars where the interplay of the nonlinearity with the hopping among the two sites triggers a parametric scattering process which resonantly creates a signal and idler field. The interference of the pump, signal and idler fields results in a dynamical self-pulsing of steady state. This preliminary result interestingly suggests a way to generate squeezing and entangled polariton pairs.

CHAPTER ONE is a general introduction to microcavity polaritons. In the first section the physical distinction between the weak and strong coupling is discussed and the consequences of strong coupling on the fundamental excitations of a two-level system are investigated. Exciton-polaritons are mixed light-matter states: the second and third section discuss in detail their properties. The fourth section dedicates to the formal description of the polariton states and the mean field equations describing the polariton dynamics in a planar semiconductor microcavity are derived.

CHAPTER TWO describes the sample fabrication process involving Molecular Beam Epitaxy, Electron Beam Litography and an Inductively Coupled Plasma dry etching. A second part is

devoted to the description of the setup and of the measurement techniques employed in the experiments.
CHAPTER THREE introduces the reader to the experimental characterization of the polariton dispersion in a planar cavity, which is the natural starting point to understand the physics of a confined polariton gas. The second section shows how polariton can be laterally confined in micron-sized pillar structures. The confinement results in a discretization of the polariton states, this discrete level structure can be engineered by tuning the pillar section. In the third section we measure the polariton-polariton interaction constant dependence on the sample temperature.

CHAPTER FOUR is devoted to the rich phenomenology of two coupled pillar structures, which we call a photonic dimer molecule. Both the linear and nonlinear physics of the dimer is experimentally investigated. We show how this simple system can be mapped to a two-site driven-dissipative Bose-Hubbard model. We measure two distinct nonlinear phenomena: the Optical Limiter and Bistable regime. The last section presents the first experimental evidence of a parametrical instability resulting from the interplay of the hopping and nonlinear term in the dimer Hamiltonian.

CHAPTER 1

Light-Matter Coupling

Since it's dawn modern optics demonstrated itself as unique probe of physical phenomena: diffraction and interference of a coherent source can be used to build measurement schemes such as spectrometers and interferometers allowing unprecedented precision. The ever growing perfection of these techniques culminated few month ago in the first measurements of Gravitational Waves from the LIGO-VIRGO experiment [28].

Tough powerful probes, photons manybody physics itself lacks the richness of many other systems because photon photon interactions in vacuum are vanishingly small from NIR to UV light spectrum. Indeed the interaction can be only happen trough virtual lepton pairs excitations $l\bar{l}$ of the vacuum field, but the photon energy for visible light is more than five orders of magnitude smaller than the rest mass of electron-positron pairs (which are the lighter leptons). Therefore the overlap of the electromagnetic field with virtual $l\bar{l}$ vacuum excitations is strongly inhibited. From the Euler-Heisenberg effective Lagrangian the cross-section reads in units of $\hbar = c = 1$

$$\sigma(\gamma\gamma \to \gamma\gamma) \sim \frac{\alpha^4 s^3}{m_l^8} \sim 10^{-41} (\hbar\omega_\gamma)^6 \; barn \tag{1.1}$$

where α is the fine structure constant, s the squared energy in the center of mass and m_l the rest mass for a given lepton excitation. On the contrary, matter interacts at much higher rates both with matter and with light. One can then imagine to take advantage of light-matter interactions to form a mixed state, which may eventually interact with other mixed states trough matter-matter interactions. Such hybrid states result from the strong coupling of light and matter fields which can be pictorically seen as a photon "dressing" a matter excitation.

The essence of strong coupling is energy exchange between a light and matter excitations. However in most of the experimental situations light matter interaction is not a reversible process because the optical transitions couple a two level matter system to a continuum of final states. Once the system has left its initial state the probability of finding it back in its initial state decreases exponentially with time as predicted by the Fermi golden rule [29]. This is the so called *Weak Coupling* regime where the interaction of matter and light can be described within a perturbative approach.

Nevertheless is possible to engineer the free space modes in such a way the emission-absorption process becomes reversible, in these conditions the *Strong Coupling* regime may establish. The prototype system is an atom embedded in a cavity where an optical transition of the atom couples to one of the modes of the cavity in a quasi-resonant fashion. Indeed in this picture the cavity photon can be repeatedly emitted and absorbed by the atom and the probability to find the atom in its initial excited state follows a damped sinusoidal behavior, with a damping time inversely proportional to the cavity quality factor[30]. The system fundamental excitation oscillates between the state $|e,0\rangle$, which have the atom in the excited state but no photons, and the state $|g,1\rangle$ consisting of the atom in the ground state plus one cavity photon. These are usually called *Rabi oscillations* and have a period inversely proportional to the coupling strength g. In this picture the interaction cannot be threaten within a perturbative approach and the fundamental excitations of the system are mixed light matter states.

In 1992 Weisbuch and collaborators [7] achieved the light-matter strong coupling with semiconductor based heterostructures. In particular they embedded a semiconductor quantum well (QW) inside a Fabry-Pérot microcavity, in which one longitudinal optical mode is resonant with the QW excitonic transition.

In this chapter we will first try to make quantitative the above statements on the different coupling regimes. We will discuss a criterion to discern between strong and weak coupling and we will study a simple classical toy model which interestingly contains a lot of physics despite its simplicity: two damped and coupled classical harmonic oscillators (CHOs). Moreover this toy model is a very good starting point to understand the linear dynamics of two coupled polariton microcavities (section 1.1). We will then address the formal description of the bare exciton and cavity photon properties deriving the energy-momentum dispersion relation for these two systems (respectively section 1.2 and 1.3). Finally we will describe the properties of the polariton states deriving the two-mode dispersion relation and the mean field equations capturing the polariton dynamics (section 1.4).

1.1 Weak and Strong Coupling

Two damped coupled harmonic oscillators (CHOs) constitute a simple model where the phenomena related to energy exchange and dissipation can be addressed in an intuitive picture. One expects two different behaviours whether the energy exchange or the dissipation dominates the dynamics of the CHOs leading to different coupling regimes. For two CHOs the discerning elements of weak and strong coupling regimes are three

- the time dynamics of the CHOs shows energy exchange cycles or monotonous exponential decay
- the linear response steady state spectrum of the CHOs is characterized by a single or splitted peak resonance
- the eigenfrequencies of the CHOs cross or anti-cross when the bare oscillators detuning transits zero

from the above traits two different criteria are commonly used to identify the strong coupling regime. The first one [31] is that the frequency splitting in the linear response spectrum ($\propto$ coupling strength) needs to be higher than the sum of the linewidths ($\propto$ loss rates). This criterion is well suited for classical systems where the transition from weak coupling to strong coupling regime has a smooth dependence on the CHOs parameters. A second one [32] defines strong coupling the regime where the energy exchange rate between the two CHOs exceeds the difference between the loss rates. This criterion is good when describing quantum rather than classical oscillators because of the criticality of the transition between weak and strong coupling in open quantum systems. Indeed here the transition is dictated by the convergence radius of the perturbative series expansion of the coupling term as a function of the complex oscillator detuning.

To better understand these features we start from the analysis of classical CHOs dynamics and we move as a second step to the framework of two mode Non-Hermitian Hamiltonian (NHH). We follow the false line of the pedagogical article by S.R.K. Rodriguez in Ref. [33], which is rich of further references and strongly suggested for anyone who wants to deepen the knowledge of this argument.

The simple analysis which follows is both interesting to understand the rich physics of strongly coupled systems in a visual fashion, both sets the fundamental ingredients we will need in the next chapters to describe coupled confined polariton condensates which can be mapped within mean approximation in a nonlinear extension of the CHOs formalism. The linear dynamics of CHOs we address in this chapter is therefore the natural starting point of this work.

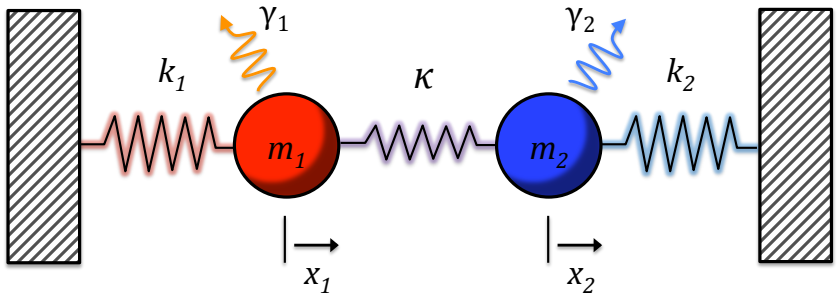

Figure 1.1: Scheme of the two coupled harmonic oscillators, $m_{1,2}$ are the oscillator masses, $k_{1,2}$ and κ respectively the oscillators and coupling spring Hook's constant, $x_{1,2}$ the displacement from equilibrium positions and $\gamma_{1,2}$ the loss rates due to the coupling of the system with the environment

Lets first take the two classical harmonic oscillators depicted in figure 1.1. In absence of an external driving force the Euler-Lagrange equation of motion are

$$\begin{aligned} \ddot{x}_1 + \gamma_1 \dot{x}_1 + \omega_1^2 x_1 - \Omega^2 x_2 = 0 \\ \ddot{x}_2 + \gamma_2 \dot{x}_2 + \omega_2^2 x_2 - \Omega^2 x_1 = 0 \end{aligned} \tag{1.2}$$

where $\omega_j = \sqrt{k_j/m_j}$, $j = 1,2$ are the bare oscillators eigenfrequencies and $\Omega = \sqrt{\kappa/m^*}$ is the coupling rate, m^* the reduced mass of the coupled system. By canonical separation of these two second order ordinary differential equations we can derive a first order system which has the form

$$\dot{q}^j = A_i^j q^i \quad i,j = 1,..,4 \tag{1.3}$$

where we set $q_1 = x_1$, $q_3 = x_2$, $q_2 = \dot{x}_1$, $q_4 = \dot{x}_2$. The 4×4 matrix A has the form

$$A = \begin{pmatrix} 0 & 1 & 0 & 0 \\ -\omega_1^2 & -\gamma_1 & \Omega^2 & 0 \\ 0 & 0 & 0 & 1 \\ \Omega^2 & 0 & -\omega_2^2 & -\gamma_2 \end{pmatrix} \tag{1.4}$$

The time evolution of the system can be easily evaluated if the (eventually generalized) eigenvalues and eigenvectors of the matrix A are known. Indeed from the Volterra integral representation of equation (1.3) for time independent $A_{i,j}$ coefficients it is easy to show that the solution of the Cauchy problem (1.3) with initial conditions $q(0) = q_0$ at the time t is given by the flux $\Phi^t(q_0) = q_0 e^{tA}$. In the simplest case where $A \in M_n(\mathbb{C})$, the group of complex valued $n \times n$ squared matrix, has n independent eigenvalues the exponential matrix can be calculated as

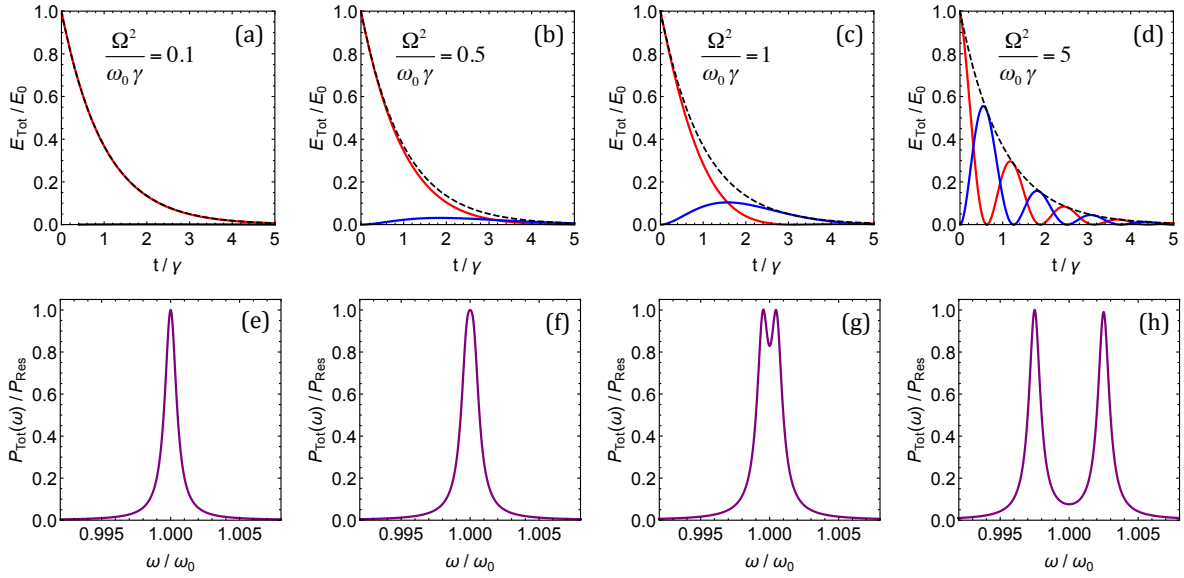

Figure 1.2: (a,b,c,d) shows the evolution of the reduced total energy $E_{Tot}(t)/E_{Tot}(0)$ as a function of the reduced time t/γ. We follow the color-code in figure 1.1 to identify oscillator one, which is initially displaced from its equilibrium and oscillator two. From (a) to (d) we increase the value of the coupling rate Ω, in the figure inset we report the value $\Omega^2/\omega_0\gamma$ which represents the ratio between the loss rate and energy exchange rate. The dotted black curve is the time evolution of the total energy for oscillator one. If we set $\Omega = 0$, in the plot scaled units, this time evolution has the form $e^{-\gamma t}$. The figures (e)-(h) correspond to the steady state power spectrum dissipated by the oscillators when an harmonic force with frequency ω is applied on oscillator one. From (e) to (h) it's possible to observe a smooth splitting of the system resonance, signature of the strong coupling regime.

$$e^{t\mathbf{A}} = \Phi(t)\Phi(0)^{-1} \tag{1.5}$$

if λ_j, $j = 1,..,n$ are the eigenvalues of A and $v_j(\lambda_i)$ is the $j-th$ component of the λ_j-eigenvector, then $\Phi(t)_{i,j}$ is a matrix which elements are $e^{\lambda_i t} v_j(\lambda_i)$. For simplicity we focus on the case where the oscillators parameters are equal, so that $m_1 = m_2 = m^* = m$, $\gamma_1 = \gamma_2$ and $\omega_1 = \omega_2 = \omega$. The four eigenvalues of A are

$$\lambda_i = -\frac{1}{2}\left(\gamma \pm \sqrt{\gamma^2 - 4\omega_0^2 \pm 4\Omega^2}\right) \tag{1.6}$$

The relevant quantity to address the interplay of coupling and damping over time is the total energy of the two oscillators $E_{Tot} = T + V$ where T is the kinetic energy of the oscillator and V its potential energy. We chose $k/m = 1\ rad^2\, s^{-2}$ so that $\omega_0 = 1\ rad\, s^{-1}$ and $\gamma = 10^{-3}\omega_0$, the Cauchy initial conditions are $q_0^{2,3,4} = 0$ and $q_0^1 = q_0$. Within this classical picture some energy has to be externally fed trough the displacement of the first oscillator in order to look at a non-trivial time dynamics, this is no longer true in the quantum picture because there is always non zero energy exchange with the vacuum field.

In figure 1.2 we plot the total energy evolution over time for four different values of the coupling rate Ω. The definition of strong coupling as we said is somehow related to the interplay of energy exchange cycles and losses, when the system energy exchange rate exceeds all the losses we expect in this classical picture a smooth transition to the strong coupling regime. When $\Omega^2 < \omega_0\gamma$ losses dominates the dynamics, indeed in figure 1.2 (a,b) the dynamics of the displaced oscillator (in red) is similar to the dynamics of an uncoupled oscillator ($\Omega = 0$), the energy transfer to the blue oscillator can be regarded as a small perturbative correction on the uncoupled case. As Ω is increased (fig. 1.2 c,d) multiple cycles of energy exchange appear, such cycles are the classical analogue of the so called Rabi oscillation.

Let now see how these considerations on the system dynamics can be linked to Novotny's criterion which relies on the form of the spectral susceptibility. The evaluation of the steady state power dissipated spectrum we need to add an armonic driving term $Fe^{-i\omega t}$ in the equations of motions. Since we are interested in the steady state we can insert the ansatz $x_j(t) = x_j^0 e^{-i\omega t}$ in equation (1.2) which can be proven to be a good solution as soon as $t \gg \gamma^{-1}$. We obtain the following spectral representation of the driven-dissipative CHOs system

$$\begin{pmatrix} \omega_1^2 - \omega^2 - i\gamma_1\omega & -\Omega^2 \\ -\Omega^2 & \omega_2^2 - \omega^2 - i\gamma_2\omega \end{pmatrix} \begin{pmatrix} x_1 \\ x_2 \end{pmatrix} = \begin{pmatrix} Fe^{-i\omega t} \\ 0 \end{pmatrix} \tag{1.7}$$

the solutions of this linear system in the form $Z^i_j x^j = F^i$ can be found by inversion on the matrix Z^i_j, which reads

$$\begin{pmatrix} x_1 \\ x_2 \end{pmatrix} = \frac{1}{det(Z)} \begin{pmatrix} \omega_2^2 - \omega^2 - i\gamma_2\omega & \Omega^2 \\ \Omega^2 & \omega_1^2 - \omega^2 - i\gamma_1\omega \end{pmatrix} \begin{pmatrix} Fe^{-i\omega t} \\ 0 \end{pmatrix} \tag{1.8}$$

and $det(Z) = (\omega_1^2 - \omega^2 - i\gamma_1\omega)(\omega_2^2 - \omega^2 - i\gamma_2\omega) - \Omega^4$. From these spectral solutions, the steady state power dissipated can be calculated as $P_{Tot}(\omega) = \sum P_j(\omega)$, with $P_j(\omega) = \gamma_j\omega^2|x_j(\omega)|^2$. If we focus on the simplest case where oscillators parameters are equal the total power dissipated spectrum has the form

$$P_{Tot}(\omega) = \gamma\omega^2 F^2 \frac{(\omega^2 - \omega_0^2)^2 + \Omega^4 + \gamma^2\omega^2}{\left((\omega^2 - \omega_0^2)^2 + \gamma^2\omega^2\right)^2 - 2\Omega^4\left((\omega^2 - \omega_0^2)^2 - \gamma^2\omega^2\right) + \Omega^8} \tag{1.9}$$

If Ω is set to zero, the above formula reduces to a Lorentzian shaped peak centered on the frequency ω_0 with a full width half-maximum $\Gamma = \gamma\omega$ which is in good approximation equal to $\gamma\omega_0$, since $\omega_0 \gg \gamma$. Since the fourier transform of a Lorentian function is proportional to an exponential function,The quantity $\omega_0\gamma$ represents the loss rate. For $\Omega^2 \gtrsim \gamma\omega_0$ equation (1.9) shows two peaks which maxima have frequency splitting $\approx \Omega^2$. Then the inequality

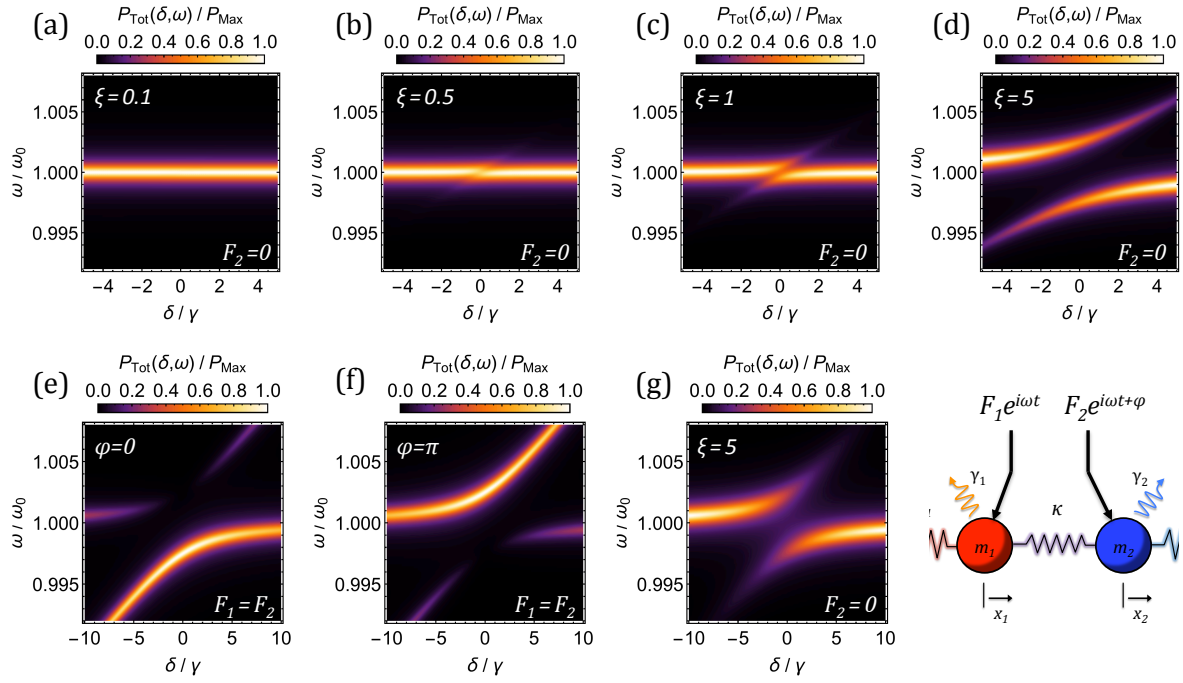

Figure 1.3: Total power absorbed in steady-state by two coupled harmonic oscillators as a function of the two bare oscillators eigenmodes $\delta = \omega_2 - \omega_1$ and of the driving frequency. In the panels (a) to (d) we show the ARC phenomenon emerging as the strong coupling regime is reached, we label with ξ the adimensional quantity $\Omega^2/\gamma\omega_0$. In panel (e) we set $\xi = 5$ and a second coherent drive is added on oscillator two, only the symmetric mode is excited. In panel (f) the second drive is π-dephased and only the antisymmetric mode is excited close to zero detuning. In panel (g) $\xi = 5$ and the loss rate of the second oscillator is increased by a factor three.

$$2\Omega^2 > \omega_0(\gamma_1 + \gamma_2) \tag{1.10}$$

is equivalent to the Novotny's criterion and figure 1.2 (c) represents the transition between weak and strong coupling. We plot in figure 1.2 (e-h) the steady state power dissipated by the CHOs as a function of the driving frequency ω, for the same CHOs parameters of the correspective time dynamics shown in the panels (a-d). The power dissipated shows a progressive splitting of the single resonance which charaterizes the spectrum in the weak coupling regime. This effect is often called Rabi splitting and, as we mentioned in the introduction of this section, can be regarded as one of the three signatures of the strong coupling regime.

We mentioned also a third signature of strong coupling which is related to eigenfrequencies anticrossing. This simple CHOs model capture also this feature: we plot in figure 1.3 (a-d) the total power absorbed as a function of the driving frequency ω and of the detuning $\delta = \omega_2 - \omega_1$ for increasing values of the coupling Ω. As the strong coupling regime is reached (panels c,d)

we observe the characteristic avoided resonance crossing (ARC), when

$$\frac{|\delta|}{\gamma} \lesssim \frac{\Omega^2}{\omega_0 \gamma} \tag{1.11}$$

the spectrum clearly shows two resonances which repeals each other as zero detuning is crossed. While for higher values of the detuning the spectrum is essentially dominated by a single resonance which corresponds roughly with the driven oscillator eigenfrequency. This happens because if the detuning becomes large the efficiency of the energy exchange decrease over orders of the linewidth. Avoided resonance crossing is a sufficient but not necessary signature of strong coupling. The spectral response of the CHOs depends on the match between the driving force and the eigenmodes of the system. Indeed when only one resonator is driven both the symmetric and antisymmetric are excited but if a second harmonic drive is added on the second oscillator with a phase $\varphi = 0, \pi$ only the symmetric or antisymmetric mode are respectively excited close to zero detuning. For higher values of the detuning since the resonances repeals the driving frequency no longer maches any of the system eigenmodes and partial tough weak excitation of the dark mode happens because of inefficient energy exchange processes.

These features are captured in figure 1.3 (e-f) which shows the total power dissipated spectrum as a function of the driving frequency and oscillators detuning in the deep strong coupling regime with a coherent and π-dephased drive of the second oscillator.In figure 1.3 (g) we show the absorbed power spectrum with the same parameters of the CHOs in panel (d) but with an increased loss rate $\gamma_2 = 3\gamma_1 = 3 \cdot 10^{-3}\omega_0$ in the undriven oscillator. It is noteworthy that in the deep strong coupling regime even if just one of the two oscillators has an increased loss rate, both the eigenfrequencies linewiths are equally broadened. This happens because in the strong coupling regime the individuality of the two oscillators is lost and thanks to efficient energy exchange the most lossy oscillator sets the damping rate of both the oscillators. In the weak coupling regime instead one expects the increased loss on the second oscillator acts as a small perturbation on the first oscillator dynamics.

As discussed in the introduction of this chapter, our main interest in strong coupling relies in the possibility of creating mixed light-matter states. This mixing is visual in this classical picture of CHOs as energy exchange cycles sets in, indeed if we take a time cut of the dynamics and we measure E_tot for the two oscillators, when $\Omega^2 \ll \omega_0\gamma$ $E_{Tot,1} \approx e^{-\gamma t}$ and $E_{Tot,2} \approx 0$ but with $\Omega^2 \gg \omega_0\gamma$, in general, $E_{Tot,1} = E_1 \neq 0$ and $E_{Tot,2} = E_2 \neq 0$. Therefore the fundamental excitation of the whole system can be written as a superposition of the two bare oscillator energies

$$E_{Tot} = E_1 + E_2 = \left(\alpha(t)^2 + \beta(t)^2\right) \tag{1.12}$$

with $\alpha^2+\beta^2=e^{-\gamma t}$ to recount for the total losses. The coefficients $\alpha(t)$ and $\beta(t)$ can be seen as the time dependent amplitudes of the two oscillators. In a quantum picture this can be rephrased by assuming an eigenfunction of the system with the form

$$|\psi(t)\rangle=\alpha(t)|1,0\rangle+\beta(t)|0,1\rangle \tag{1.13}$$

where $|1,0\rangle$ and $|0,1\rangle$ are the fock states corresponding to the fundamental excitations of oscillator one and two respectively. If we sample at different times whether the system is in the state $|1,0\rangle$ or $|0,1\rangle$, we would find on average with a probability $\tilde{\alpha}$ the fock state $|1,0\rangle$ and $\tilde{\beta}$ the fock state $|0,1\rangle$. Where $\tilde{\alpha}$ and $\tilde{\beta}$ are defined as

$$\begin{aligned}\tilde{\alpha}^2&=\int_0^\infty\frac{\langle\psi(t)|P_{|1,0\rangle}|\psi(t)\rangle}{\langle\psi(t)|\psi(t)\rangle}dt=\int_0^\infty\frac{\alpha^2(t)}{e^{-\gamma t}}dt\\ \tilde{\beta}^2&=\int_0^\infty\frac{\langle\psi(t)|P_{|0,1\rangle}|\psi(t)\rangle}{\langle\psi(t)|\psi(t)\rangle}dt=\int_0^\infty\frac{\beta^2(t)}{e^{-\gamma t}}dt\end{aligned} \tag{1.14}$$

$P_{|\cdot\rangle}$ are the projectors of the two Fock states and we used $\alpha^2+\beta^2=e^{-\gamma t}$. The eigenstate of the system can be mapped as a point on a Bloch spere with angular coordinates $(\alpha(t),\beta(t))$ and a exponentially suppressed radius on timescales order of γ^{-1}. In figure 1.4 we plot these coefficients as a function of the parameter $\Omega^2/\omega_0\gamma$, if the coupling Ω equals zero, $\tilde{\alpha}^2=1$ and $\tilde{\beta}^2=1-\tilde{\alpha}^2=0$ and the system lays in the pure Fock state $|1,0\rangle$. As Ω increases the two cefficients $\tilde{\alpha}^2$ and $\tilde{\beta}^2$ tend to the value $1/2$ charateristic of a maximally mixed state. Notice that the coefficients $\tilde{\alpha}$ and $\tilde{\beta}$ also depend on the detuning $\delta=\omega_2-\omega_1$ which was set to zero in our analysis. We show in figure 1.4 the effect of the detuning following the palette colorcode for the curves: if the quantity $\Omega^2/\omega_0\gamma$ is fixed the mixing efficiency decrease with the absolute value of the oscillators detuning. The proposed analogy is an intuitive picture showing that trough strong coupling of two oscillators the fundamental excitations of the system are mixed states: the components of a strongly coupled system lose their individuality.

We finally address the problem of mapping the CHOs classical equation of motion in a Non-Hermitian two-mode Hamiltonian (NHH) and we discuss the origin of the strong coupling boundary in a quantum picture. The NHH has a complex spectrum which imaginary part is related to the losses due to energy exchange with the environment, thus constituting one of the simplest examples of non trivial open quantum system.

We can start by substituting the ansatz $x_j(t)=x_j^0e^{-i\omega t}$ in equation (1.2) and then divide the j-th row by $(\omega_j+\omega)$ obtaining

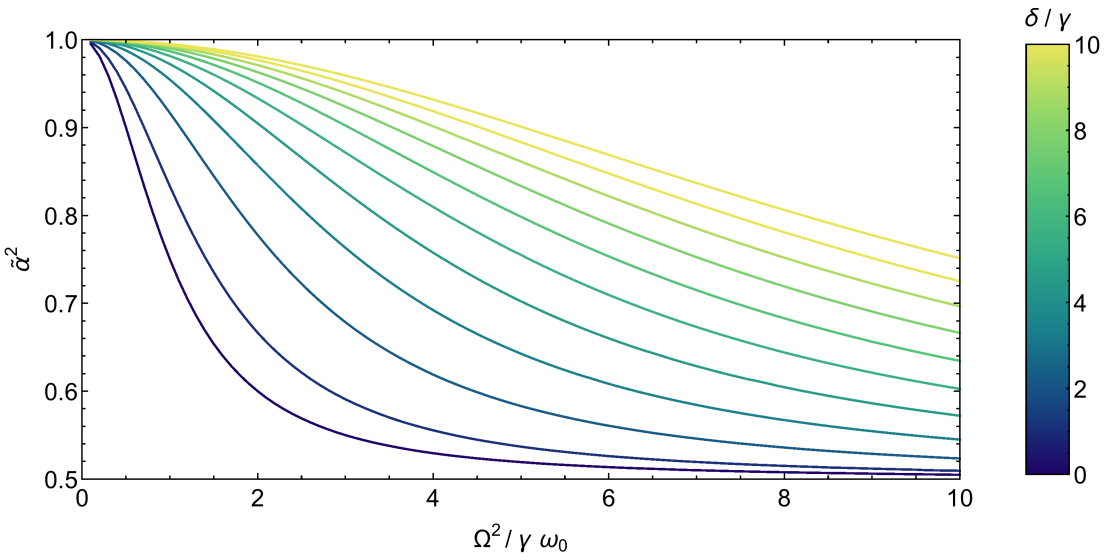

Figure 1.4: Average energy stored in oscillator one as a function of the coupling relative strenght $\Omega^2/\gamma\omega_0$ for different detuning values. We set $\omega_0 = (\omega_1 + \omega_2)/2 = 1\ rad\,s^{-1}$ and $\gamma = \gamma_1 = \gamma_2 = 10^{-3}\omega_0$. This average energy stored in the two oscillators can be seen in the analogy with a two level atom coupled to a single mode resonator, as the mixing degree of the eigenstates of the system.

$$\begin{pmatrix} \omega_1 - \omega - \frac{i\gamma_1\omega}{\omega_1+\omega} & -\frac{\Omega^2}{\omega_1+\omega} \\ -\frac{\Omega^2}{\omega_2+\omega} & \omega_2 - \omega - \frac{i\gamma_2\omega}{\omega_2+\omega} \end{pmatrix} \begin{pmatrix} x_1 \\ x_2 \end{pmatrix} = \begin{pmatrix} 0 \\ 0 \end{pmatrix} \tag{1.15}$$

Since the response of the system if $\gamma \ll \omega_0$ is tightly peaked around ω_0 we can assume that in our region of interest $|\omega - \omega_{1,2}| \ll \omega$, then

$$\begin{pmatrix} \omega_1 - \omega - \frac{i\gamma_1}{2} & -\frac{\Omega^2}{2\tilde{\omega}} \\ -\frac{\Omega^2}{2\tilde{\omega}} & \omega_2 - \omega - \frac{i\gamma_2}{2} \end{pmatrix} \begin{pmatrix} x_1 \\ x_2 \end{pmatrix} = \begin{pmatrix} 0 \\ 0 \end{pmatrix} \tag{1.16}$$

and we defined $\tilde{\omega} \approx (\omega + \omega_{1,2})/2$ as the mean oscillator frequency. The above linear system has non-trivial solutions if and only if $det(H - \mathbb{1}_2\omega) = 0$. If we define $g = -\Omega^2/(2\tilde{\omega})$ the matrix H has the form

$$H = \begin{pmatrix} \omega_1 - \frac{i\gamma_1}{2} & g \\ g & \omega_2 - \frac{i\gamma_2}{2} \end{pmatrix} \tag{1.17}$$

which is in units of $\hbar = 1$ the two-mode NHH corresponding to the CHOs. The eigenvalues of the above two mode Hamiltonian are

$$\omega_\pm = \tilde{\omega} \pm \frac{\Delta}{2}\sqrt{1 + \left(\frac{2g}{\Delta}\right)^2} \tag{1.18}$$

and we defined the quantities $\tilde{\omega}$ as the average complex frequency of the bare states and Δ their complex detuning

$$\begin{aligned} \tilde{\omega} &= \frac{1}{2}(\omega_1 + \omega_2) - \frac{i}{4}(\gamma_1 + \gamma_2) \\ \Delta &= (\omega_1 - \omega_2) - \frac{i}{2}(\gamma_1 - \gamma_2) \end{aligned} \tag{1.19}$$

If we now expand in Taylor series the eigenvalues of the NHH around $2g/\Delta = 0$ we find

$$\omega_\pm = \tilde{\omega} \pm \frac{\Delta}{2}\left(1 + \left(\frac{2g}{\Delta}\right)^2 - \left(\frac{2g}{\Delta}\right)^4 + ...\right) \tag{1.20}$$

however this Taylor expansion converges only inside a disk in the complex plane of radius $|2g/\Delta| = 1$, if g is such to lye outside this disk, the eigenvalues of the system can not be anymore expressed as a perturbative series of the bare oscillators ones: this non-perturbative regime is what we call the strong coupling regime. In contrast with the classical picture the transition from weak to strong coupling in the quantum picture is characterized by a sharp boundary dictated by the complex polar singularities of the eigenvalues of the NHH (eq. (1.18)) for $2g/\Delta = \pm i$. While for $|2g/\Delta| < 1$ the manifolds describing $\omega_\pm$ in the complex detuning plane Δ, are never crossing each other. This means the oscillators individuality is still present because any analytical transformation (i.e. time evolution) can map a system prepared in the eigenstate $+$ in the $-$ one. This is anymore the case when $|2g/\Delta| > 1$ because the two eigenvalues manifolds cross and the system constituents as we already found for the classical CHOs model, completely lose their individuality.

In the following sections we address the description of the matter and light degrees of freedom we want to couple: quantum well excitons and cavity photons.

1.2 III-V Semiconductors: Excitons

To better understand the exciton-polaritons physics it is worth to recall briefly some general properties of semiconductors, which fundamental excitations, electron-hole pairs constitute the matter degree of freedom we want to strongly couple with a confined light field. We will focus on zinc-blend type semiconductors which are much more optically active than diamond-like crystal thanks to their direct bandgap structure. The formal description of a crystal involves the solution of the Shrödinger equation for the Hamiltonian involving $N \sim 10^{23} cm^{-3}$ atoms; because of tight atom packing and long range Coulomb interaction, the problem results in something intractable. However one can start by using Born-Oppenheimer approximation which relies on the separation of nuclear and electronic dynamics thanks to the enormous difference between the nuclei and electronic cloud mass entailing completely different characteristic timescales. The crystal hamiltonian can be separated in three contributions

$$\mathscr{H} = H_{ion} + H_{e-ion} + H_e \tag{1.21}$$

the first recounts for the interaction between nuclei and core electrons which determines the form of the effective ion-ion interaction potential. The ground state eigenvector of H_{ion} can be addressed by mean of a variational principle and encodes the crystalline arrangement of the atoms. The second term describes the interaction between valence electrons, which occupy the outer incomplete shells of the electron cloud and the ions when they are displaced from their equilibrium positions (electron-phonon interactions in a second quantization picture). This term is responsible for instance of energy relaxation machanisms of excited electrons, and in the further considerations will be neglected since constitutes a small perturbation to the total hamiltonian. We anyhow stress that in different crystal structures, at low temperatures, this term may become of crucial importance, indeed in metal componds it is responsible for the quantum phase transition from conductor to superconductor (BCS mechanism). The last term H_e describes both the intercation between electrons and ions frozen on their equilibrium positions and electron electron Coulomb interactions and has the form

$$H_e = \sum_i \frac{p_i^2}{2m_0} + \frac{1}{2}\sum_{i\neq j} \frac{e^2}{4\pi\varepsilon_0|\mathbf{r}_i - \mathbf{r}_j|} - \sum_{i,j} \frac{Q_j e^2}{4\pi\varepsilon_0|\mathbf{R}_i - \mathbf{r}_j|} \tag{1.22}$$

where $\mathbf{p}_i$ is the electron momentum operator, e the electron charge, ε_0 the vacuum permittivity, m_0 the free electron mass, Q_j the absolute ion valence, and $(\mathbf{r}, \mathbf{R})_j$ are the position operators of the j-th electron or ion.

In many III-V semiconductor compounds the ground state solution of H_{ion} evidences a zinc-blende structure, which is by translating along the main diagonal two face centered cubic bravais lattices of the two semiconductor species by one quarter of the cell parameter. The valence

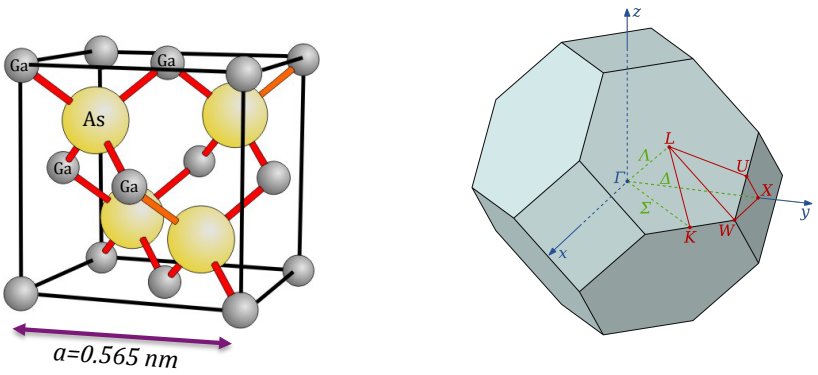

Figure 1.5: Gallium Arsenide zinc-blende lattice structure (left) and first Brillouin zone in reciprocal space showing the Γ point and the maximal symmetry directions (right).

electrons arange to form four bonds arranged in a tethraedral covalent bonding structure. We will focus on Gallium Arsenide (GaAs); since the incomplete outer shell of Ga is $4s^2 4p^1$ and the As one is $4s^2 4p^3$ the valence electrons have p-type charater in their ground state forming sp^3 hybridized covalent bonds. We show in figure 1.6 the zinc-blende bravais cell of GaAs and its corresponding representation in reciprocal space which geometric center is called Γ point.

Some intersting properties of the eigenstates of the H_e can be deduced by using a mean field description of H_e where each valence electron feels an averaged potential $V(\mathbf{r})$ coming from the ions and the rest of the electrons. We will not enter in the difficult task of calculating the form of $V(\mathbf{r})$ which can be addressed by means of variational principles or density functional theory, we refear to [34]-[35] for the details. The many-body hamiltonian H_e can be then reduced to the effective one body Luttinger-Khon hamiltonian

$$H^{\mu}_{\nu} = \left(\frac{p^2}{2m_0} + V(\mathbf{r})\right)\mathbb{1}^{\mu}_{\nu} + \frac{\hbar}{4m_0^2c^2}(\varepsilon_{ijk}\partial^i V(\mathbf{r})p^j)(\sigma^k)^{\mu}_{\nu} \tag{1.23}$$

$$H^{\mu}_{\nu}\psi^{\nu}_{n,\mathbf{k}}(\mathbf{r}) = E_n(\mathbf{k})\psi^{\mu}_{n,\mathbf{k}}(\mathbf{r})$$

where c is the light speed, $\psi^{\mu}_{n,\mathbf{k}}(\mathbf{r})$ is the position representation of the spinorial eigenfunction with a given momentum $\mathbf{k}$, band index n and spin S_z component labeled by the index μ and $(\sigma^k)^{\mu}_{\nu}$ are the (μ,ν) entries of the k-th Pauli matrices. While the left part of the hamiltonian is the standard Shrödinger equation for a massive particle the second term has a relativistic origin and models the spin-orbit coupling of spin and angular momentum with the electrostatic field generated by the background. This term is usually a perturbation δE_{so} to the standard hamilto-

nian which may become important in proximity of points of maximal symmetry as the Γ point since it's responsible of a band splitting which depends on electron momentum **k**, total angular momentum J and its z-projection J_z. We first neglect this term to simplify our analysis of equation (1.23) but we discuss its influence in a second moment.

If we neglect H_{so} the spinorial indexes becomes trivial, and the Shrödinger equation becomes scalar. Thanks to the bravais cell translational symmetry, the Bloch's theorem can be applied, ensuring that the eigenfunctions of the electron can be expanded in a Fourier series of free electron plane waves enveloped by a periodic function

$$\psi_{n\mathbf{k}}(\mathbf{r}) = u_{n\mathbf{k}}(\mathbf{r})\, e^{i\mathbf{k}\cdot\mathbf{r}} \tag{1.24}$$

where $u_{n\mathbf{k}}(\mathbf{r})$ is a function with the same periodicity as the crystal potential and **k** are the momenta of the free electron plane waves. The k-states results discretized in cubic crystal of side L, however for typical macroscopic crystal the discretized levels are spaced by $\Delta k = 2\pi/L$ and thus forms a quasi-continuum of states. The effect of the potential $V(\mathbf{r})$ is to open energy gaps between the bands n and $n+1$ close to the first brillouin zone edge [35]. The band structure of GaAs can be calculated for instance with perturbation theory ($\mathbf{k}\cdot\mathbf{p}$ method). If the Bloch wavepacket in equation (1.24) is substituted in the Luttinger-Khon hamiltonian with zero spin-orbit coupling we get

$$\left(\frac{p^2}{2m_0} + \frac{\hbar^2 k^2}{2m_0} + \frac{\hbar\mathbf{k}\cdot\mathbf{p}}{m_0} + V(\mathbf{r})\right) u_{n\mathbf{k}}(\mathbf{r}) = E_n(\mathbf{k}) u_{n\mathbf{k}}(\mathbf{r}) \tag{1.25}$$

this equation at the Γ point where $|\mathbf{k}| = 0$ takes the simple form

$$\left(\frac{p^2}{2m_0} + V(\mathbf{r})\right) u_{n0}(\mathbf{r}) = E_n(0) u_{n0}(\mathbf{r}) \tag{1.26}$$

once the solutions of this simple equation are known, the solution for small k vectors can be inferred by standard perturbation theory techniques. A second order expansion gives the following form for the eigenenergies of the system close to the Γ point

$$E_n(\mathbf{k}) = E_n(\mathbf{0}) + \frac{\hbar^2 k^2}{2m_0} + \frac{\hbar^2}{m_0^2} \sum_{n' \neq n} \frac{|\langle u_{n\,\mathbf{0}} | \mathbf{k}\cdot\mathbf{p} | u_{n'\mathbf{0}} \rangle|^2}{E_{n\,\mathbf{0}} - E_{n'\mathbf{0}}} \tag{1.27}$$

This equation defines the crystal dispersion relation in the so called parabolic which takes the simplified form

$$E_n(\mathbf{k}) = E_n(\mathbf{0}) + \frac{\hbar^2 k^2}{2m^*} \tag{1.28}$$

where the scalar quantity

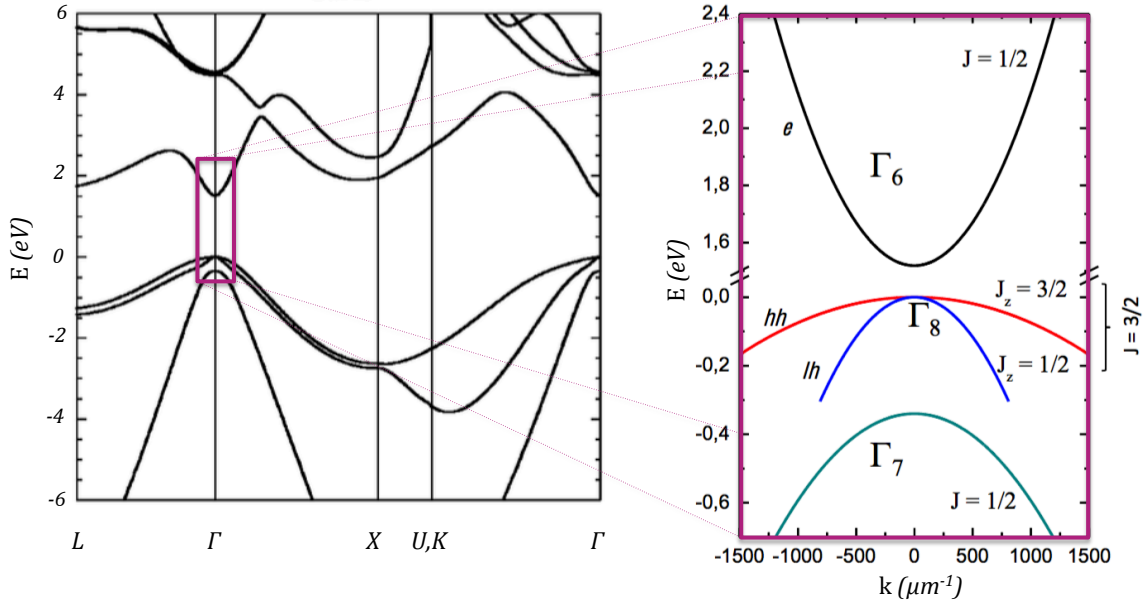

Figure 1.6: Gallium Arsenide bandstructure calculated with a thirty orbital $\mathbf{k}\cdot\mathbf{p}$ method from ref [36] (left panel). Parabolic band approximation close to the Γ point for the conduction band Γ_6, the so called light hole and heavy hole valence bands Γ_8 and the split-off band Γ_7.

$$\frac{1}{m^*} = \frac{1}{m_0} + \frac{2}{m_0^2 k^2} \sum_{n' \neq n} \frac{|\langle u_{n\,\mathbf{0}} | \mathbf{k}\cdot\mathbf{p} | u_{n'\mathbf{0}} \rangle|^2}{E_{n\,\mathbf{0}} - E_{n'\mathbf{0}}} \tag{1.29}$$

defines the effective mass of a charge carrier in the n band and can be generalized as [35]

$$\left(\frac{1}{m^*}\right)_{i,j} = \frac{1}{\hbar^2}\left(\frac{\partial^2 E_n(\mathbf{k})}{\partial k_i \partial k_j}\right) \tag{1.30}$$

We show in figure 1.6 the bandstructure of GaAs calculated with perturbative $\mathbf{k}\cdot\mathbf{p}$ methods involving thirty orbitals [36] and the corresponding parabolic band approximation. The following parameters can be extracted for monocystalline GaAs [37]

$T = 300^o K$	$T = 4^o K$
$E_{gap}(\mathbf{0}) = 1.424\ eV$	$E_{gap}(\mathbf{0}) = 1.519\ eV$
$E_{so}(\mathbf{0}) = -0.34\ eV$	$E_{so}(\mathbf{0}) = -0.34\ eV$
$m^*_{co} = 0.067\ m_0$	$m^*_{co} = 0.063\ m_0$
$m^*_{hh} = 0.45\ m_0$	$m^*_{co} = 0.51\ m_0$
$m^*_{lh} = 0.082\ m_0$	$m^*_{co} = 0.082\ m_0$
$m^*_{so} = 0.154\ m_0$	$m^*_{co} = 0.150\ m_0$

$E_{co} - E_h$ constitutes the fundamental bandgap at the Γ point, the so called heavy hole and light hole bands are degenerate for zero momentum charge carriers but split because of k-dependent

spin orbit coupling to the band total angular momentum projections. H_{so} is also responsible for the split off band gap E_{so} and is an energy offset term due to the total angular momentum absolute value. Indeed the spin orbit coupling hamiltonian takes the four-band effective form [35]

$$H^{KL} = -\frac{\hbar^2}{2m_0}\left((\gamma_1 + \frac{5}{2}\gamma_2)k^2 - 2\gamma_2(J_x^2k_x^2 + J_y^2k_y^2 + J_z^2k_z^2) - 2\gamma_3\sum_{m\neq n} J_mJ_nk_nk_n\right) \tag{1.31}$$

where $J_{x,y,z}$ are the spin $3/2$ Pauli matrices and γ_i are the so called Luttinger parameters which can be measured by best fitting experimental datas with the model (from [36]):

$\gamma_1 = 6.85$	$\gamma_2 = 2.9$	$\gamma_3 = 2.1$

In combination with magnetization, this type of spin–orbit interaction will distort the electronic bands depending on the magnetization direction, thereby causing Magnetocrystalline anisotropy. We refear for this fine splitting phenomena to [35]. Finally we highlight that we reported positive effective masses for the valence band whereas the parabolic bands depicted have negative second derivative for zero wavevector (i.e negative effective mass). We adopted the so called hole picture: since at zero temperature the semiconductor ground state has insulating charater and the fundamental excitation consists in the promotion of one valence electron to the conduction band thus creating a vacancy in the valence band which can be effectively seen as a positively charged particle. The interaction term then changes sign for the holes but this can be absorbed if the effective mass sign is changed, so that the same effective hamiltonian describes both electron and vacancies. Therefore in parabolic band approximation negatively charged particles have positive effective mass in bands with positive curvature and vice-versa.

Let see how we can extract some information on the angular momentum of the different bands which will be fundamental information to distingush the optically allowed transition. As pointed before the valence bands posses a p-type bonding character thus inheriting orbital angular momentum $L = 1$, while the conduction band originates from s-type valence orbitals thus having $L = 0$. The charge carriers (electron and vacancies) in these bands have half-integer spin. From the composition rule of spin and orbital angolar momentum it is straightforward to show that the conduction band Γ^6 has $J = 1/2$, the spin orbit coupling for this band is in first approximation is zero, this reflects on the four-band Luttinger hamiltonian (1.31) which depends only on three parameters, and the effect of the third component of angular momentum has the only role of setting the degeneracy of the band. The valence band electrons have $L = 1$ and $S = 1/2$, thus the total angular momentum rule tells us that the band degeneracy is 6 since if we label with $|J, J_z\rangle$ the band states we have $|3/2, \pm 3/2\rangle$, $|3/2, \pm 1/2\rangle$ which are respectively the heavy and light hole bands Γ_8 and the split-off band $|1/2, \pm 1/2\rangle$ labeled in figure 1.6 as Γ_7.

1.2.1 Excitons

The fundamental excitation of a zero temperature crystal consits in the promotion of an electron to the conduction band with the creation of a valence band vacancy which can be effectively pictured as a positively charged particle we call hole. Since these two charge carriers have opposite sign they feel a mutual attraction due to Coulomb interactions and may eventually form a bound state called exciton. In the semiconductor morphologies we are considering, electron-hole interaction is heavily screened by the fermi electron sea, so the net wavefunctions of the bound state are extended over several unit cells and this states are called Wannier-Mott excitons. A completely different situation for instance emerges in ionic crystals where excitons are strongly localized.

We can model the exciton as an hydrogen-like atom using the effective mass approximation, the time independent Schrödinger equation reads

$$\left(\frac{p_e^2}{2m_e^*}+\frac{p_h^2}{2m_h^*}+\frac{e^2}{4\pi\varepsilon|\mathbf{r}_e-\mathbf{r}_h|}\right)\psi(\mathbf{r}_e,\mathbf{r}_h)=(E-E_{gap})\psi(\mathbf{r}_e,\mathbf{r}_h) \tag{1.32}$$

where ε is the dielectric permittivity of the material which models the screening effect of the valence electron sea. We can now pass to the center of mass reference frame: we call the center of mass position operator $\mathbf{R}$ and the relative distance from the center of mass $\mathbf{r}$ defined as

$$\begin{aligned}(m_e^*+m_h^*)\mathbf{R}&=(m_e^*\mathbf{r}_e+m_h^*\mathbf{r}_h)\\ \mathbf{r}&=\mathbf{r}_e-\mathbf{r}_h\end{aligned} \tag{1.33}$$

plugging this map in equation (1.32) one gets

$$\left(\frac{P^2}{2(m_e^*+m_h^*)}+\frac{p^2}{2\mu_{eh}}+\frac{e^2}{4\pi\varepsilon|\mathbf{r}|}\right)\psi(\mathbf{R},\mathbf{r})=(E-E_{gap})\psi(\mathbf{R},\mathbf{r}) \tag{1.34}$$

where $\mathbf{P}=-i\hbar\nabla_{\mathbf{R}},\mathbf{p}=-i\hbar\nabla_{\mathbf{r}}$ and $(\mu_{eh})^{-1}=(m_e^*)^{-1}+(m_h^*)^{-1}$. The eigenfunctions of this equation can be factorized as $\psi(\mathbf{R},\mathbf{r})=\phi(\mathbf{R})\chi(\mathbf{r})$, where $\phi(\mathbf{R})$ corresponds to free particle motion of mass $(m_e^*+m_h^*)$ and $\chi(\mathbf{r})$ has the form of the well known hydrogen atom orbitals, which can be expressed as product of generalized Laguerre polynomials $L_n^\alpha(r)$ and spherical armonic functions $Y_{l,m}(\theta,\phi)$. If $\mathbf{R}$ is written in cartesian coordinates and $\mathbf{r}$ in spherical coordinates the eigenfunctions have the form

$$\psi_{n,l,m}=(\mathbf{R},\mathbf{r})=e^{i\mathbf{K}\cdot\mathbf{R}}\sqrt{\left(\frac{2}{na_B}\right)^3\frac{(n-l-1)!}{2n(n+l)!}}e^{-\frac{\rho}{2}}\rho^l L_{n-l-1}^{2l+1}(\rho)Y_{l,m}(\theta,\phi) \tag{1.35}$$

where n is the principal quantum number l eigenvalue of the angular momentum operator L^2

and m the eigenvalue of its third component L_z, $\rho = 2r/na_0$ and a_B is the bulk exciton Bohr radius

$$a_B = \frac{4\pi\hbar^2\varepsilon}{\mu_{eh}e^2} \tag{1.36}$$

which for Gallium Arsenide at 4^oK is $a_B \approx 14.2\ nm$, on this typical exciton sizes the relativistic corrections, the lamb shift and fine structure of the eigenenergies can be safely neglected, thus

$$E_{n,l,m}(\mathbf{K}) \approx E_n(\mathbf{K}) = E_{gap} + \frac{\hbar^2 K^2}{2(m_e^* + m_h^*)} - \frac{E_b}{n^2} \tag{1.37}$$

where $\hbar\mathbf{K}$ is the exciton center of mass linear momentum and E_b the Rydberg constant for the exciton. The first two terms recount for the gap and center of mass energy while the second is the binding energy of the system. The binding constant for GaAs reads

$$E_b = \frac{\mu_{eh}e^2}{32\pi^2\varepsilon^2\hbar^2} \approx 4.2\ meV \tag{1.38}$$

The exciton ground state eigenfunction at rest is given by $\mathbf{K} = \mathbf{0}$, $(n,l,m) = (1,0,0)$ and has the simple form:

$$\psi_{0,0,0}(r) = \sqrt{\frac{2}{a_B^3}} e^{-\frac{r}{a_B}} \tag{1.39}$$

These equations tells us that excitons are free to move in the crystal, nevetheless we expect in a non ideal system that excitons interacts with crystal vibrations (phonons), defects or other excitations resulting in a global dissipative term. We also see that the exciton ground state energy has it's own parabolic band located $\Delta E = E_b$ under the conduction band. At $k = 0$ in absence of the valence band mixing term $\propto \mathbf{k}\cdot\mathbf{p}$ both the hole and the electron have well defined total J and third component J_z angular momentum quantum numbers since $[H,J]|_{k=0} = [H,J_z]|_{k=0} = 0$. The resulting exciton will have well defined (J^X, J_z^X) quantum numbers given by the angular momentum composition rule with possible values $J_z^X = 0,1,2$:

$J_z^h \otimes J_z^e$	$J_z^{hh} = 3/2$	$J_z^{hh} = -3/2$	$J_z^{lh} = 1/2$	$J_z^{hh} = -1/2$
$J_e^z = 1/2$	$J_z^X = +2$	$J_z^X = -1$	$J_z^X = +1$	$J_z^X = 0$
$J_e^z = -1/2$	$J_z^X = +1$	$J_z^X = -2$	$J_z^X = 0$	$J_z^X = -1$

moreover the eigenvalues of total angular momentum are and $J_{hh}^X = 1,2$, this reflects the fact that the exciton is conformed by two fermions, therefore it's angular momentum and spin are integers, for this reason, as soon as the charge carrier gas is diluite (i.e. weak interactions), excitons can be regarded as composite bosons. We will discuss when addressing polariton-polariton interactions the limits of validity of this assumption.

We also point out that the theory we are showing mutually looks to exciton creation in an ideal environment where only one electron is promoted to the conduction band. However when the charge carrier density is high a vast ensamble of many body effects arise: the energy distribution changes from the spinless Maxwell-Boltzmann distribution to the Fermi-Dirac one, electron-hole gas wavefunction must be antisymmetrized due to Pauli principle, screening effects and spin dependent phenomena may become important. This results in modification of the bangaps, of the effective masses, of the effective dielectric permittivity of the system resulting in a decresing binding energy of the exciton eventually leading to dissociation in the high charge carrier density regime (electron -hole plasma). We refear for the details to the book of Yu and Cardona [35].

1.2.2 Bulk Optical transitions

The promotion of one electron from the valence band to the conduction band can be achieved with different strategies, among them by means of optical pump. The description of this process is a well-known absorption process: the light matter interaction hamiltonian can be deduced by inserting the minimal coupling ansatz

$$\mathbf{p} \rightarrow \left(\mathbf{p} + \frac{e}{c}\mathbf{A}\right) \tag{1.40}$$

in equation (1.26), where $\mathbf{A}$ is the vector potential of the incident radiation. If we assume a weak incident radiation intensity the quadratic terms in the vector potential can be safely neglected, this is the so called dipolar approximation $H_{dip} \propto \mathbf{p} \cdot \mathbf{A}$. The optical transitions in a semiconductor in dipolar approximation are characterized by two momentum selection rules [35]

1 -Linear momentum in the emission or absorption process must be conserved $\mathbf{k}_\gamma = \mathbf{k}_i + \mathbf{k_f}$ where $\mathbf{k}_{i,f}$ are respectively the initial and final state momenta and $\mathbf{k}_\gamma$ is the incident photon momentum. Typically the photon momentum is very small compared to the typical carrier momenta, this implies that only vertical optical transition are allowed in the band diagram $\mathbf{k}_i \approx -\mathbf{k}_f$.

2 -Angular momentum in the emission or absorption process must be conserved. This both impose selection rules depending on polarization of incident radiation and on the (J, J_z) components of the valence and conduction band.

The selection rules are exact only if $\mathbf{k} = \mathbf{0}$ where the operators J^2 and J_z commute with the Khon-Luttinger hamiltonian, when $\mathbf{k} \neq \mathbf{0}$ the valence band mixing effects allow forbidden transition, however these contributions close to the Γ point can be regarded as a second order effect. In

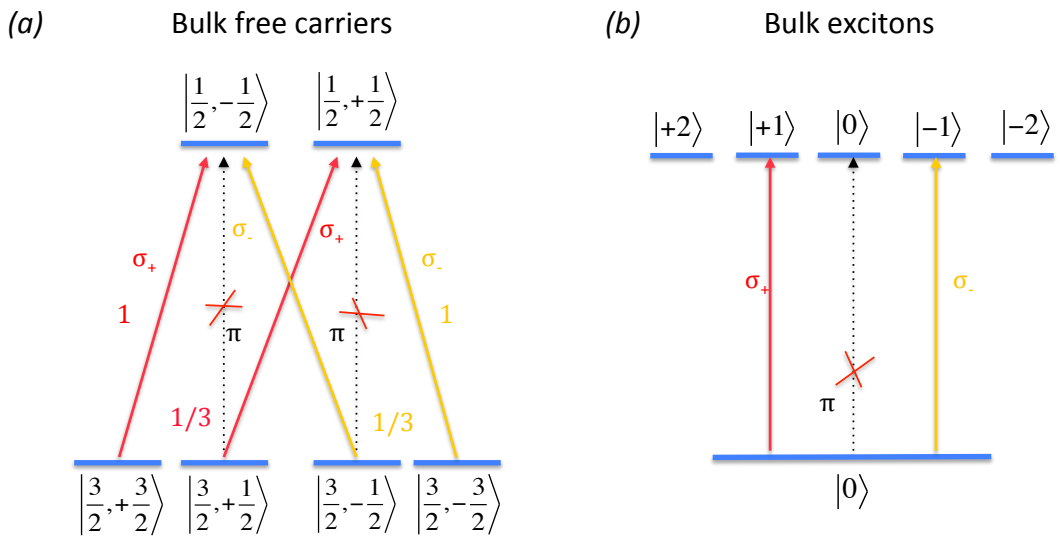

Figure 1.7: *Gamma* point polarization and relative intensity of the non-zero dipole matrix elements for the optical promotion of an electron from the valence band to the counduction band (a). Selection rules for the exciton creation via optical pumping (b), notice that only transitions to $J^X = 1$ excitons are allowed since $J^X = 2$ are dark states because of total angular momentum conservation and the assumption of a plane wave excitation.

general the transitions amplitude can be calculated in dipolar approximation by mean of the Fermi Golden Rule

$$P_{if} = \frac{2\pi}{\hbar} \sum_{\mathbf{k}} |u_{c,\mathbf{k}} \langle |H_{dip}| u_{h,\mathbf{k}} \rangle|^2 \delta(E_c(\mathbf{k}) - E_v(\mathbf{k}) - \hbar\omega) \tag{1.41}$$

where $u_{c,\mathbf{k}}$ and $u_{h,\mathbf{k}}$ are respectively the Bloch wavefunctions of a conduction band electron and a valence band hole. The calculation of the electric dipole matrix elements is much easier at the Γ point. The calculation is straightforward (we refear to [35]) and is summarized in figure 1.7-(a) where the allowed transition probabilities are reported for the free carriers. We denote with $\sigma_\pm$ left and right circularly polarized light, and with π_z we denote a linearly polarized radiation along the propagation direction. This last polarization geometry cannot be realized in the case of a plane wave which is in very good approximation the excitation scheme of our experiments, we will then neglect this transition. Its remarkable that an electron with $J_z^c = 1/2$ has three more times times the possibility of recombining with a $J_z^{hh} = 3/2$ heavy hole than with a $J_z^{lh} = -1/2$ light hole and this transition are the only one allowed if π photon transitions are neglected.

Excitons can also couple resonantly with light, and this process actually dominates the photoluminascence spectrum of a high quality direct gap semiconductor. The same linear and angular momentum conservation rules valid in case of unbound electron and hole are applicable. This

ensures that only excitons with center of mass momentum close to zero can couple to light since $\mathbf{K}_X \approx \mathbf{k}_\gamma = 0$. This narrow the optically active excitons to a very narrow momentum space region at the bottom of the exciton dispersion band. When non radiative processes (i.e. phonon exciton interactions) are small this narrow radiative region acts as a bottleneck for the exciton recombination.

Since the crystal ground state has $J_z = 0$ the conservation of total angular momentum prescribes $J_z^X + J_\gamma^z = 0$. For the circular polarized photons $J_\gamma^z = \pm 1$. The other selection rules in dipolar approximation can be derived in analogy with the hydrogen's atom ones: from the parity properties of the vector potential and of the hydrogenic eigenfuctions the dipole matrix overlap is nonzero only for $l = 0, m = 0$ states. Therefore only the $1s, 2s, 3s, \ldots$ transitions are optically active , heavy hole excitons with $J_z^{hh} = \pm 2$ and light hole excitons with $J_z^{lh} = 0$ are dark states, and in our experiments we neglect π_z transitions. Finally the optical transitions of interest are

Heavy hole excitons	*Light hole excitons*
$\|J, J_z\rangle = \|1, \pm 1\rangle$	$\|J, J_z\rangle = \|1, \pm 1\rangle$

We summarize these results in figure 1.7-(b), it is intersting that both σ_+ and σ_- radiation excites an admixture of light hole and heavy hole excitons, however the dipole matrix elements are proportional to $|\psi_{n,0,0}(\mathbf{R}, \mathbf{0})|^2$ ([35]) and the optical transition probability increase with the electron-hole wavefunction overlap, being inversely proportional to the third power of Bohr exciton radius [35], which is diffent for light and heavy holes.

$$\left(\frac{P^{hh}}{P^{lh}}\right)|_{\mathbf{k}=\mathbf{0}} \propto \left(\frac{a_B^{lh}}{a_B^{hh}}\right)^3 = \left(\frac{m_{hh}^*(m_{co}^* + m_{lh}^*)}{m_{lh}^*(m_{co}^* + m_{hh}^*)}\right)^3 \approx 3.9 \tag{1.42}$$

The creation of a light hole exciton by means of optical $\sigma_\pm$ pumping is therefore suppressed in bulk GaAs at $4^o K$ by factor about four.

1.2.3 Quantum Well Excitons

As we pointed in section 1.1 a common strategy to achieve strong coupling between light and matter is to turn the absorption and emission processes of a photon reversible by embedding a two level matter degree of freedom in a cavity. In order to obtain this geometry with semiconductor excitations is to build a $2D$ quantum well (QW) which can be inserted in the cavity. Such kind of stuctures can be obtained confining the excitons in $2D$ structures resulting from a thin layer of semiconductor material in between a semiconductor with a wider bandgap. Matter excitations get trapped along the growt direction when the extension of the bulk wavefunction of the exciton becomes comparable to the layer thickness. Lower dimensionality heterostructures like quantum wires and quantum dots can be also embedded, but will not be treated in this manuscript. We label the layer semiconductor with the letter A sandwitched in between the

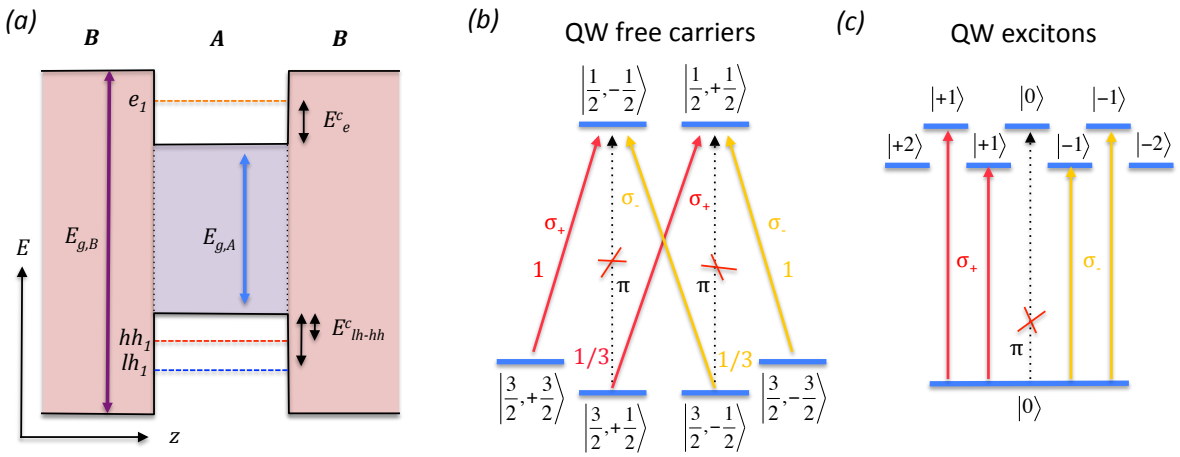

Figure 1.8: Γ point band structure for the quantum well A in between B semiconductor substrate. The first discretized levels for the confined electron and holes are depicted (a). Selection rules calculated at the Γ for the confined charge carriers and for the QW exciton creation via optical pumping, respectively in (b) and (c).

semiconductor B as sketched in figure 1.8-(a). We can again use the Bloch decomposition to write the wavefunction envelopes as

$$\psi_{\mathbf{k}}(\mathbf{r}) = \sum_n e^{i\mathbf{k}\cdot\mathbf{r}} u^A_{n,\mathbf{k}}(\mathbf{r}) \tag{1.43}$$

if $\mathbf{r}$ belongs to the layer A, and as

$$\psi_{\mathbf{k}}(\mathbf{r}) = \sum_n e^{i\mathbf{k}\cdot\mathbf{r}} u^B_{n,\mathbf{k}}(\mathbf{r}) \tag{1.44}$$

if $\mathbf{r}$ belongs to semiconductor B. One should then impose the continuity of u^A and u^B and of their weighted mass derivatives at the AB inteface. The problem is analogous to a particle confined in a two dimensional square well: the problem can be solved separately for the conduction and valence bands considering the appropriate effective mass. A straightforward consequence of confinement in the growt direction $\hat{z}$ is the quantization of the energy in the $\hat{z}$ direction leading to a splitting of every band in different confined states. Indeed the system hamiltonian for a given valence band has the form

$$H = E_{gap} + H_e + H_h + H_{eh} \tag{1.45}$$

where the different contributions are

$$\begin{aligned} H_e &= \frac{p_e^2}{2m_e^*} + V_e(z) \\ H_h &= \frac{p_h^2}{2m_h^*} + V_h(z) \\ H_{eh} &= \frac{-e^2}{4\pi\varepsilon(z)|\mathbf{r}_e - \mathbf{r}_h|} \end{aligned} \tag{1.46}$$

We can consider a simplified system if we assume an infinitely high squared well, so that $\psi_{\mathbf{k}}(\mathbf{r}) = 0$ in the B region. The general case for a finite well and can be solved analytically at least of quadratures by mean of a variational principle, we refear to [38] for the details. If we set $H_{eh} = 0$ the hamiltonian eigenfuctions are exactly

$$E_{n,m}(\mathbf{K}) = E_{gap} + E_{n,e} + E_{m,h} + \frac{\hbar^2 K^2}{2(m_{e,\|}^* + m_{h,\|}^*)} \tag{1.47}$$

where $E_{n,e}$ and $E_{m,h}$ are respectively the confined electron and hole eigenenergies depending on the principal quantum numbers n, m

$$E_n = \frac{\pi^2 \hbar^2 n^2}{2m_{\perp,e,h}^* L^2} \quad , \quad n \in \mathbb{N}_0 \tag{1.48}$$

where L is the layer depth. The electron-hole interaction term can be calculated if we assume $z \ll \rho$ where ρ is the in plane coordinate, which is valid if the A layer depht is such that $d \ll a_B^{3D}$. The problem in this perfect $2D$ well assumption can be factorized in the inplane and off plane direction

$$\psi(\mathbf{r}_e, \mathbf{r}_h) \propto e^{i(\mathbf{k}_\| \cdot \mathbf{R}_e + \mathbf{k}_\| \cdot \mathbf{R}_h)} \chi(z_e)\chi(z_h)\phi(\mathbf{r}_\|) \tag{1.49}$$

and the solutions the relative reference frame $(\mathbf{R}_\|, \mathbf{r}_\|)$ again becomes anologous to the solution of a $2D$ hydrogen atom, thus we need to add the $2D$ binding energy contribution $E_b(q)$ and the eigenenergies of the system have the form

$$E_{n,m}(\mathbf{K}_\|) = E_{gap} + E_{n,e} + E_{m,h} + \frac{\hbar^2 K_\|^2}{2(m_{e,\|}^* + m_{h,\|}^*)} - \frac{E_b^{2D}}{q^2} \tag{1.50}$$

where $\hbar\mathbf{K}_\|$ is the in plane momentum of the exciton and E_b^{2D} is the Rydberg constant for the $2D$ hydrogen-like atom. Out of these approximations the problem is still tractable but the calculations are cumbersome and add nothing to the relevant physics for our purposes. A straighforward implication of equation (1.50) is that even at $\mathbf{K} = \mathbf{0}$ the light and heavy holes bands are anymore degenerate since the confinement depends on the charge carrier effective mass, moreover the dispersion is still parabolic close to the Γ point. Another consequence of the confinement is that the electron and hole wavefunction ovelap is greatly enhanced thus providing

an increased optical oscillator strenght respect to bulk excitons. In particular in the perfect $2D$ infinite well approximation the exciton Bohr radius is half the bulk one, since the absorption and emission cross section in bulk is proportional to $(a_B^{3D})^{-3}$ and in the QW is proportional to $(a_B^{2D})^{-2}$ the enhancement factor is $\varepsilon = 4$. If we assume a finite quantum well height, the penetration depth in the B material decrease this value by increasing the a_B^{2D} value, the same happens if the well depth becomes comparable or bigger than the bulk exciton Bohr radius. Another practical advantage of working with confined excitons is the possibility of fine tuning control over the QW gap energy by engineering the well depth following equation (1.48) and this will be an important feature in order to control the exciton-cavity photon detuning, which as we showed in section 1.1 is a critical parameter in the strong coupling regime.

The optical selection rules for transitions between heavy or light hole and conduction subbands are the same as those reported in bulk, with some additional requirements:

1- The planar symmetry of the structure implies in plane linear momentum conservation[1] in emission absorption processes

2- Due to the parity of the confined wavefunctions in each subband, the only single photon emission or absorption admitted processes are those satisfying $(n+m)/2 \in \mathbb{N}_0$ where n and m are the principal quantum numbers respectively to the electron and the hole subband. Its noteworthy that transitions within subbands with $n = m$ are strongly enhanced due to an increased electron and hole wavefunction overlap.

We schematize the allowed optical transition in figure 1.8-(b,c). An unpolarized plane wave can excite also in the quantum well both light and heavy hole excitons, however here even at $\mathbf{K}_{\parallel} = \mathbf{0}$ the two subbands are splitted in energy, thus allowing to couple selectively only to one of the two. Heavy excitons show enhanced coupling to radiation respect to light holes :

$$\left(\frac{P^{hh}}{P^{lh}}\right)|_{\mathbf{k}=\mathbf{0}} \propto \left(\frac{a_{B,lh}^{2D}}{a_{B,hh}^{2D}}\right)^2 \approx 2.4 \tag{1.51}$$

their choice is therefore natural in the perspective of achieving the strong coupling between quantum well excitons and cavity photons. An unpolarized plane wave resonant with the heavy-hole subband transition creates an admixture of $|J, J_z\rangle = |1, \pm 1\rangle$ excitations, being the $J = 2$ states dark as discussed before. Hereafter when refering to excitons we will implicitly assume we are talking of heavy-hole excitons with $J = 1$ total angular momentum.

[1] Formally this can be proven via the Noether theorem, since momentum conservation is associated to traslational invariance.

1.3 Cavity Photons

In order to achieve strong coupling between a quantum well exciton and photons the emission absorption process has to be made reversible and the natural pathway to this goal is to embed the QW in a cavity. To this aim the first ingredient are mirrors: Distributed Bragg Reflectors (DBR) are dielectric haterostructures composed of two alternating layers of material with a different index of refraction. The working principle of such structures can be understood in analogy with the case of one electron in a periodic potential, but in this case the role of the electron is played by a photon and the periodic potential enters the Helmoltz equation via the refractive index modulation: this is why these structures are often referred as photonic crystals. Thanks to the discrete symmetry of the structure along the growt direction, the Bloch theorem can be used to expand the tranverse electro-magnetic field. In full analogy with a one dimensional crystal with a two atom unit cell the dispersion band struture has energy gaps i.e. exists a energy range in which the electromagnetic wave propagation is forbidden, thus the photonic crystal acts as a mirror. When building a mirror one is interested both on its reflectivity, both on the spectral range in which the mirror works. The photonic crystal acts as a mirror within the bandgap range, which is maximal at normal incidence if the optical thiknesses of the layers are equal $d_1 n_1 = d_2 n_2$ and is centered around the frequency [39]

$$\omega_B = \frac{n_1 + n_2}{4 n_1 n_2} \frac{2\pi c}{d_1 + d_2} \tag{1.52}$$

where c is the vacuum speed of light, $d_{1,2}$ are the thicknesses of the two layers and $n_{1,2}$ the respective refractive index. Notice that at the frequency ω_B corresponds a vacuum wavelength satisfying the Bragg condition $n1d_1 = n_2 d_2 = 4\lambda_B$. The reason why the gap is maximized for a quarter-wave stack is related to the property that the reflected waves from each layer are all exactly in phase at the midgap frequency. And the gap-midgap ratio at this Bragg frequency is

$$\frac{\Delta\omega}{\omega_B} = \frac{4}{\pi} \sin^{-1}\left(\frac{|n_1 - n_2|}{n_1 + n_2}\right) \tag{1.53}$$

the two above equations show that by engineering the layer optical thickness and by matching materials with sightly different refractive index it is possible to synthetize dielectric mirrors with easily tunable central frequency and with a wide spectral working range. In this infinite photonic crystal picture, the states inside the gap are strictly forbidden. As the layer number if finite the density of states forms anymore a continuum, and some states are allowed with small probability even in the forbidden region: the heterostructure reflectivity is not perfect. By using classical electromagnetic theory of continuum media it is possible to show that the reflectivity at normal incidence of N periods of Bragg matched dielectric pairs has the simple form

$$R(\omega_B) \sim 1 - 4\left(\frac{n_1}{n_2}\right)^{2N} \tag{1.54}$$

If a defect (i.e. a layer with different optical depth) is inserted in a perfect infinite photonic crystal some localized modes are created, with frequencies inside photonic band gaps. If a mode has a frequency in the gap, then it must exponentially decay once it enters the crystal. The multilayer films on both sides of the defect behave like frequency-specific mirrors. If two such films are oriented parallel to one another, any photon propagating along the growt direction trapped between them will just bounce back and forth between these two mirrors. And because the mirrors localize light within a finite region, the cavity modes are quantized into discrete frequencies. A Fabry-Pérot cavity (FPC) can be set up by facing two DBR enclosing a spacer with $\alpha\lambda/2$ optical thickness, with $\alpha \in \mathbb{N}_0$. We show a schematic of the DBR and FPC in figure 1.9 (b) and (c) respectively.

1.3.1 Transfert matrix method

The reflectivity spectrum $R(\omega)$ contains valuable informations on an arbitrary heterostructure with a finite layer number, we here show a simple iterative method for its calculation. Lets write a plane wave propagating in a material of refractive index n along the $\hat{z}$ direction as a sum of a transmitted and reflected standing waves

$$E(z) = \tilde{A}(z) + \tilde{B}(z) = A(z)e^{-i\beta z} + B(z)e^{+i\beta z} \tag{1.55}$$

where $A, B \in \mathbb{R}$ are the transmitted and reflected wave amplitudes and $\beta = 2\pi n/\lambda$ with λ the vacuum wavelength of the incident radiation. If the refractive index is omogeneus the propagation for a length L in the layer modifies only the wavepacket phase, this can be modeled by the matrix

$$P(L, n_i) = \begin{pmatrix} e^{-i\beta_i L} & 0 \\ 0 & e^{i\beta_i L} \end{pmatrix} \tag{1.56}$$

and $\beta = 2\pi n_i/\lambda$. The wavepacket at the depth L can be written in vector form as $E(L) = (\tilde{A}(L), \tilde{B}(L))^T = P(L, n_i)(\tilde{A}(0), \tilde{B}(0))^T$. Notice that we are assuming a propagation trough a non dispersive medium: if losses are non negligible they can be taken in account by turning β in the complex form $\beta = 2\pi(n_1 + in_2)/\lambda$, with n_2 related to the imaginary part of the dielectric function $\Im[\varepsilon]$ of the medium. When the wavepacket mets a refractive index discontinuity, one has to require tangetial electric field continuity which, assuming normal incidence on the interface, is equivalent to the Snell relations

$$\begin{aligned} \tilde{A}_i + \tilde{B}_i &= \tilde{A}_j + \tilde{B}_j \\ -n_i\tilde{A}_i + n_i\tilde{B}_i &= -n_j\tilde{A}_j + n_j\tilde{B}_j \end{aligned} \tag{1.57}$$

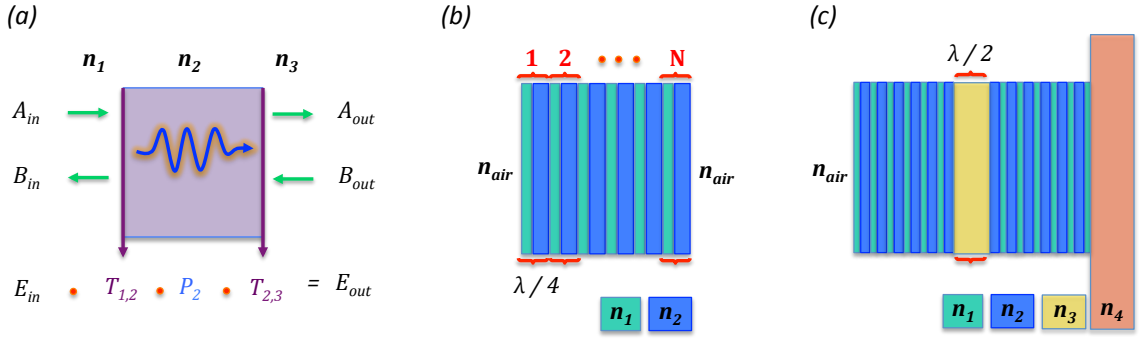

Figure 1.9: (a) Transfert matrix method mechanism schematic. (b)-A distributed Bragg reflector. (c)-Schematic of the Fabry-Pérot cavity formed by two DBRs enclosing a $\lambda/2$ spacer, the heterostructure is grown on top of a substrate.

where n_i and n_j are the refractive index of the two materials conforming the interface and $\tilde{A}_{i,j}, \tilde{B}_{i,j}$ are the relative wavepacket amplitudes. This requirements can be casted in the impedence matrix

$$T(n_i, n_j) = \begin{pmatrix} \frac{n_i+n_j}{2n_i n_j} & \frac{n_i-n_j}{2n_i n_j} \\ \frac{n_i-n_j}{2n_i n_j} & \frac{n_i+n_j}{2n_i n_j} \end{pmatrix} \tag{1.58}$$

which modifies the relative weights at the interface. The propagation of the wavepaket trough a arbitrary heterostructure can be obtained by ordered multiplication of P and T matrices. If χ is the matrix resulting from the multiplication of all the P and T factors, the reflectio coefficient can be calculated as

$$R(\lambda) = \left| \frac{n_a\chi_{11} - n_s\chi_{22} + n_a n_s\chi_{12} - n_a\chi_{21}}{n_a\chi_{11} + n_s\chi_{22} + n_a n_s\chi_{12} + n_a\chi_{21}} \right|^2 \tag{1.59}$$

where n_a and n_s are refractive indexes of the two mediums enclosing the heterostructure. The total tranfert matrix for the DBR and FPC depicted in figure 1.9 (b) and (c), with the shorthand notation $P_i = P(n_i, \lambda/4n_i)$, $T_{i,j} = T(n_i, n_j)$ reads

$$\chi^N_{DBR}(n_a, n_s, n_1, n_2) = T_{a,2} \cdot [P_2 T_{2,1} P_1 T_{1,2}]^N \cdot T^{-1}_{1,2} \cdot T_{1,s} \tag{1.60}$$

$$\chi^N_{FPR}(n_a, n_s, n_1, n_2) = \chi^N_{DBR}(n_a, n_2, n_1, n_2) \cdot P\left(\frac{\alpha\lambda}{2n_2}, n_2\right) \cdot \chi^N_{DBR}(n_2, n_s, n_2, n_1) \tag{1.61}$$

and (n_a, n_s, n_1, n_2) are respetively the index of refraction of the environment, of the substrate and of the Bragg matched layers (we assume $n_2 > n_1$), $\alpha \in \mathbb{N}$ sets the $n2$ spacer optical depth. In C2N labs $Al_xGa_{1-x}As$ based heterostructures are grown with state of the art optical quality. The

last ingredient to perform reflectance calculations is therefore to know $Al_xGa_{1-x}As$ refractive index as a function the relative Al concentration and wavelength. A model for the Sellmeier's equation for $Al_xGa_{1-x}As$ alloys was proposed back in 1974 by M.A. Afromowitz [40] and reads

$$n(E) = \sqrt{1 + \Lambda_1 + \Lambda_3 E^2 + \frac{\eta}{\pi} E^4 \log\left(\frac{E_f^2 - E^2}{E_\Gamma^2 - E^2}\right)} \tag{1.62}$$

$$E_f = \sqrt{2E_0^2 - E_\Gamma^2)} \tag{1.63}$$

$$\eta = \frac{\pi E_d}{2E_0^3(E_0^2 - E_\Gamma^2)} \tag{1.64}$$

$$\Lambda_1 = \frac{\eta}{2\pi}(E_f^4 - E_\Gamma^4) \tag{1.65}$$

$$\Lambda_2 = \frac{\eta}{\pi}(E_f^2 - E_\Gamma^2) \tag{1.66}$$

where $E = \hbar\omega$ is the incident photon energy and the parameters (E_Γ, E_f, E_0) are respectively the alloy direct bandgap at the Γ point, the dispersion energy and effective oscillator strength energy and depends on the alloy composition x as

$$\begin{aligned} E_\Gamma(x) &= 1.424 + 1.266x + 0.26x^2 \\ E_f(x) &= 36.1 - 2.45x \\ E_0(x) &= 3.65 + 0.871x + 0.179x^2 \end{aligned} \tag{1.67}$$

and are empirical formulae coming from best fit of experimental data. The formula holds within 3% in the range $\lambda = (0.7 - 2.0)\ \mu m$. Typical alloy doublets for the fabrication of DBRs are $(x_1, x_2) = (0.95, 0.10)$, which have a room temperature refractive index of

$Al_{0.95}Ga_{0.05}As$	$Al_{0.1}Ga_{0.9}As$
$n_1 \approx 3.02$	$n_2 \approx 3.57$

We show in figure 1.10 the room temperature reflectivity plots for a DBR and a FPC as a function of the incident radiation wavelength λ and of the pair number. We chose the alloy doublet $(x_1, x_2) = (0.95, 0.10)$, a GaAs substrate $x_s = 0$ and air as environment. With these simulations is possible to carefully design the Fabry-Pérot cavity in which one wants to embed the QW and provide valuable information on the coupling efficiency of the structure with incident radiation

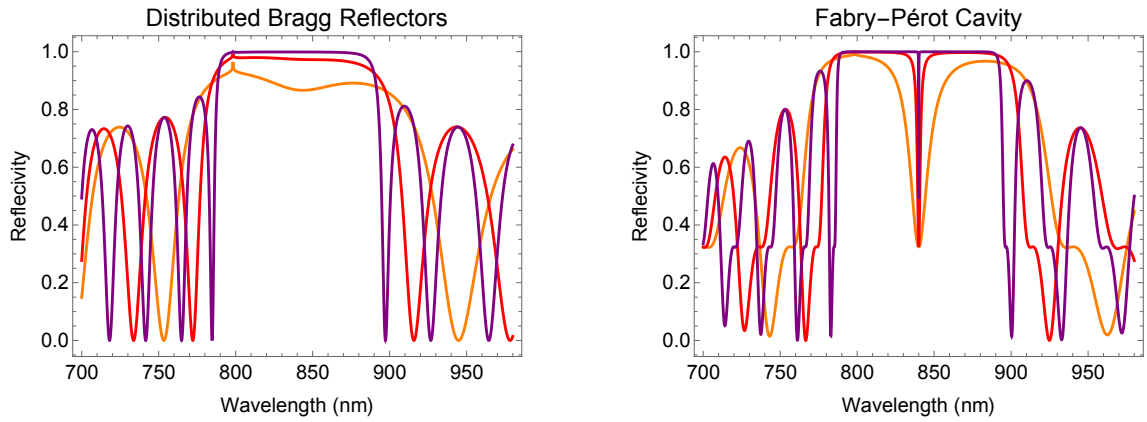

Figure 1.10: Reflectivity of a DBR with $N = (10, 15, 25)$ layer pairs are plotted respectively in orange, red and violet in panel (a). The central Bragg wavelength is $\lambda_B = 840\,nm$, we obtain for the three pair numbers a λ_B-reflectivity of $(86.8, 97.4, 99.9)\%$ in good agreement with equation (1.54). In panel (b) we plot the reflectivity of a $\lambda/2$ FPC cavity enclosed within DBRs with $N = (10, 15, 25)$ pairs. The reflectivity at the cavity resonant frequency is almost independent of N and equals 32%.

1.3.2 Cavity mode dispersion and linewidth

A Fabry-Pérot cavity created by two DBRs and a spacer can be mapped in the simpler case of two planar metallic mirrors by introducing the effective cavity length $L_{eff} = L_c + L_{DBR}$ where L_c is the optical depth of the spacer and L_{DBR} is the penetration depth of the electromagnetic field inside the stop band and has the simple form

$$L_{DBR} = \frac{\lambda}{2} \frac{n_1 n_2}{n_{cav}(n_2 - n_1)} \tag{1.68}$$

and n_cav is an effective averaged refractive index of refraction for the whole heterostructure. The condition for constructive interference in a round trip in the cavity the becomes

$$\left(\frac{n_{cav}^2 \omega^2}{c^2} - k_{\|}^2 \right)^{\frac{1}{2}} L_{eff} = \alpha\pi \quad , \quad \alpha \in \mathbb{N} \tag{1.69}$$

where $\mathbf{k}_{\|}$ is the in plane momentum of the photon, orthogonal to the growt $\hat{z}$ direction, ω the incident photon frequency and n_cav an effective mean refractive incex value for the whole FPC. At normal incidence $\mathbf{k}_{\|} = \mathbf{0}$ and the above equation gives the Bragg condition

$$\lambda_\alpha = \frac{2L_{eff}}{n_{cav}\alpha} \tag{1.70}$$

and the lowest allowed cavity mode corresponds to a Bragg wavelength twice the optical length of the effective cavity. Usually is convenient to operate the cavity in one of the lowest mode in order to have a energy separation with neighbouring modes big enough to disregard their

influence on the optical properties of the cavity. In these conditions the cavity mode dispersion can be written as

$$E(\mathbf{k}) = \frac{\hbar c}{n_{cav}}|\mathbf{k}| = \frac{\hbar c}{n_{cav}}\sqrt{k_\perp^2 + k_\parallel^2} \tag{1.71}$$

and $k_\perp = 2\pi n_{cav}\lambda_\alpha^{-1}$, fixed by the Bragg resonant condition. Under the assumption of small in plane momentum we can Taylor expand this relation around $\mathbf{k}_\parallel = \mathbf{0}$ to get

$$E(\mathbf{k}) \approx \frac{\hbar c}{n_{cav}}\left(k_\perp + \frac{k_\parallel^2}{2k_\perp}\right) \tag{1.72}$$

Its noteworthy that the cavity photon dispersion is non vanishing at $\mathbf{k}_\parallel = \mathbf{0}$, and depends in a quadratic rather than linear form on $\mathbf{k}_\parallel$ as one expects for free photons. The $\mathbf{k}_\parallel = \mathbf{0}$ implicitly defines an effective rest mass for the cavity photons in the form

$$m_{ph}^* = \frac{2\pi\hbar}{c\lambda_\alpha} = \frac{\hbar\pi n_{cav}}{cL_{cav}}\alpha \tag{1.73}$$

the straightforward consequence of a rest mass for the photons is the acquisition of a non vanishing chemical potential, this allows a cavity photon gas to thermalize and eventually condense in its ground state in analogy (the system is intrinsically lossy and has a dynamical steady state) with the Bose Einstein Condensation of an ultracold rare gas. The condensation and thermalization of cavity photons was experimentally achieved at room temperature in 2010 by J.Klaers M. Weitz and collaborators in Bohn. The possibility of observing this transition at room temperature (where for atomic gases $T_c \approx 100\,nK$) is due to the very low cavity photon effective mass which implies an associated de Broglie wavelength much bigger than the atomic case. A typical effective mass in AlGaAs based heterostructures is $m_{ph}^* \sim \cdot 10^{-5} m_e$ where $m_e$is the electron rest mass.

Another important quantity characterizing the FPC is the linewidth of the λ_α resonance and is directly connected to the cavity photon average lifetime. At normal incidence and assuming symmetric DBRs with reflectivity R, the cavity photon linewidth reads

$$\gamma_{ph} = \frac{c}{n_{cav}\,L_{eff}}\frac{1-R}{2\sqrt{R}} \tag{1.74}$$

and the cavity quality factor for the FPC is

$$Q = \frac{\pi\sqrt{R}}{1-R} \tag{1.75}$$

which is the average number of round trips of a photon in the cavity before escaping. For the typical parameters of FPC fabricated at C2N the linewidth can be as low as $(10 \div 20)\mu eV$ corresponding to a lifetime of $\sim (32 \div 60)\ ps$ and Q-factors up to 40000. Another relevant

effect of great importance couple the QW exciton to the cavity mode is that the electric field gets enhanced in the center of $\lambda/2$ FPC by a factor of

$$\xi(\omega) = \frac{|F(\omega)|^2}{|F_0|^2} = \frac{1-R(\omega)}{(1-R(\omega))^2 + 4\sqrt{R(\omega)}\sin^2\left(\frac{1}{2}k_\perp L_c + \varphi_r(\omega)\right)} \tag{1.76}$$

where F_0 is the amplitude of the incident electromagnetic field, and $\varphi_r(\omega)$ is the round trip phase acquired by a photon in the cavity mode. Within half of the stopband this phase has the linear form

$$\varphi_r(\omega) = \frac{n_s L_{DBR}}{c}(\omega - \omega_\alpha) \tag{1.77}$$

With the above mentioned FPC parameters $\xi(\omega)$ can be up to some thousands, meaning the effective dipolar coupling felt by a QW exciton embedded at the center of the spacer with the cavity field is huge compared to the one with free space optical modes.

1.4 Exciton-Polaritons

We want now to see what happens when a QW is embedded in a Fabry-Pérot cavity, the system is intersting because the fundamental excitations of the QW can absorb and emit photons, if the exciton absorption line is quasi-resonant with a FPC mode, a cavity photon may be repeatedly absorbed and re emitted by the QW excitons. If the rate of this process is faster than the losses, as we have seen in section 1.1, the cavity photon and QW well exciton are in a strong coupling regime and the fundamental excitations of this hybrid system are quasiparticles we call exciton-polaritons inheriting properties of both the photonic and excitonic component. We schematize the system in figure 1.11.

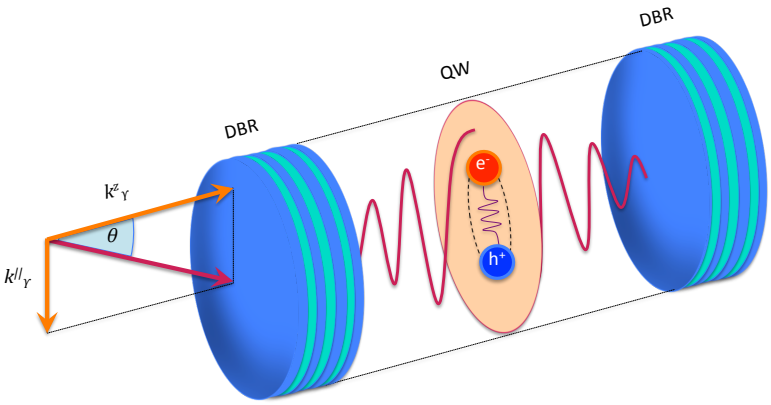

Figure 1.11: A quantum well embedded in a cavity is the prototype system to achieve exciton polariton states. Due to in plane traslational symmetry of the system, the cavity photons can only couple to free space modes with an equal in plane momentum. Therefore exits a one to one relation between the angle of emission of a photon and the in plane momentum of the exciton which recombined in the QW.

To model the system we use a second quantization picture along the lines of the inspiring review work by Carusotto and Ciuti "Quantum Fluids of Light" [8], the proposed formalism is the correct quantum representation of polariton physics, but often a mean-field semiclassical description is handy, we will first introduce the general framework and in a second time we will show how to apply the mean field approximation.

In the previous two sections we studied the bare cavity photon and quantum well exciton dispersion and we showed within some approximations they both have a parabolic like dispersion, however the typical heavy-exciton mass is order of the electron mass while the cavity photon effective mass is order of $10^{-5} m_e$, thus the exciton band curvature is much less than the cavity photon one and in the range of validity of the parabolic band approximation for $E_{cav}(\mathbf{k}_{\|})$, the exciton dispersion appears flat $E_X(\mathbf{k}_{\|}) \approx E_X = const$.

As discussed before, both the cavity and the excitons are intrinsically lossy, out of equilibrium systems. We firstly will assume to work with an idealized heterostructure where the coupling with the enviroment is zero: the exciton photon system is isolated. As we discussed in section 1.1 such a system is always strongly coupled as soon as the coupling constant is non zero [32]. We will introduce the losses in a second moment, and we will discuss the strong coupling criterion for a exciton-cavity photon two level system and polariton-polariton effective interactions.

1.4.1 Exciton-Polaritons as an isolated system

Within the above mentioned assumptions we can write the bare cavity photon normal-ordered hamiltonian as

$$H_{cav} = \int \frac{d^2\mathbf{k}}{(2\pi)^2} \sum_{\sigma} \hbar\omega_{cav}(\mathbf{k}) a^{\dagger}_{c,\sigma}(\mathbf{k}) a_{c,\sigma}(\mathbf{k}) \tag{1.78}$$

where $\mathbf{k}$ is the in plane wave-vector of the cavity photon, $a^{\dagger}_{c,\sigma}(\mathbf{k})$ is the creation operator of a cavity photon with polarization σ and in plane wave-vector $\mathbf{k}$ and $a_{c,\sigma}(\mathbf{k})$ is the corresponding destruction operator. The photon creation and destruction operator satisfy standard Bose-Einstein equal time commutation rules

$$[a_{c,\sigma}(\mathbf{k}), a^{\dagger}_{c,\sigma}(\mathbf{k}')]_{ET} = (2\pi)^2 \delta(\mathbf{k}-\mathbf{k}')\delta_{\sigma,\sigma'} \tag{1.79}$$

The in plane real space cavity photon fields $\Psi_{C,\sigma}(\mathbf{r})$, $\Psi^{\dagger}_{C,\sigma}(\mathbf{r})$ are defined trough

$$\Psi_{C,\sigma}(\mathbf{r}) = \int \frac{d^2\mathbf{k}}{(2\pi)^2} a_{c,\sigma}(\mathbf{k}) e^{i\mathbf{k}\cdot\mathbf{r}} \tag{1.80}$$

and $\Psi^{\dagger}_{C,\sigma}(\mathbf{r})$ is defined by the the hermitian conjugate relation. The bare $2D$-exciton hamiltonian in a similar way reads

$$H_{exc} = \int \frac{d^2\mathbf{k}}{(2\pi)^2} \sum_{\sigma} \hbar\omega_{exc}(\mathbf{k}) a^{\dagger}_{X,\sigma}(\mathbf{k}) a_{X,\sigma}(\mathbf{k}) \tag{1.81}$$

but now $\omega_{exc}(\mathbf{k}) \approx \omega_{exc}$ is the 2D exciton dispersion and $a^{\dagger}_{X,\sigma}$, $a_{X,\sigma}$ respectively creates or destroy an exciton with angular momentum projection σ, recall that only excitons with $\sigma = \pm 1$ are optically active for a plane wave excitation in dipole approximation as discussed in section 1.2.3. Provided that the exciton density in the quantum well plane is such that interparticle distance is larger than their Bohr radius, the exciton creation and destruction operator satisfies Bose commutation rules. However small corrections can be included trough a density and spin dependent correction to the pure Bose commuting rule (Combescot CITA). We have now to recount for the coupling between the cavity field and the excitons, in particular one is interested

in calculating the leading dipolar interaction strength. In general this issue can be addressed in a first quantization picture applying the minimal coupling ansatz in the bare exciton hamiltonian along with the Fermi golden rule and dropping the second order terms in the electromagnetic field potential. This gives the coupling with free space optical modes, the presence of the cavity however greatly enhances the electro-magnetic field inside the cavity, in general the coupling strenght will have the form

$$g = \hbar\Omega_R \propto \xi(Q)P_{if} \tag{1.82}$$

the quantity Ω_R is often called Rabi frequency, P_{if} has the form (1.41) and $\xi(Q)$ is the elctro-magnetic field enhancement provided by the cavity dependent The bracket can be calculated once the confined electron and hole wavefunction in the form of equation (1.49) are known. The calculation can be cumbersome, we refear to [41]-[42] for the details; in case of a single QW placed at the maximum of the cavity field g reads

$$g = \hbar\left(\frac{4\pi\omega_{cav}(\mathbf{0})}{L_{eff}}f_{2D}\right)^{\frac{1}{2}} \approx \hbar\left(\frac{2c\Gamma_0}{n_{cav}L_{eff}}\right)^{\frac{1}{2}} \tag{1.83}$$

where Γ_0 is the exciton radiative lifetime and f_{2D} is oscillator strength surface density and is proportional to the square of the 2D exciton Bohr radius. The righ-most relation was extracted assuming a DBR reflectivity $R \sim 1$, for a single quantum well in GaAs based heterostructures $g \approx 1.7\ meV$. The coupling also scales with the number of the quantum wells, indeed if N_{QW} are present in the cavity, $N_{QW} - 1$ linear combinations of the exciton states are dark [8], while the single bright one is coupled to the cavity with an enhanced coupling constant

$$\tilde{g} = \hbar\sqrt{\sum_i^{N_{QW}} (\Omega_R^i)^2} \sim \sqrt{N_{QW}}g \tag{1.84}$$

its noteworthy that the presence of the cavity eliminates the quantum well exciton radiative coupling to free space modes which can only happen via the cavity lossy mode [42]. If the excitonic (hh-lh) level spacing is much greater than their linewidth ($\Delta E/\Gamma_0 \gtrsim 15 \div 20$ in GaAs based 80Å width QW) and the same holds for the cavity mode, we can describe the system within the so called two level approximation where just one optical mode is coupled to a two level system reresented by the QW ground state and by the creation of an (heavy hole) exciton. The system is a syntetic two-level atom embedded in a cavity which light matter interaction can be described by a Jaynes-Cummings term

$$H_{JC} = \int \frac{d^2\mathbf{k}}{(2\pi)^2}\sum_\sigma g\left[a^\dagger_{X,\sigma}(\mathbf{k})a_{c,\sigma}(\mathbf{k}) + a^\dagger_{c,\sigma}(\mathbf{k})a_{X,\sigma}(\mathbf{k})\right] \tag{1.85}$$

and g is specified by equation (1.83). The antiresonant terms proportional to $a^\dagger_{X,\sigma}(\mathbf{k})a^\dagger_{c,\sigma}(\mathbf{k})$ and $a_{X,\sigma}(\mathbf{k})a_{c,\sigma}(\mathbf{k})$ can be safely neglected since they are associated in an interaction picture to

fast oscillating terms which have average null contribution to the coupled system dynamics as soon as $2\Omega_R = g\hbar^{-1} \ll (\omega_{exc} + \omega_{cav})$ and $(\omega_{cav} - \omega_{exc}) \ll (\omega_{exc} + \omega_{cav})$. In our samples these requirements are always matched and a typical $2\Omega_R/(\omega_{exc} + \omega_{cav})$ is 10^{-3}. We can write now the total hamiltonian in a matrix form in the $\Psi_\sigma(\mathbf{k}) = (a_{c,\sigma}(\mathbf{k}), a_{X,\sigma}(\mathbf{k}))$ basis as

$$H_{pol} = H_{cav} + H_{exc} + H_{JC} = \int \frac{d^2\mathbf{k}}{(2\pi)^2} \sum_\sigma \Psi^\dagger_\sigma(\mathbf{k}) \Xi(\mathbf{k}) \Psi_\sigma(\mathbf{k}) \tag{1.86}$$

where

$$\Xi(\mathbf{k}) = \begin{pmatrix} \hbar\omega_{cav}(\mathbf{k}) & g \\ g & \hbar\omega_{exc}(\mathbf{k}) \end{pmatrix} \tag{1.87}$$

The hamiltonian kernel can be diagonalized by means of a unitary transformation

$$\tilde{\Theta} = \begin{pmatrix} X(\mathbf{k}) & C(\mathbf{k}) \\ -C(\mathbf{k}) & X(\mathbf{k}) \end{pmatrix} \tag{1.88}$$

with the requirement $det(\tilde{\Theta}) = X(\mathbf{k})^2 + C(\mathbf{k})^2 = 1$. The explicit form of the X and C coefficients can be determined once the eigenvalues of the hamiltonian kernel are known. After some algebra one gets

$$\omega_{UP}(\mathbf{k}) = \frac{\omega_{cav}(\mathbf{k}) + \omega_{exc}(\mathbf{k})}{2} + \sqrt{\Omega_R^2 + \frac{1}{4}\left(\omega_{cav}(\mathbf{k}) - \omega_{exc}(\mathbf{k})\right)^2} \tag{1.89}$$

$$\omega_{LP}(\mathbf{k}) = \frac{\omega_{cav}(\mathbf{k}) + \omega_{exc}(\mathbf{k})}{2} - \sqrt{\Omega_R^2 + \frac{1}{4}\left(\omega_{cav}(\mathbf{k}) - \omega_{exc}(\mathbf{k})\right)^2} \tag{1.90}$$

descibing the so called upper and lower polariton branch dispersions relative to the new diagonalized hamiltonian eigenstates. The eigenvectors of the kernel can be expressed in the old $\Psi_\sigma(\mathbf{k}) = (a_{c,\sigma}(\mathbf{k}), a_{X,\sigma}(\mathbf{k}))$ basis via the $\tilde{\Theta}$ matrix: $\tilde{\Psi}_\sigma(\mathbf{k}) = \tilde{\Theta}\,\Psi_\sigma(\mathbf{k})$, since

$$\Psi^\dagger\,\Xi\,\Psi = \Psi^\dagger\,[\tilde{\Theta}^{-1}\tilde{\Theta}]\,\Xi\,[\tilde{\Theta}^{-1}\tilde{\Theta}]\,\Psi = \tilde{\Psi}^\dagger\,\tilde{\Xi}\,\tilde{\Psi} \tag{1.91}$$

and $\tilde{\Xi}$ is the diagonal matrix $diag(\omega_{UP}, \omega_{LP})$. The new creation and destruction operators can be defined trough

$$\tilde{\Psi} = \begin{pmatrix} a_{UP,\sigma}(\mathbf{k}) \\ a_{LP,\sigma}(\mathbf{k}) \end{pmatrix} = \begin{pmatrix} X(\mathbf{k})a_{c,\sigma}(\mathbf{k}) - C(\mathbf{k})a_{X,\sigma}(\mathbf{k}) \\ C(\mathbf{k})a_{c,\sigma}(\mathbf{k}) + X(\mathbf{k})a_{X,\sigma}(\mathbf{k}) \end{pmatrix} \tag{1.92}$$

this tells us that the eigenstates of H_{pol} can be interpreted as mixed light matter states we call upper and lower polaritons moreover, since a_{UP} and a_{LP} can be written as linear superposition of the a_c and a_X states, the polariton field inherits properties of both the light and matter fields.

This simple observation is at the very heart of the interest in polaritons and strongly coupled light matter sytems in general, as we anticipated in the introduction of chapter 1. Indeed if we move from an idealized picture where only one excitation is present in the system and we look at a polariton gas, the excitonic component provides an effective polariton-polariton interaction term and the photonic field provides both a way to confine polaritons trough refractive index landscape engineering and a probe on the system thanks to the radiative coupling to the environment. The first experimental realization of QW exciton-cavity photon strong coupling was achieved by Weisbuch and collaborators in 1992 [7].

The $X(\mathbf{k})$ and $C(\mathbf{k})$ coefficients can be easily determined imposing $det(\tilde{\Theta}) = 1$ and solving the eigenvector characteristic linear equation system. The result is

$$X(\mathbf{k})^2 = \frac{1}{2}\left(1 + \frac{\omega_{cav}(\mathbf{k}) - \omega_{exc}(\mathbf{k})}{\sqrt{4\Omega_R^2 + (\omega_{cav}(\mathbf{k}) - \omega_{exc}(\mathbf{k}))^2}}\right) \tag{1.93}$$

$$C(\mathbf{k})^2 = \frac{1}{2}\left(1 - \frac{\omega_{cav}(\mathbf{k}) - \omega_{exc}(\mathbf{k})}{\sqrt{4\Omega_R^2 + (\omega_{cav}(\mathbf{k}) - \omega_{exc}(\mathbf{k}))^2}}\right) \tag{1.94}$$

these coefficients are often referred as Hopfield coefficients, in honour to J.J. Hopfield pionering work, dating back to 1958, on the contribution of excitons to the complex dielectric constant of crystals [43].

We plot in figure 1.12 the upper and lower polariton bands, along with the bare exciton and photon dispersions and the Hopfield coefficients for the three bare exciton-cavity detuning $\delta_0 = (\omega_{cav}(0) - \omega_{exc}(0)) = (+2\Omega_R, 0, -2\Omega_R)$. We set in the plot some realistic parameters for our system: a bare exciton energy of $\hbar\omega^0_{exc} = 1.48\ eV$, a $\Omega_R = 1.4\ meV$ Rabi oscillation frequency and $n_{cav} \approx 3.6$.

Some intersting properties of polaritons are suggested by the graphs: first we notice that in this closed quantum system description the polariton dispersion shows a clear anticrossing phenomenon indeed for negative detunings $\delta_0 < 0$, where close to $|\mathbf{k}| = 0$, $\omega_{UP} \approx \omega_{exc}$ and $\omega_{LP} \approx \omega_{cav}$, for larger wave vectors $\omega_{UP} \approx \omega_{cav}$ and $\omega_{LP} \approx \omega_{exc}$. This anticrossing phenomenon, as discussed in section 1.1, is one of the three signatures of strong coupling regime. Close enough to $|\mathbf{k}| = 0$ the polariton bands have parabolic like dispersion: by Taylor expanding up to second order $\omega_{UP,LP}(\mathbf{k})|_{k=0}$ it is possible to calculate the upper and lower polariton effective masses, which reads

$$m^*_{UP} = \frac{m^*_X m^*_{ph}}{X^2(\mathbf{0})m^*_{ph} + C^2(\mathbf{0})m^*_X} \approx \frac{m^*_{ph}}{C^2(\mathbf{0})} \tag{1.95}$$

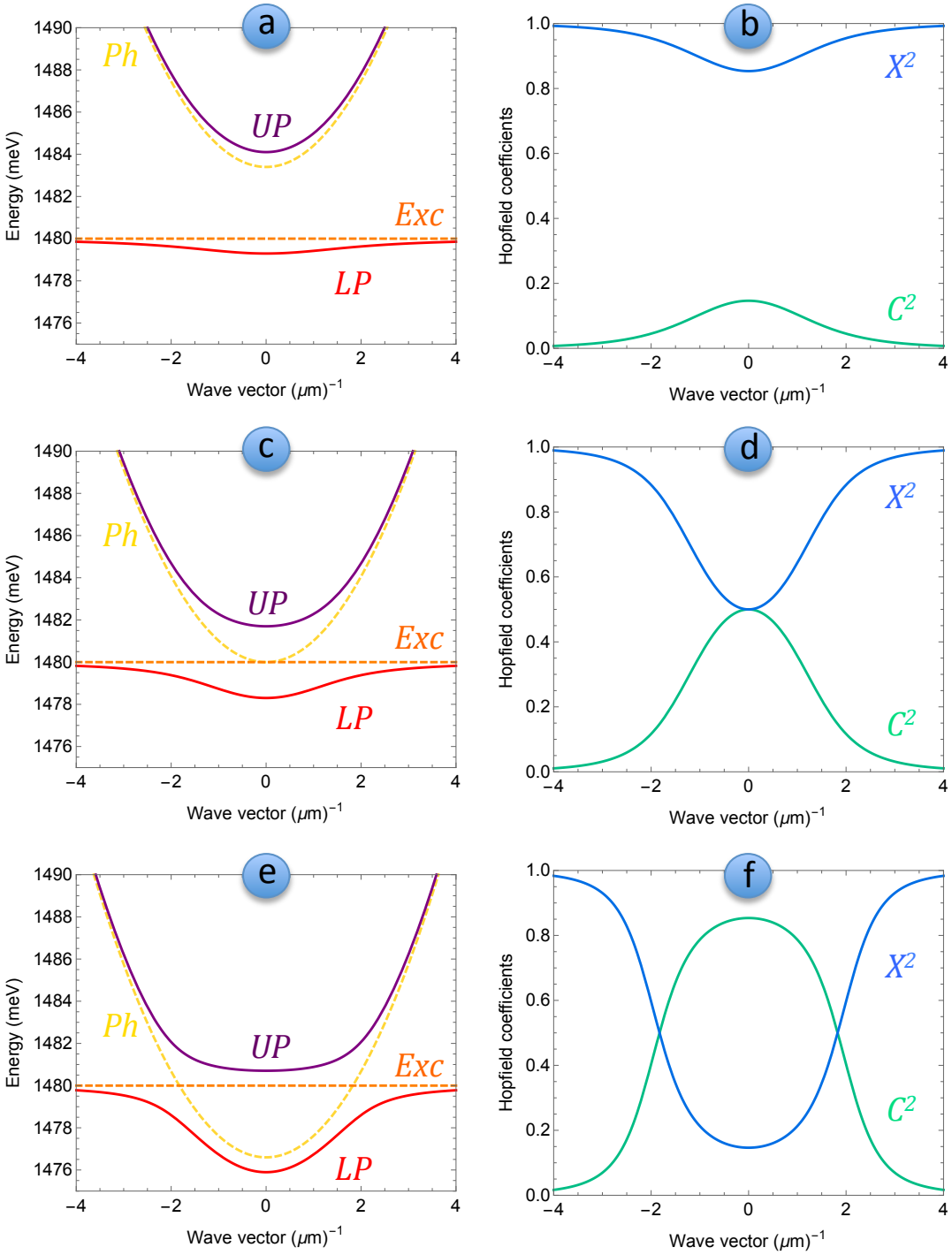

Figure 1.12: Panels (a-c-e) Upper and lower polariton dispersion according to equation (1.89)-(1.90), dashed curves are the bare QW exciton and cavity photon parabolic dispersions, respectively calculated for the zero wave vector exciton-photon detuning $\delta_0 = (+2\Omega_R,\ 0,\ -2\Omega_R)$. In (b-d-f) we show the Hopfield coefficients associated to the (a,c,e) plots. interestingly the lower polariton at zero wave vector is mostly photonic or excitonic depending on the detuning sign, which can be tuned in order to obtain a specific exciton-photon admixture.

$$m^*_{LP} = \frac{m^*_X m^*_{ph}}{X^2(\mathbf{0})m^*_X + C^2(\mathbf{0})m^*_{ph}} \approx \frac{m^*_{ph}}{X^2(\mathbf{0})} \tag{1.96}$$

where we used the fact that $m^*_X/m^*_{ph} \sim 5 \cdot 10^4$ in the whole region where the cavity dispersion can be aproximated as parabolic. For typical values of the bare exciton-cavity detuning this implies $m^*_{LP} \sim (2 \div 20)m^*_{ph}$, meaning polariton have a very low effective mass order of 10^{-4} times the rest mass of the electron.

1.4.2 Exciton-Polaritons as an open quantum system

A quantum description of the pumping and losses processes which describe the coupling between the cavity and the external environment requires a generalization of the standard hermitian time evolution of the system. Non hermitian terms must be added and the density matrix master equation has the form [8]

$$\frac{d\rho}{dt} = \frac{1}{i\hbar}[H,\rho] + \mathscr{L}[\rho] \tag{1.97}$$

where ρ is the system density matrix, H is a non neccessarily hermitian hamiltonian and $\mathscr{L}[\rho]$ is the density matrix dependend superoperator recounting for all the dissipative processes due the coupling with the environment. In particular a coherent external field driving the cavity (i.e. a laser), can be modeled with a non hermitian term

$$H_{pump} = i\hbar \int \frac{d^2\mathbf{k}}{(2\pi)^2} \sum_\sigma [\eta_\sigma(\mathbf{k})\tilde{E}_\sigma(\mathbf{k},t)a^\dagger_{c,\sigma}(\mathbf{k}) - \eta^*_\sigma(\mathbf{k})\tilde{E}^*_\sigma(\mathbf{k},t)a_{c,\sigma}(\mathbf{k})] \tag{1.98}$$

where $\tilde{E}_\sigma(\mathbf{k},t)$ is the k-space representation of incident field and $\eta^*_\sigma(\mathbf{k})$ models the incident field coupling efficiency with the cavity modes and is proportional to the transmission coefficient of the cavity front mirror. If the temperature of the radiative modes outside the cavity is much lower than the cavity mode one $k_B T_{env} \ll \hbar\omega_{cav}$ and the radiative process is assumed Markovian (i.e. memoryless) the radiative losses can be modeled by the Lindblad superoperator [8]

$$\mathscr{L}^{rad}[\rho] = \int \frac{d^2\mathbf{k}}{(2\pi)^2} \sum_\sigma \frac{\gamma^{rad}_\sigma(\mathbf{k})}{2} (2a_{c,\sigma}(\mathbf{k})\rho a^\dagger_{c,\sigma}(\mathbf{k}) - \{n_{c,\sigma}(\mathbf{k}),\rho\}_{ET}) \tag{1.99}$$

where $\gamma^{rad}_\sigma(\mathbf{k})$ is the wave-vector and polarization dependent decay rate, which can be calculated using the Tranfert Matrix Method we reported in section 1.3.1, $n_{c,\sigma} = a^\dagger_{c,\sigma}a_{c,\sigma}$ is the cavity field number operator and $\{a,b\}_{ET} = ab + ba$ is the equal time anticommutator. As we already mentioned the presence of the cavity inhibts a direct coupling of the QW exciton field with the free space radiative modes. Therefore the radiative decay of the exciton determines trough equation (1.83) the Rabi coupling but enters the Lindblad superoperator as a second order correction, still some nonradiative recombination processes due to QW inhomogeneities, defects

and phonon intractions are present and dominates the exciton linewidth. This dephasing terms within the RWA can be modeled as [8]

$$\mathscr{L}^{deph}[\rho] = \int \frac{d^2\mathbf{k}}{(2\pi)^2} \sum_{\sigma} \frac{\gamma^{deph}_{X,\sigma}(\mathbf{k})}{2} \left(2n_{X,\sigma}(\mathbf{k})\ \rho\ n_{X,\sigma}(\mathbf{k}) - \{n_{X,\sigma}(\mathbf{k}) n_{X,\sigma}(\mathbf{k}), \rho\}_{ET}\right) \quad (1.100)$$

where $\gamma^{deph}_{X,\sigma}(\mathbf{k})$ is the wave-vector and polarization dependent decay rate which can be directly measured via photoluminescence experiments and $n_{X,\sigma}$ is the exciton number-density operator. Its noticeable that while $\mathscr{L}^{rad}[\rho]$ is a bilinear form in the creation and destruction operators, $\mathscr{L}^{deph}[\rho]$ is bilinear in the exciton number-density operator. This "linear" dependence on the field density for radiative processes and "quadratic" dependence on field density for the nonradiative processes reflects in a respectively Lorentzian or Gaussian eigenmode lineshape. Indeed if the time dynamics operator $U(t)$ has the Lindblad superoperator as Lie generator $Lie[U(t)] \propto \mathscr{L}$, the lineshape of the modes is associated to the fourier transform of $U(t) \propto exp[\mathscr{L}]$ and the exponential of a linear form is the generating function of a Lorentzian distribution while the exponential of a quadratic form is the generating function of a Gaussian distribution.

For some practical calculation however we can take advantage of the two level NHH model analogy with two coupled classical harmonic oscillators with a friction term. As suggested in section 1.1 in a semiclassical picture, the losses can enter the system dynamics as soon as we allow the system eigenenergies to be complex. We can write in general the lossy cavity photon and QW exciton dispersion as [42]

$$\tilde{\omega}_{cav}(\mathbf{k}) = \omega_{cav}(\mathbf{k}) - i\gamma_{cav}(\mathbf{k}) \quad (1.101)$$

$$\tilde{\omega}_{exc}(\mathbf{k}) = \omega_{exc}(\mathbf{k}) - i\gamma_{exc}(\mathbf{k}) \quad (1.102)$$

where $\gamma_{cav}(\mathbf{k})$ and $\gamma_{exc}(\mathbf{k})$ model the (eventually k-dependent) cavity and exciton loss rates. If we follow the same diagonalization procedure of the previous section, we find the complex polariton eigenvalues

$$\tilde{\omega}_{UP}(\mathbf{k}) = \frac{\tilde{\omega}_{cav}(\mathbf{k}) + \tilde{\omega}_{exc}(\mathbf{k})}{2} + \sqrt{\Omega_R^2 + \frac{1}{4}\tilde{\delta}^2(\mathbf{k})} \quad (1.103)$$

$$\tilde{\omega}_{LP}(\mathbf{k}) = \frac{\tilde{\omega}_{cav}(\mathbf{k}) + \tilde{\omega}_{exc}(\mathbf{k})}{2} - \sqrt{\Omega_R^2 + \frac{1}{4}\tilde{\delta}^2(\mathbf{k})} \quad (1.104)$$

representing the lossy upper and lower polariton branches, where $\tilde{\delta}(\mathbf{k})$ is the cavity-exciton complex detuning defined by

$$\tilde{\delta}(\mathbf{k}) = \tilde{\omega}_{cav}(\mathbf{k}) - \tilde{\omega}_{exc}(\mathbf{k}) = (\omega_{cav}(\mathbf{k}) - \omega_{exc}(\mathbf{k})) - i(\gamma_{cav}(\mathbf{k}) - \gamma_{exc}(\mathbf{k})) \tag{1.105}$$

While in the isolated cavity with no environmental coupling, if $\Omega_R \neq 0$ the two polariton bands were non degenerate, here the right most square root term in equations (1.103)-(1.104) can be imaginary and the real part of the bands becomes degenerate, in the simpler case where $\Re e[\tilde{\delta}] = 0$ this happens if $2\Omega_R < (\gamma^0_{cav} - \gamma^0_{exc})$, and the system is said to be in the weak coupling regime. The upper and lower polariton homogeneous linewidths can be written in the bare exciton-photon basis as

$$\gamma_{UP}(\mathbf{k}) = X^2(\mathbf{k})\gamma_{exc}(\mathbf{k}) + C^2(\mathbf{k})\gamma_{cav}(\mathbf{k}) \tag{1.106}$$

$$\gamma_{LP}(\mathbf{k}) = C^2(\mathbf{k})\gamma_{exc}(\mathbf{k}) + X^2(\mathbf{k})\gamma_{cav}(\mathbf{k}) \tag{1.107}$$

Usually in GaAs based heterostructures the excitonic linewidth is the dominant one, and typical polariton lifetimes are order of a dozen picoseconds.

1.4.3 Interactions, Confinement and Mean Field Approximation

Polaritons interact with other polaritons thanks to the excitonic component in their wavefunction. The description from a microscopic standpoint of the scattering process is quite complex since involves the complex Coulomb interactions between electron and holes: we refear to [44]-citeGlazov for the details. However is possible to write an effective hamiltonian modeling the interactions between excitons without invoking their elementary costituents is possible. This trick is often referred in many-body physics as bosonization procedure. As soon as the average transferred wave vector in the scattering events is small when compared to a_B^{-1} the effective hamiltonian can be cast in the form of a contact interaction

$$H_{XX} = \int d^2\mathbf{r} \sum_{\sigma,\sigma'} \frac{\Gamma^{XX}_{\sigma,\sigma'}}{2} \Psi^\dagger_{X,\sigma}(\mathbf{r})\Psi^\dagger_{X,\sigma'}(\mathbf{r})\Psi_{X,\sigma'}(\mathbf{r})\Psi_{X,\sigma}(\mathbf{r}) \tag{1.108}$$

where $(\sigma,\sigma') = \sigma_\pm$ and are the polarization indexes and $Psi_{X,\sigma}(\mathbf{r})$ is the Fourier transform of the exciton destruction operator. The interaction constant Γ^{XX} can be decomposed in a parallel spin $\Gamma^{XX}_{\sigma_+,\sigma_+} = \Gamma^{XX}_{\sigma_-,\sigma_-} = \Gamma^{XX}_{\rightrightarrows}$ and antiparallel spin $\Gamma^{XX}_{\sigma_+,\sigma_-} = \Gamma^{XX}_{\sigma_-,\sigma_+} = \Gamma^{XX}_{\rightleftarrows}$ and the rotational invariance of this interaction potential imposes that total exciton spin is conserved in the scattering. The two scattering term which originates are often called Pauli scattering terms: physically $\Gamma^{XX}_{\rightrightarrows}$ terms correspond to the exchange of an electron or hole between to excitons where $\Gamma^{XX}_{\rightleftarrows}$ correspond to the exchange of an electron with a hole between, this process needs to be mediated by biexcitons[2] or by the dark states. From the electric charge sign of the exchanged

[2] Helium like excitons composed by two electrons and two holes

particles intuitively one would say that $\Gamma^{XX}_{\rightrightarrows} > 0$ is repulsive and $\Gamma^{XX}_{\rightleftarrows} < 0$ is attractive. This is true for $\Gamma^{XX}_{\rightrightarrows}$ but for $\Gamma^{XX}_{\rightleftarrows}$ the sign depends on the dominance of the biexciton or dark state mechanism. Under circularly polarized drive the parallel spin interaction constant reads [8]-[45]

$$\Gamma^{XX}_{\rightrightarrows} = \frac{6e^2 a_B^{2D}}{\varepsilon} \tag{1.109}$$

where e is the unit charge, a_B^{2D} the exciton Bohr radius and ε is the background dielectric permittivity. And usually $\Gamma^{XX}_{\rightrightarrows} \gg \Gamma^{XX}_{\rightleftarrows}$ and the ratio depends on the pump polarization and detuning but in some conditions the biexciton creation mechanism may become resonant (biexciton Feshbach resonance) and the inequality can be flipped [8]-[46]-[44]. Other contributions to the interaction term are for instance

1- **Direct coulomb scattering**: this term since the exciton is a neutral artificial atom is trongly suppressed: in absence of external fields applyed on the microcavity the Coulomb cross section is roughly four orders of magnitude smaller than the Pauli term [45].

2- **QW electrostatic energy**: is the energy of electric charges of an electron and a hole forming an exciton in the electrostatic potential formed by other excitons. Indeed if the electron wave function penetrates into the barriers deeper than the hole wave function, the population of excitons in a QW creates an inhomogeneous charge density consisting of a positive sheet at the center of the well and two negative sheets at the edges of the well. The well acts as a plane capacitor in this case [46].

3- **Exciton saturation**: the Pauli principle forbids the creation of another exciton at a distance shorter than the Bohr radius with another exciton with the same spin. This term can be modeled at the lower order in the exciton density by another quartic hamiltonian with a positive intercation constant. In general the exciton saturation term is smaller than the other contributions up to very high densities [45].

In most of the relevant experimental conditions one can restrict to work with the lower polariton branch, if we write the interaction hamiltonian in the polariton basis, it reads

$$H_{LP-LP} = \int \frac{d^2\mathbf{k}}{(2\pi)^2} \sum_{\sigma,\sigma'} \frac{\Gamma^{LP}_{\sigma,\sigma'}(\mathbf{k})}{2} a^{\dagger}_{LP,\sigma}(\mathbf{k}) a^{\dagger}_{LP,\sigma'}(\mathbf{k}) a_{LP,\sigma'}(\mathbf{k}) a_{LP,\sigma}(\mathbf{k}) \tag{1.110}$$

with

$$\Gamma^{LP}_{\sigma,\sigma'}(\mathbf{k}) \approx |X(\mathbf{k})|^4 \Gamma^{XX}_{\rightrightarrows} \tag{1.111}$$

where $X(\mathbf{k})$ is the hopfield coefficient related to the excitonic component in the lower polariton band.

Another intersting question is how is possible to implement spatial and spin-dependent external potentials. Many strategies were developed in the past years to build scalar (i.e. spin independent) potentials, we briefly list some of them:

- **Surface Acoustic Waves**: originally developed by P. Santos and collaborators in Berlin, allows to modulate the exciton energy via the spatially patterned strain field produced by the surface acoustic waves (SAW) propagating in the sample. The SAW also affects the photonic component by introducing a change in the thickness and refractive index of the cavity layer. One or two trains of surface acoustic waves can be used to create 1D or 2D lattices. However the potential modulation is limited by the smallest sound wavelength.

- **Mechanical Stress**: developed in the group of D. Snoke, allows to change the exciton energy by using a tip which pushes on the back side of the sample. The confining mechanism is similar to the SAW one, but here the strain is applied by means of pressure.

- **Optical Manipulation**: this technique was originally proposed by A. Amo and S. Pigeon, was successfully developed in many groups. A repulsive potential can be achieved by means of a strong "trap" laser field injecting σ_- polaritons with a real space desity profile reminscent of the laser spot shape, which can interact with σ_+ polaritons excited by a second "pump" laser. The advantage of this technique is the possibility to create potentials with almost arbitrary shapes down to μm size which can be also modulated on short time scales.

- **Surface Metal Deposition**: developed in the group of Y. Yamamoto, introduces a local change in the dielectric constant of a cavity by depositing a patterned thin metallic layer on top of the sample. 1D and 2D periodic potentials can be obtained.

- **Overgrowth Techniques**: this technique was developed by the group of B. Deveaud and consists in modulating the cavity spacer width by a post-growth selective etching technique: in correspondence of the spacer width discontinuity an in plane photonic band gap is created thus laterally confining the polaritons.

- **Post-growth Etching Techniques**: consists in the deep spatially patterned etching of the microcavity planar structure structure after the growth process. The etching involves all the layers forming the top mirror, the cavity layer and the lower mirror down to the substrate. The huge refractive index mismatch at the air-semiconductor inteface provides an almost squared confinement potential, with this technique is possible to grow structures with arbitrary shapes down to micron sized pillars. We will discuss in detail in the next chapter this technique since is the one used in C2N labs for the sample growt.

In general the interactions can be modeled with an hamiltonian term

$$H_{ext} = \int d^2\mathbf{r} \sum_{\sigma,\sigma'} [\, V^{cav}_{\sigma,\sigma'}(\mathbf{r})\Psi^{\dagger}_{c,\sigma}(\mathbf{r})\Psi_{c,\sigma'}(\mathbf{r}) + V^{exc}_{\sigma,\sigma'}(\mathbf{r})\Psi^{\dagger}_{X,\sigma}(\mathbf{r})\Psi_{X,\sigma'}(\mathbf{r})\,] \tag{1.112}$$

which can be cast in the lower polariton and higher polariton band basis by means of the unitary transformation $\tilde{\Theta}$.

We are now interested in the derivation of an equation describing the non trivial dynamics of the polariton gas in the cavity. In particular the interaction terms describing exciton-exciton collisions make the dynamics non trivial and are responsible for a number of nonlinear and quantum phenomena. If again for simplicity we neglect the lossy lindblad terms, the time evoultion operator for the coherent fields $\Psi_{UP,LP}(\mathbf{r},t)$ can be writtem in the path integral formulation as

$$\mathscr{U}(\,\Psi^*_{\alpha,f},\, t_f,\, \Psi_{\alpha,i},\, t_i\,) = \int \mathscr{D}[\Psi^*_{\alpha}(t)]\mathscr{D}[\Psi_{\alpha}(t)]\; exp\left(\frac{i}{\hbar}S[\Psi^*_{\alpha},\Psi_{\alpha}]\right) \tag{1.113}$$

where $\beta = (k_B T)^{-1}$, the indexes i, f label the initial and final states, $\mathscr{D}[\Psi^*_{\alpha}(t)]\mathscr{D}[\Psi_{\alpha}(t)]$ is the Feynmann path functional measure and the action S has the form

$$S[\Psi^*_{\alpha},\Psi_{\alpha}] = \int_{t_i}^{t_f} dt \sum_{\alpha}[\, i\hbar\, \Psi^*_{\alpha}(t)\partial_t\Psi_{\alpha}(t) - H_{Tot}(\Psi^*_{\alpha}(t),\Psi_{\alpha}(t))] \tag{1.114}$$

In our two level model $\alpha = 1,2$ and corresponds to the upper and lower polariton states, we can write the vector forms $\Psi = (\Psi_{UP},\Psi_{LP})^T = (\Psi_1,\Psi_2)^T$ and $\Psi^{\dagger} = (\Psi^*_{UP},\Psi^*_{LP}) = (\Psi^*_1,\Psi^*_2)$ remembering that -in absence of spin orbit coupling terms- the upper and lower polariton fields are $\mathbb{C}$-valued scalar kind. In case of spin dependent terms the definition of $\Psi,\Psi^{\dagger}$ has to be generalized in terms of spinorial fields. In the exciton basis the total hamiltonian reads $H_{Tot} = H_{cav} + H_{exc} + H_{JC} + H_{XX} + H_{ext} + H_{pump}$ while for the exciton exciton interactions we already have a real space expression for the pump and free polariton term $H_{cav} + H_{exc} + H_{JC} = H_{pol}$ we have to find it, this can be easily done by recalling the Fourier conjugation between the k-space creation and destruction operators and the real space field operators, see (1.80). We restrict ourself to spinless system i.e. $H_{so} = 0$. The pump hamiltonian has a simple form in the polariton basis if one restricts to k-vectors close to zero and to a quasi resonant pumping (i.e. $\delta \ll \Omega_R$): under these assumptions the coupling η is real valued and constant $\eta^*(\mathbf{k}) = \eta(\mathbf{k}) \approx \eta_0$, and the pump hamiltonian reads

$$\begin{aligned} H_{pump} &= i\hbar \int d^2\mathbf{r}\; \eta_0[E(\mathbf{r},t)\Psi^{\dagger}_c(\mathbf{r},t) - E^*(\mathbf{r},t)\Psi_c(\mathbf{r},t)] \\ &= i\hbar \int d^2\mathbf{r}\; \eta_0[E(\mathbf{r},t)\Psi^{\dagger}_i(\mathbf{r},t)\tilde{\Theta}^{1,i} - E^*(\mathbf{r},t)\tilde{\Theta}_{1,i}\Psi^i(\mathbf{r},t)] \end{aligned} \tag{1.115}$$

where $E(\mathbf{r},t)$ is the incident radiation coherent field, $\tilde{\Theta}_{i,j}$ are the entries of the matrix $\tilde{\Theta}$ which diagonalizes the $H_0 = H_{exc} + H_{cav} + H_{JC}$ hamiltonian and represent the compact form of the

relations

$$\Psi_X = X_0\Psi_{LP} - C_0\Psi_{UP} \tag{1.116}$$
$$\Psi_C = C_0\Psi_{LP} + X_0\Psi_{UP} \tag{1.117}$$

where (X_0, C_0) are the Hopfield coefficients at $|\mathbf{k}| = 0$, notice that these relations are good as soon one is restricting the dynamics close to the bottom of the polariton bands. The exciton interaction term (**??**) can be written within the same approximations as

$$H_{XX} = \int d^2\mathbf{r}\, \Gamma^{XX}_{\rightrightarrows}[\Psi^\dagger\, \tilde{\Lambda}\, \Psi] \tag{1.118}$$

where

$$\tilde{\Lambda}(\mathbf{r},t) = \begin{pmatrix} C_0^4 n_{UP}(\mathbf{r},t) & 0 \\ 0 & X_0^4 n_{LP}(\mathbf{r},t) \end{pmatrix} \tag{1.119}$$

and $n_{LP,UP}$ are the number density operators for the upper and lower polariton band. The external potential can be put as well in the compact form

$$H_{ext} = \int d^2\mathbf{r}\, [\Psi^\dagger(\mathbf{r},t)\tilde{V}(\mathbf{r})\Psi(\mathbf{r},t)] \tag{1.120}$$

and $\tilde{V}$ is the matrix encoding the confinement acting on the upper and lower bands weighted by the hopfield coefficients

$$\tilde{V}(\mathbf{r}) = \begin{pmatrix} X_0^2 V_{cav}(\mathbf{r}) + C_0^2 V_{exc}(\mathbf{r}) & 0 \\ 0 & C_0^2 V_{cav}(\mathbf{r}) + X_0^2 V_{exc}(\mathbf{r}) \end{pmatrix} \tag{1.121}$$

To conclude we need to write the real space reperesentation of the free polariton hamiltonian (1.86), this can be done by finding the real space representation of the kernel (1.87). Close to zero in plane wavevector the parabolic band approximation can be applied also to the polariton dispersion and the real space kernel representation is the free particle one

$$\tilde{\Xi}(\mathbf{r}) = \begin{pmatrix} \hbar\omega_{UP}(0) - \frac{\hbar^2\nabla^2}{2m^*_{UP}} & 0 \\ 0 & \hbar\omega_{LP}(0) - \frac{\hbar^2\nabla^2}{2m^*_{LP}} \end{pmatrix} \tag{1.122}$$

and equation (1.86) has the real space representation

$$H_{pol} = H_{cav} + H_{exc} + H_{JC} = \int d^2\mathbf{r}\, [\Psi^\dagger(\mathbf{r})\tilde{\Xi}(\mathbf{r})\Psi(\mathbf{r})] \tag{1.123}$$

Summing up the terms (1.123)-(1.118)-(1.120)-(1.115) we finally have derived the action.

The physical meaning of equation (1.113) is that once the Hilbert space vector point Ψ_i is specified the probability of finding the state Ψ_f at the time t_f is proportional to the weighted sum of all the possible paths in the Hilbert space which connects the two. The second quastion is how to identify the dominant terms in this sum: for every possible path from the phase space point Ψ_i to the point Ψ_f the action $S[\Psi^*(t),\Psi(t)]$ takes a well defined $\mathbb{R}$ value if the Hamiltonian is hermitian. This is not our case because of the H_{pump} term but we will briefly see how to solve this problem, lets first assume to work with an hermitian hamiltonian. Since the action in the path integral formulation of the time evolution is multiplied by the imaginary unit, larger action terms correspond to faster phase oscillations which average to zero faster and faster as the action gets larger and larger. This pictorical representation of the time evolution suggests that the dynamics is dominated by the "trajectories" which have the smaller action: this is the so called Least Action Principle inherited from classical mechanics.

Mean field approximation[3] consists in finding the extremal value of the action (which is always a minimum for convex hamiltonians) and negleting all the other contributions. This corresponds in assuming the expectation value of the quantum observables evolves accordingly to the classical equations of motion. Indeed the extremal value of the action $\delta S[\Psi^*(t),\Psi(t)]$ is found only for the "classical" trajectories $\langle\Psi(t)\rangle$ satisfying the Euler-Lagrange equations of motion.

The non hermitian pump term seems to be a problem, indeed the larger the terms the quicker the time evolution operator diverges or decays. However the hamiltonian corresponding to the pump term (1.115) is linear in the polariton fields $\Psi(t)$ and $\Psi^\dagger(t)$, thus when we Taylor expand the action around the classical polariton field, the only non vanishing term is the first. This allows, for our purposes, a safe inclusion of the non hermitian pump term in the action.

The mean field equation of motions for the polariton field $\Psi(t)$ are easily derived if we take the variation of $S[\Psi^*(t),\Psi(t)]$ respect to $\Psi^\dagger$ and we set the result equal to zero. In the compact form we derived for the total action the computation is straightforward and for the lower polariton component reads

$$i\hbar\partial_t\Psi_{LP}(\mathbf{r},t)=\left[\hbar\omega^0_{LP}-\frac{\hbar^2\nabla^2}{2m^*_{LP}}+V_{LP}(\mathbf{r})+g_{LP}|\Psi_{LP}(\mathbf{r},t)|^2\right]\Psi_{LP}(\mathbf{r},t)+i\eta_{LP}E^{inc}(\mathbf{r},t) \quad (1.124)$$

Where $V_{LP}(\mathbf{r})=C_0^2V_{cav}(\mathbf{r})+X_0^2V_{exc}(\mathbf{r})$ is the confinement potential term, $g_{LP}=\Gamma^{XX}_{\rightrightarrows}X_0^4$ is the strenght of the Kerr (χ^3-type) nonlinearity induced by polariton polariton contact interactions and $\eta_{LP}=\eta_0C_0$ is the coupling efficiency of an incident coherent field quasi-resonant with the lower polariton energy ground state $\hbar\omega^0_{LP}$ and is proportional to the front mirror trasmittance

[3] Also called saddle point approximation in Field Theory textbooks

at normal incidence η_0. The inclusion of the lossy terms $\mathscr{L}[\rho]$ is completely non trivial from the stand point of the derivation of the above equation from first principles and in self consisten way: the reason is the Path Integral formulation needs to be extended to model the coupling of a quantum system with the environment, for the details we refear to [47]. Nevertheless we can add a dissipative term to equation (1.124) in a euristic but consistent way taking advantage of the mapping between a calssical damped harmonic oscillator and a non hermitian hamiltonian we demonstrated in section 1.1. A non null imaginary component in the NHH complex eigenenergy spectrum turns in a finite eigenenergy linewidth, corresponding to an exponentially damped probability of finding the system in the initial state as the time passes. This can be mapped in the friction term of the classical CHOs model, the classical equations of motion for an omogeneus friction term are in the form

$$\frac{d\mathbf{v}}{dt} = -\gamma\,\mathbf{v} \tag{1.125}$$

But then as long as the mean field approximation holds the quantum observables must obey the classical Euler-Lagrange equations, in addition we mapped the friction term of the above equation in section 1.1 to a non hermitian hamiltonian contribution in the quantum picture, we therefore demonstated that we can recount for the system dissipation by adding a term $\propto -i\gamma_{LP}\Psi_{LP}$, thus obtainig

$$i\hbar\partial_t\Psi_{LP} = \left[\hbar\omega^0_{LP} - \frac{\hbar^2\nabla^2}{2m^*_{LP}} + V_{LP}\right]\Psi_{LP} + g_{LP}|\Psi_{LP}|^2\Psi_{LP} + i\eta_{LP}E^{inc} - i\frac{\gamma_{LP}}{2}\Psi_{LP} \tag{1.126}$$

where $\gamma_{LP} = C_0^2\gamma_{cav} + X_0^2\gamma_{exc}$ is the lower polarition homogeneus linewidth and the origin of factor two in the denominator of the lossy term can be traced back in the NHH mapping proposed in section 1.1.

The last issue we want to address is how to model the drive if the the pump laser detuning is larger than the rabi splitting. It can be demonstrated [8] that the equation form is left unaltered but the coupling efficiency η becomes a functional of the reservoir density $n_{res}(\mathbf{r})$. We call reservoir the "hot" unbound charge carriers created by a positive detuned pump: these electrons have too high momentum to form the exciton bound state, however they can relax to the bottom of the conduction band trough non radiative mechanisms mediated by photons or defects. The modeling of these processes is highly non trivial and has to be accounted trough a time dependent master equation, which is coupled trough $\eta[n_{res}]$ to equation . We refear for the details to [8] since we will not deal in detail trough this manuscript with the mechanisms involving the reservoir.

This equation is often called Driven Disspative Gross-Pitaevsky Equation and was firstly derived (without the imaginary terms in the right hand part) to describe the dynamics of a diluite bosonic condensate wavefunction with contact repulsive interactions. The fact that the polari-

ton dynamics at mean field level is described by this equation is exciting because DD-GPE has a huge nuber of solution families depending on the different coefficients ratios, some of them show for instance superfluidity, solitons, vortex formation, topological excitations and much more. Many of these phenomena were already present in the undriven lossles equation but the addition of external driving and losses opens the frontiers to the study of the rich out of equilibrium dynamics of an interacting Bose-Einstein gas, in regimes often unreachable to other systems. Equation will be fundamental for the modeling of the dynamics of two coupled polariton cavities, which is the main subject of this manuscript.

CHAPTER 2

Samples and Experimental setup

Before strarting the description of the samples and of the setup, i want to aknowledge the collaboration within the group i worked in and the Team of engineers, physicists and chemists working in the clean room of C2N-Marcoussis. Without their know-how and the continuous close contact work the realization of such high quality samples would not be possible. In particular i would like to thank A. Lemaître and E. Galopin for the sample growth, L. Le Gratiet for the etching mask deposition and imprinting and I. Sagnes for the etching, as all their collaborators.

We will first describe which are the main techniques employed in the sample growth and etching, then we will focus on the particular sample used for all the measurements in this manuscript characterizing its optical properties with by means of the transfert matrix method proposed in section 1.3.1. The second part of the chapter will focus on the description of the experimental setup and measurement techniques.

2.1 Sample description

Our sample is grown by Molecular beam epitaxy (MBE), a technique originally developed in the Bell labs by A. Y. Cho and collaborators [48], which is a unique tool to grow layer by layer a desired heterostructure. The main advantages respect to the other growth protocols is the extreme control and purity which can be achieved, this latter being only limited by the chemical purity of materials employed in the growth and by the level of vacuum in the reaction chamber. The basic idea of MBE is to create ultra high vacuum in a chamber where the substrate is hold on a support which can be freely rotated and heated. Ultra-pure elements in form of small ingots are lodged in Knudsen cell heaters where they can be sublimated, each cell has also a shutter. The cell temperature has to be controlled with high precision since every temperature variation may affect the flux of sublimated molecules, and even small chemical overabundances can be source of defects in the crystal structure. Once a shutter is opened the gaseous element start to diffuse in the chamber and condense on the substrate wafer, if two or more shutters are opened the different elements reacts on the wafer to create the desired alloy. Another advantage of MBE is that the condensation and reaction of the atoms on the substrate is an intrinsically an out of equilibrium process, this allows the creation of alloys based on elements which are immiscible in the termodinamic equilibrium gaseous or liquid form. The term *Beam* means that evaporated atoms do not interact with each other or vacuum chamber gases until they reach the wafer, due to the long mean free paths. We schematize the MBE setup in figure 2.1 (a).The reaction chamber also lodges a high energy electron gun and a phosphorous sceen used to detect the diffracted electrons from the sample surface, this technique usually called with the acronym RHEED, allows to probe the growth of the sample layer by layer. In addition a lamp and a fiber allows the MBE operator to perform in situ fluorescence spectroscopy.

The working principle of the RHEED technique is quite simple: the electron partial waves generated by the scattering with an ordered structure can positively or destructively interfere, bright intensity maxima appear in correspondence of the directions satisfying the Laue-Bragg condition. If the electron gun flux is kept constant, the roghness characterizing non completely grown layers creates spurious constructive interferences at angles different from the Bragg ones resulting in a lowering of the Bragg-Laue peak intensity I. If this quantity is recorded over time one can track from the number of oscillations of $I(t)$ the number of layers already grown, allowing one to control the layer thickness on orders of some angstroms: since the $\lambda/4$ layers of the DBRs are approximatively $(600 \div 700)$Å thick this control is fundamental because every variation in the layer thicknesses may degrade the DBR reflectivity. A better control is even more important in the growth of the QW because as discussed in section 1.2.3, any thickness fluctuation greatly enhance the decoherence processes, enlarging the excitonic linewidth and worsening the exciton optical properties, see for instance [41]. The RHEED mechanism is sketched in figure 2.1 (b).

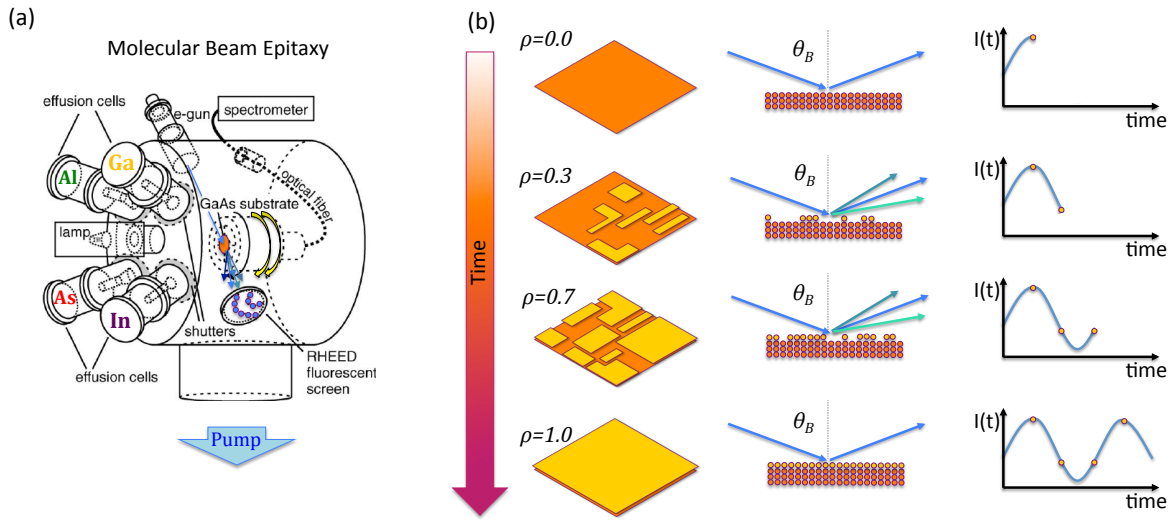

Figure 2.1: Typical setup used for the MBE growth technique (a). RHEED working principle (b), typical MBE growth rates are $\nu < 1\ nm/s$. We call ρ the fraction of atoms in the growing layer over the total atoms of one layer, θ_B is the Bragg angle.

The presence of the rotation stage on the substrate holder is of great importance indeed, if the wafer stands still because all Knudsen cell positions cannot be perpendicular to the holder plane the subimated atom flux have a spatial gradient proportional to the beam angle. This gradient vanishes as soon as the holder is kept rotating at constant velocity, but can be also employed to create a wedge in the layer thickness, this fact can be exploited to obtain a spatial dependent exciton-cavity detuning when growing the *GaAs* spacer.

Once the full heterostructure is grown on the substrate a polymeric layer is deposited on the top mirror. The mask can be imprinted by combined use of electron beam litography creating the negative and a UV lamp which hardens the positive of the desired pattern. The negative can be lifted by after a bath in a solvent. The sample is washed in a diluite acid to remove the oxides which can spoil the chemical etching process. The dry etching procedure is rather complicate but is exentially based on a Inductively Coupled Plasma (ICP) technique, where the active etchant is a clorine-based gas. The sample is lodged in a high vacuum chamber where the gas is ionized to plasma thanks to a strong radiofrequency electromagnetic field on the metal platter located just below the saple holder. Two plates of opposite charge creates a strong electic field perpendicular to the saple, the ionized electrons have higher kinetic energy and start to be absorbed by the surface, creating very low damage since they are light paricles, however the negative surface charge grows and the ions in the plasma start to get accelerated to the surface where they etch the unprotected surfaces both by sputtering mechanisms and by chemical re-

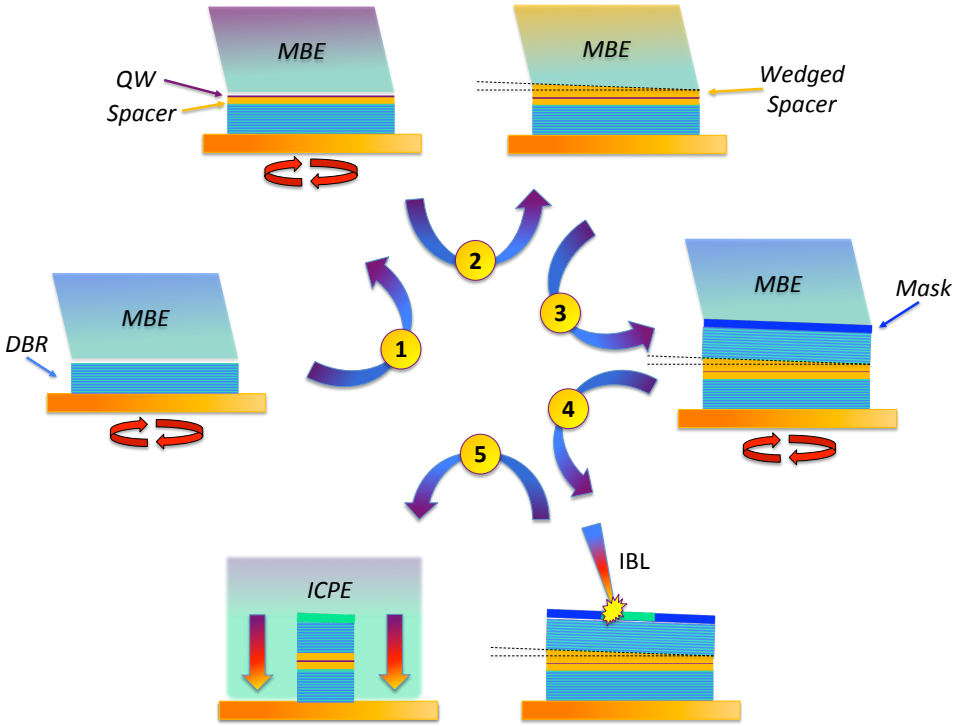

Figure 2.2: Growth and etching procedure of the sample. First the *AlGaAs*-based bottom DBR is epitaxially grown on the substrate, the arrows indicate that the sample is kept in rotation to obtain constant layer thickness on the wafer plane. In a second step the bottom part of the *GaAs* $\lambda/2$ spacer is grown followed by the *InGaAs* QW. The third step is to stop the rotation and grow the top part of the spacer with a thickness spatial gradient. Then the top DBR is grown and the polymeric mask is deposited, an ion beam hardens part of the mask corresponding to the pattern which is etched by the ICP.

action. To increase the aspect ratio of the etching process, periodic deposition of passivation layers can be employed, following a so called *Bosch* step. The technique developed in our lab by I. Sagnes and collaborators allows to fabricate structures with a section as small as $1\mu m^2$ with a height of 10 μm and almost vertical walls, this technique does not impose any restriction on the shape of the structures, except that their lateral dimension should not be too small (typically lateral dimension should be larger than 1.0 μm) to avoid non-radiative recombinations on the side walls of the etched structures, which would strongly degrade the optical properties of the system. 0D, 1D and patterned 2D structures can be realized with a high degree of freedom in choosing the desired geometry. We schematize the whole fabrication procedure in figure 2.2.

Polaritons get confined in these structures thanks to their photonic component which is vertically confined by the cavity and laterally confined by the large refractive index mismatch between vacuum and the semiconductor heterostructure. The excitonic component is instead free to move in the QW plane since the exciton Bohr radius is much smaller than the typical

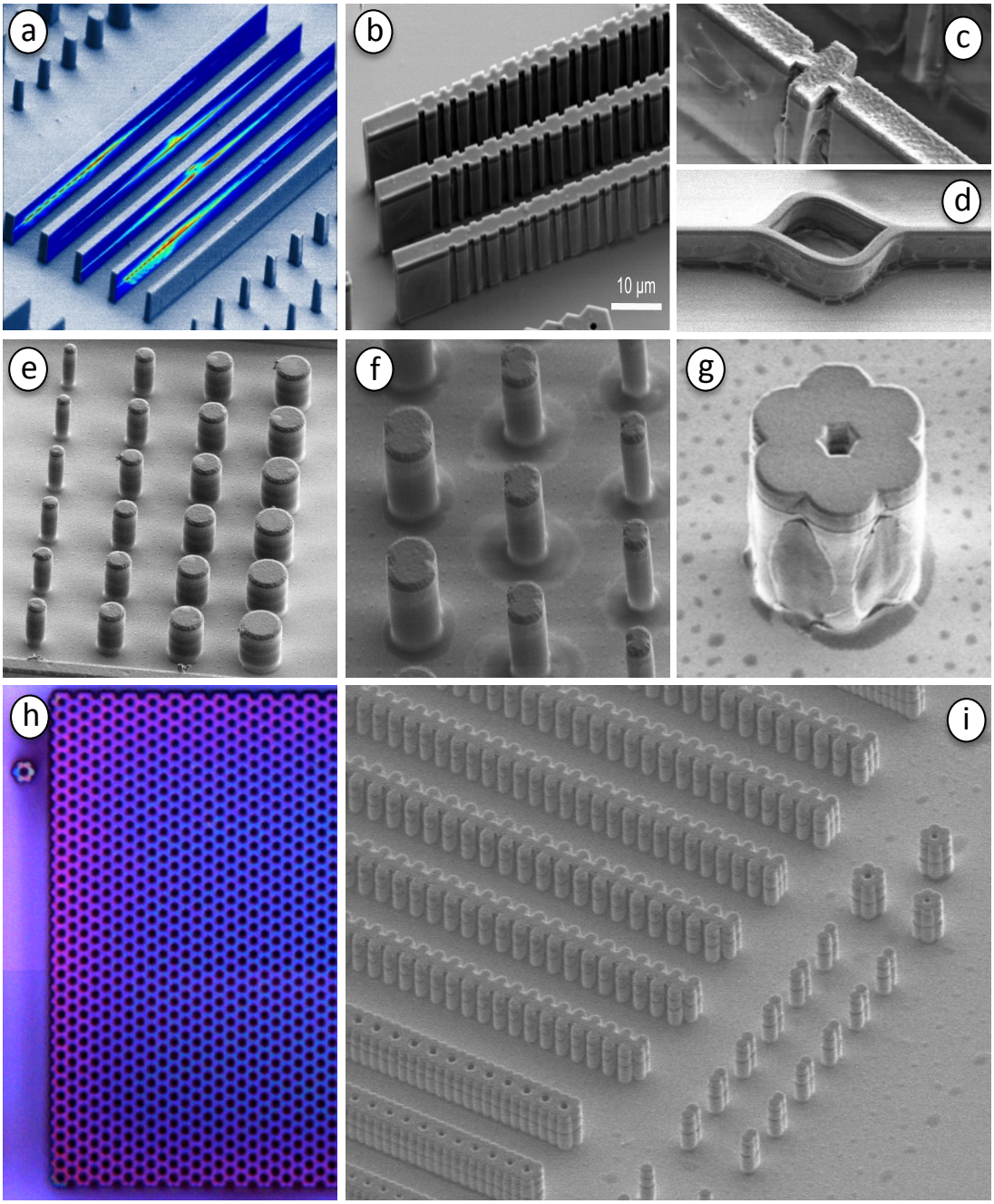

Figure 2.3: (a)-1D wires, the color map on the side is the spatially resolved PL of the polariton condensate flowing in the structure, from [49]. (b)-1D quasicrystal obtained by lateral patterning a wire, this induces a spatially dependent modulation of the lateral potential. (c)-Diode juction, (d)-Mach-Zender interferometer. (e)-Micropillar structures which can be regarded as simple artificial atoms thanks to the polariton level discretization, the diameters range between 6 and 1.5 μm. The diameter tuning can be used to engineer the energy level structure. (f)-(g) the overlap of two or more pillars results in a coupling term, the resulting structures mymic real molecules in solid state, here we show respectively an analogue H^2 and benzene molecule. (h)-Honeycomb lattice structure mymicking graphene. (i)-Some intersting 1D lattices which are very diffucult to reproduce with trapped cold atoms, ions or superconducting circuits.

later size of the structures built with this technique. The etching is therefore equivalent to an engineering of the external potential acting on polaritons. The engineering the dimensionality of the structure allows to study 1D propagation of polariton condensates, the fabrication of Mach-Zender interferometers for coherent polaritons flows and to build syntetic atoms and crystals by 3D-confining polaritons in micropillar structures. Some representative structures which can be built with this technique are shown in figure 2.3. The strenght of polariton systems is their hybrid nature: where the excitonic component provides a local Kerr nonlinearity the photonic component provides both the confinement but expecially straighforward, non disturbing and clean probe to the system. For instance a polariton condensate flowing in a wire can be direcly resolved by mean of its PL, and the valence orbital structure of an artificial molecule (i.e. fig. 2.3 (f)-(g)) can be also resolved by means of a simple imaging technique. The huge experimental advantage of detecting NIR photons becomes critical when one is interested in studying the time resolved dynamics of coupled lattices of resonators with a Kerr nonlinearity (fig. 2.3 (h)-(i)).

Our sample consists of of a $\lambda/2$ *GaAs* spacer ebedding at his center a 80 Å wide *InGaAs* quantum well, the spacer is included between two *AlGaAs* based DBRs and all the structure was grown by molecular beam epitaxy (MBE) on top of a high purity GaAs crystal. The DBR layers are $Al_{0.1}Ga_{0.9}As$ and $Al_{0.95}Ga_{0.05}$ alloy doublets forming the 26 and 30 pairs which constitutes the top and bottom mirrors. The Indium-Gallium-Arsenide quantum well composition was chosen so that the exciton energy lays roughly $\sim 35\ meV$ below the $4K$ *GaAs* Γ-point gap $E_\Gamma = 1.519\ eV$, since also the substrate is monocrystalline GaAs this allows to collect the emission of the system both in reflection and transmission geometry. This is an enormous advantage when pumping at high power the system because one avoids all the back reflected light from the top mirror, allowing much more precise and clean measurements.

We simulated the reflectivity of our sample by means of the Transfer Matrix Method illustrated in section 1.3.1. We chosed a resonant cavity mode corresponding to the vacuum wavelenghth $\lambda_0 = 840.0\ nm$, the optical thickness of the two DBR layers are 579 Å and 697 Å respectively for the lower and higher Aluminium fraction in the *AlGaAs* alloy. The aproximative *GaAs* substrate depth is $0.7\ mm$. We plot the resulting simulation in figure 2.4. From the simulation we find the following parameters

$$\tilde{\lambda}_0 = 840.002\ nm \qquad \gamma_{cav} = 4.9\ \mu eV$$

the small difference between $\tilde{\lambda}_0$ and the spacer λ_0 is amenable to the smooth spatial dependence of the refractive index in the wavelength as pointed by the Sellmeier's equation (1.62). The cavity linewidth correspond to a photon lifetime of 133 *ps* this value of course is overextimated beacuse we are assuming perfectly smooth interfaces, but the order of magnitude is correct.

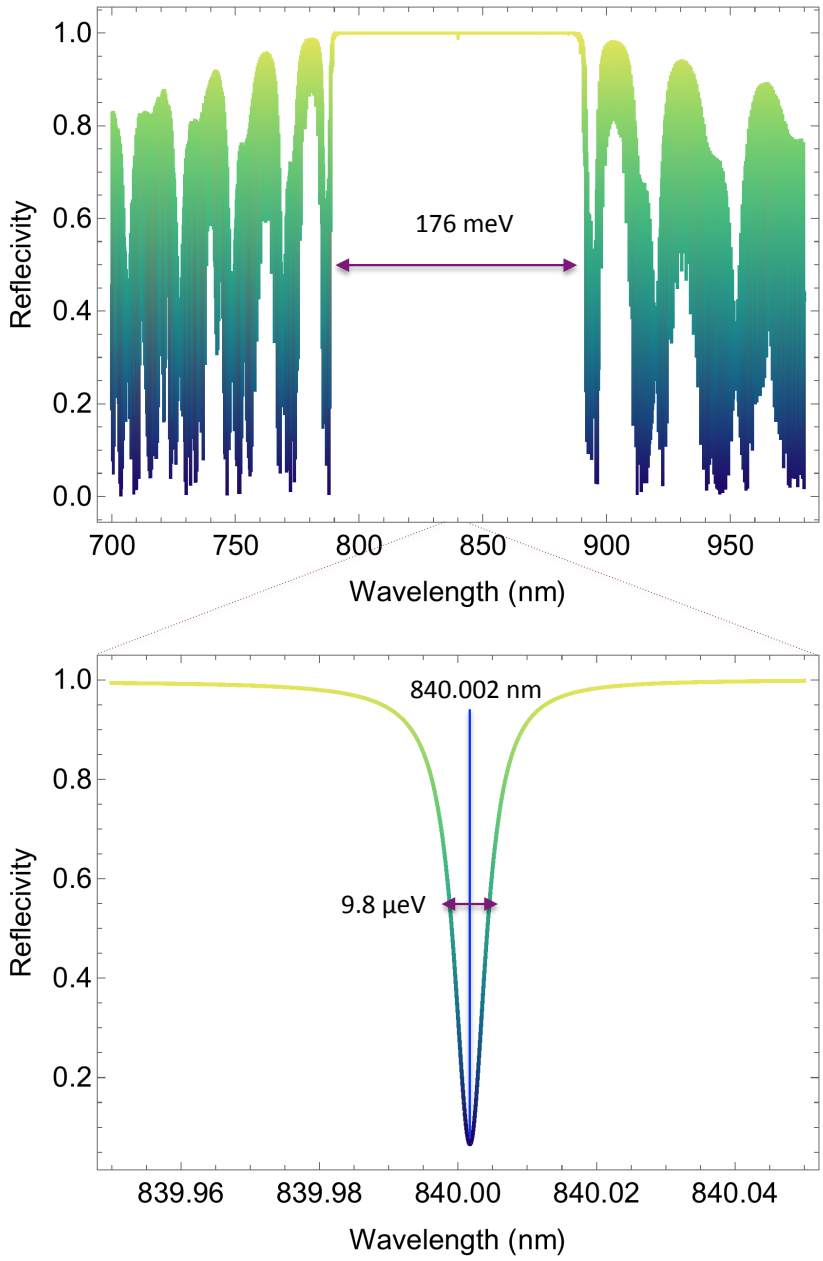

Figure 2.4: (top)-MTM calculation of the sample reflectivity spectrum. The stop band is roughly $176meV$ wide centered on the cavity resonant energy $E_{cav} \approx 1476\ meV$. The fast oscillations in the reflectivity outside the stop band are due to the weak Fabry-Perot cavity resonances of the substrate which has a refractive index a little higher than the DBRs and much higher than the air. Since the optical thickness of the substrate is huge compared to the heterostructure, these beats correspond to very high cavity modes which correspond to weaker resonances. (bottom)-Zoom around the cavity resonance, the peak transmittivity is $T(\lambda_0 + \delta\lambda) \approx 0.93$ where $\delta\lambda \approx 0.002\ nm$ is a small frequency shift of the resonance provided the refractive index of the DBR layers and of the spacer smootly changes with the wavelength. We can extract the cavity linewidth, and we find $2\gamma_{cav} = 9.8\mu eV$, corresponding to a radiative lifetime of 133 ps.

2.2 Setup and Measurement techniques

As we pointed in the previous sections the polariton observables are completely encoded in the cavity spontaneous emission. Our objective was to be able to image the cavity emission both in real and momentum space, both spatially and energy resolved. The setup can also be upgraded to include a streak camera allowing time resolved measurements on timescales of a few picoseconds, in this manuscript however we only performed CW experiments so we will omit this part of the setup. We show the setup schematics in figure 2.5.

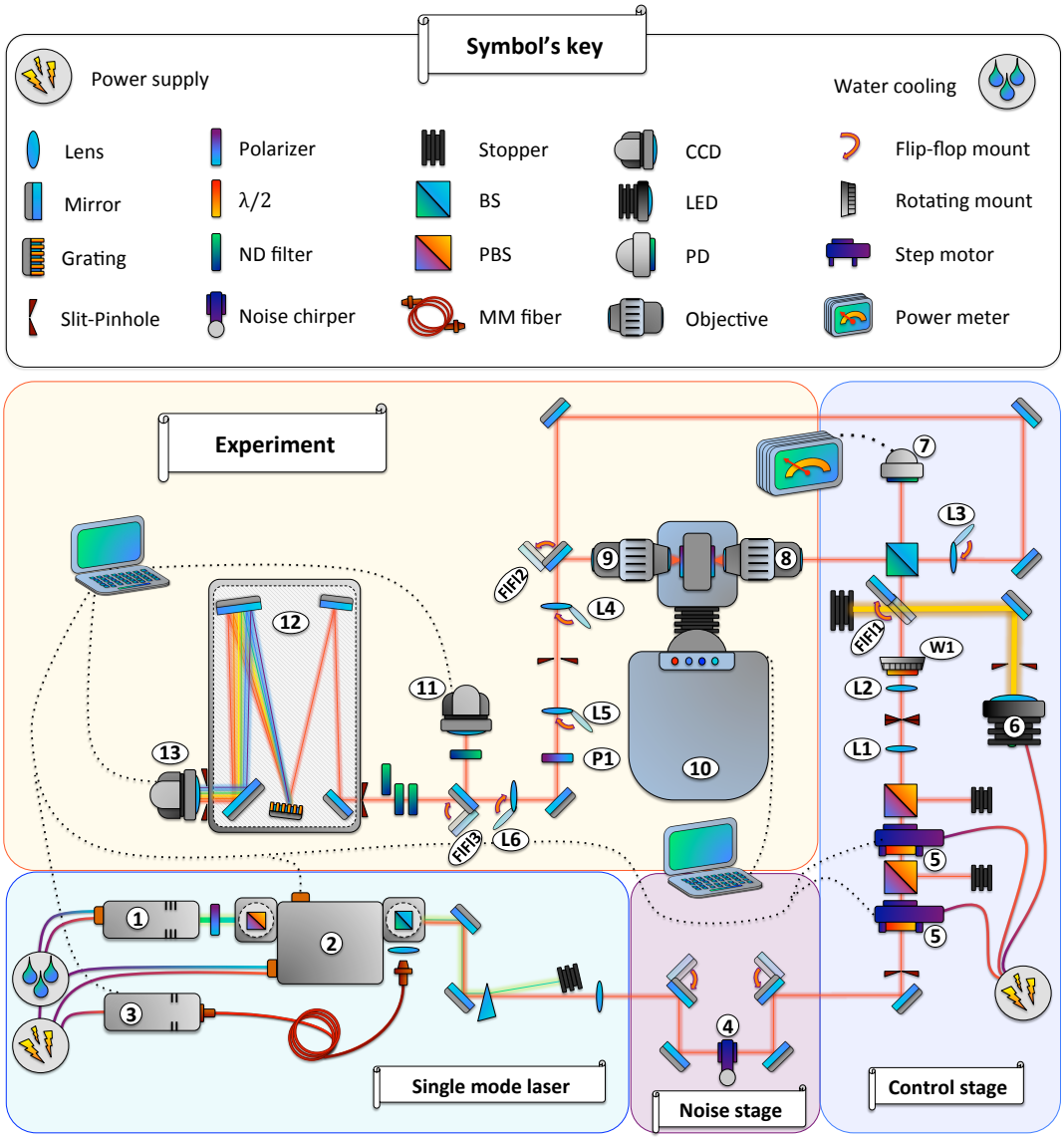

Figure 2.5: Setup schematics. Notice the seven flip flop mounts which allow to swhich between different detection configurations without changing the allignment. This flexibility plays an important role to ease the measurements since constant allignement on the micrometric structures and different imaging techniques had to be frequently alternated.

The **SINGLE MODE LASER STAGE**, highlighted in blue comprehend a Millennia XS stabilized $Nd:YVO_4$ laser (1), delivering $10W$ at $532nm$. The laser beam polarization is rotated in vertical direction respect to the table plane by a $\lambda/2$ waveplate. The Millennia XS beam pumps a MSquared SolsTiS single mode Ti:Sapphire cavity (2) which can be tuned in the wavelength range $(640-1100)\,nm$ with a precision of $0.1\,pm$, the nominal linewidth is $< 50\,kHz$, meaning the linewidth is $\sim 10^4$ times smaller than the minimal wavelength tuning step. In the imput port of the cavity a high quality PBS cleans the spurious polarization components of the Millennia beam while in the output port a small part of the output TEM_{00} beam is focused on a multimode fiber leading to a Ångstrom WS-6 high finesse wavelenght meter (3). The Wavemeter and the cavity are connected to the feedback control MSquared IceCube block which reads down the WS-6 and actively compensates the cavity to stabilize the output wavelength. Part of the $532\,nm$ pump beam is not down-converted by the single mode cavity active medium and constitute a spurious secondary output beam. Since a typical intensity ratio between the main and secondary beam is $\zeta = I_p/I_s = 400$ a simple prism or a high pass filter is enough to get rid of this contribution. The tipical beam divergence after the SolsTiS cavity is quite large and must be compensated with a lens which focal spot lays on the exit mirror of the cavity.

In the **NOISE REDUCTION STAGE**, highlighted in purple, two flip-flop mirrors allow to divert the beam on demand and let it pass trough a Thorlabs LCC3112H LCD noise eater (4). The stabilization of the beam power relies on a simple feedback circuit based on a low bias current OpAmp which imput voltage is provided by a integrated photodiode, where a small part of the incident light is collected, a potentiometer fixes a reference bias voltage acting as the OpAmp ground, the unbalance between the reference voltage and the imput pin is converted in a proportional signal which drives the LCD amplitude modulator. A typical noise reduction factor is 150 between $6\,Hz$ and $200\,Hz$. The principal noise source in the line is due to the Millenia and to the dust particles since the total optical path is about $4m$. Tipical power fluctuation rms in the DC to few Hz range is better than 0.3%, with a nearly optimal alligning.

The **CONTROL STAGE** is responsible for the polarization and power management. Two half wavelenghth waveplate-PBS couples allow to change the beam power over six orders of magnitude, from $0.5\,W$ to $0.5\,\mu W$. To achieve a fine power tuning the $\lambda/2$ plates are lodged on Thorlabs PRM1Z8 DC servo motors (5) which have a 0.03^o angular step accuracy, the two servo motors are controlled by remote. Because of the number of optical elements and dust the mode profile of the beam may degrade, two lenses (L1-L2) form a telescope. If a pinhole is located at the focal plane of the telescope the spourious Fourier modes of the beam can be filtered out, moreover the telescope allows to fine tune the beam collimation. The $\lambda/2$ plate W1 can be used to set the beam polarization axis. A Thorlabs M660L4-C4 collimated red LED (6) along with the flip-flop mirror FlFl1 can be diverted along the beam line allowing to image in the visible spectrum the sample surface, this is fundamental for the beam aligning procedure, as

we will briefly see. The beam get divided by a 70 : 30 non polarizing BS, the transmitted beam impinge on a Thorlabs S145C photodiode (7) which allows to measure the laser power. Finally the flip-flop lens L3 allows to image the Fourier plane of the excitation objective (8), as we will explain in the measurement description this allows the k-space imaging of the sample emission in reflection geometry.

The **EXPERIMENT** comprehends a Montana C2 closed cycle cryostation (10), where the sample is lodged, which cools down the sample to $4K$. The sample holder can be moved on the xz plane by a ANPz101eXT12 Attocube piezo stage. Two high working distance-high numerical aperture objectives (8) and (9) are respectively used to focus the pump beam and to collect the transmitted luminescence. The excitation objective (8) fixes the optical axis and was mounted on a three stage positioning system with xy $1.4\mu m/deg$ positioners and a $0.35\mu m/deg$ precision along the optical axis z. The collection objective (9) was mounted on a three stage xyz actuator with double screw pitch precision and on a two axis mount to adjust the tilt of the objective axis respect to the optical axis fixed by objective (8). The flip-flop mirror (FlFl2) allows to divert on the line the reflected or transmitted emission of the sample. The flip-flop lens L4 images the Fourier plane of objective (9), while the lens (L5) and (L6) are used to image with different magnifications the beam on the detectors. The polarizer (P1) allows to do polarization resolved measurements. The Grasshopper 1394b CCD detector (11) along with the flip-flop mirror (FlFl3) was mainly used in the allignment procedures, while an Andor CCD camera (13) was used for the measurements. The Andor CMOS detector is cooled to -40^oC by peltier cells and is able to capture 1024×1024 pixel images up to 100 fps with a pixel register of 14 bit. The Andor CCD is coupled to a Princeton Instruments SP2500A single grating spectrometer (12) which allows to do energy resoved measurements with a resolution of 30 μeV. To image the real space the spectrometer slit is opened and the grating is set to the 0-order, so it behaves as a mirror. We table the imaging element characteristics:

Code	Object	Industry	Specifications
L1	N-BK7 Lens	ThorLabs	Coated, 2”$\varnothing$, $f = 150mm$
L2	N-BK7 Lens	ThorLabs	Coated, 2”$\varnothing$, $f = 150mm$
L3	N-BK7 Lens	ThorLabs	Coated, 2”$\varnothing$, $f = 300mm$
L4	N-BK7 Lens	ThorLabs	Coated, 2”$\varnothing$, $f = 300mm$
L5	N-BK7 Lens	ThorLabs	Coated, 2”$\varnothing$, $f = 750mm$
L6	N-BK7 Lens	ThorLabs	Coated, 2”$\varnothing$, $f = 300mm$
8	Plan Apo. Obj.	Mitutoyo	Coated, $NA = 0.55$, $WD = 200\ mm$
9	Plan Apo. Obj.	Nikon	Coated, $NA = 0.55$, $WD = 220\ mm$

Let’s see the alignment procedure on the sample and the fundamental measurement protocols. We will use the term *flip* when a flip-flop mount element is put in the beam line and *flop* other-

wise.

- **ALIGNMENT**: we start (FlFl1) flop, the laser light shines on the sample. (L3)-(L4)-(L5)-(FlFl2) are flop, (L6)-(FlFl3) are flip, the reflection of the laser spot is imaged on the CCD (11). We set the laser spot on focus and we mark the laser spot position on the screen. Next we flip (FlFl1), now the LED light images the sample surface on the CCD. By using the piezo actuators one can move the sample until the marked spot on the screen corresponds to the microstructure one desires to pump. Finally (FlFl1) is flop and the objective (8) focus is adjusted since the substrate height is different from the top mirror one.

- **PHOTOLUMINESCENCE**: the sample is pumped non resonantly around one of the reflectivity minima of figure 2.4 around 770 *nm* in order to achieve optimal coupling with the QW optical transitions. Many electron are promoted to the conduction band and can relax non radiatively to populate all the allowed exciton-polariton states. The sample emission can be imaged both in reflection or transmission geometry depending on (FlFl2) is respectively flop or flip. If (L3)-(L4)-(FlFl3) are flop we can image the photoluminescence (PL) via the lens (L5) or (L6) on the CCD (13). Once the vertical slit is closed and the grating is tilted, the vertical axis on the CCD is real space and the horizontal axis resolves the y-slice of real space in energy. If now (L3) or (L4) are flip (depending on the collection geometry) the emission is imaged in k-space, and the CCD horizontal axis measures the momentum of the PL. The energy-momentum resolved PL provides a clean measurement of the polariton dispersion $\omega_{LP,UP}(k)$. In order to neglect nonlinear effects and the reservoir perturbation the pump has to be weak $P_{pump} \lesssim 10\mu W$.

- **RESONANT TRANSMISSION**: the sample is pumped close to level resonance, and usually the collection is in transmission geometry to avoid the spurious signal from the top mirror: (FlFl2)-(FlFl3)-(L4) are flop, we usually flop (L6) and flip (L5) which allows a higher magnification. The system emission is directly imaged on the Andor CCD and can be eventually resolved in energy by means of the spectrometer (12). By scanning the laser frequency at low power one can probe the level structure of a photonic molecule as in fig 2.3-(e)-(f)-(g) by integrating over the spatial coordinates the emission and the molecules orbitals can be direcly imaged when pumping resonantly on of the energy levels. By increasing the power one can also study the nonlinear response of these structures, in particular the possibility to probe the transmission of the sample is critical to this aim, since the reflected light from the top mirror can eventually be much more intense than the system emission.

CHAPTER 3

Planar cavities and Micropillar structures

In the perspective of building complex lattices or networks of coupled microcavities the first natural question to address is the study and characterization of a planar microcavity, indeed many of the micropillar properties in the linear regime can be inferred direcly from the dispersion relation $\hbar\omega_{pol}(\mathbf{k})$ of a nearby planar cavity. As we demonstrated in section 1.4 the detuning of the cavity mode from the exciton line and the rabi splitting completely determines the Hopfield coefficients (1.94)-(1.93). These coefficients are the key quantities to determine the polariton-polariton interactions (see (1.111)). An accurate characterization of 2D-cavities is the starting point for all the measurements we will show hereafter. From the planar cavity frame we will then characterize some single micropillar structure, hereby studing how the pillar size affects the ground state energy detuning from the 2D cavity one and thus the excitonic fraction of the confined polaritons. Finally we study the dependence of the effective polariton Kerr coefficient with the sample temperature: this additional fine control over the nonlinearity is very intersting and paves the way to study phenomena as the unconventional photon blockade in photonic molecules [26]-[27], which depend dramatically on the absolute value of the interaction constant.

3.1 Planar Cavities

The sample used in the following experiments is a small part of a initial circular GaAs wafer on which a planar Fabry-Pérot cavity constituted by two distributed bragg reflectors embedding an InGaAs quantum well was grown (see section 2.1). The cavity spacer presents a wedge which allows to change the bare exciton-cavity photon detuning along the wafer. A small rectangle approximatively 2 cm wide and 0.6 cm high was cleaved from the wafer. A repeated pattern comprising many different structures was then etched from the planar cavity. By repeating the pattern along the rectangle one is able to work on the same nominal structures in different detuning regions. We show in the below figure a schematic of the etched motifs.

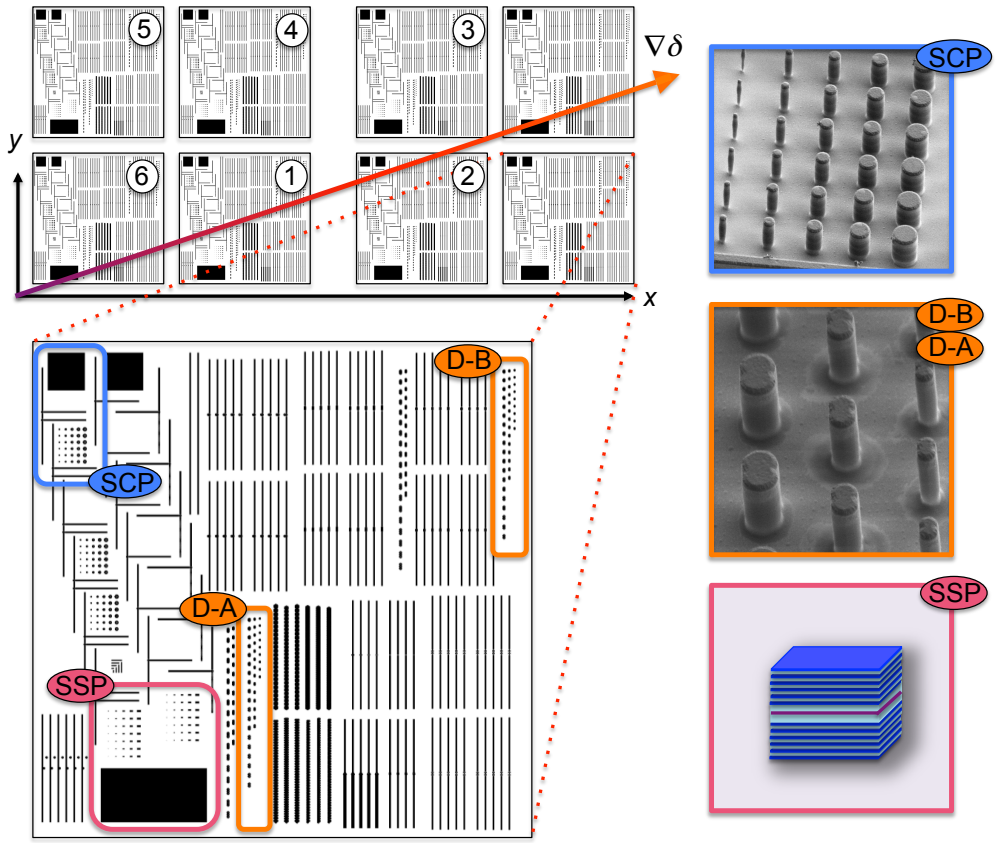

Figure 3.1: (Top left)-on the cleaved rectangular part of the wafer eight groups of four patterns were etched. Only the six central patterns were in the detuning region of interest. The arrow shows the direction of detuning gradient $\nabla\delta$. (Bottom left)-zoom of the repeated pattern, the side is about $950\mu m$. The mask includes many different structures, among them planar cavities, wires, laterally patterned wires, diodes, routers, single pillars, molecules and microstructres gating different wires. We highlight in different colors the portions of the motif containing the relevant structures to our experiments. (SCP) includes a 100×100 μm squared 2D cavity and single micropillars with different diameters. (D-A) and (D-B) includes dimer molecules with different diameter and center to center distance. (SSP) includes a 200×100 μm planar cavity and rectangular single pillars with variable width and 2:1 aspect ratio.

In figure 3.1 we show a small portion of the retangular sample: on the right of the eight motifs the exciton-cavity detuning is $\delta \gg 0$ and $\delta \ll 0$ on the left, thus the corresponding lower polariton has $X^2(0) \approx 1$ and $X^2 \approx 0$. These two oppoiste situation are not very attractive since if the lower polariton is almost an exciton the optical quality of the emission is worsened due to a weak overlap with the free space modes (which is mediated by the cavity photon field) and the eigenmodes are broad since the exciton linewidth $\gamma_{exc} \gg \gamma_{cav}$ and $\gamma_{LP} = C^2\gamma_{cav} + X^2\gamma_{exc}$. On the other hand the highly photonic polaritons are very good candidates to address the linear properties of the microstructures due to enhanced emission and narrow linewidths but they are of any interest when trying to address the nonlinear properties of the system. The motif numbering (1-6) and the three highlighted regions labels reported in figure 3.1 will be used hereafter very often to help the reader in the orientation on the sample.

The characterization of the planar cavity polariton is the first step for the ongoing studies. The measurements of the polariton dispersion provides trough equation (1.90)-(1.89) valuable information on the bare exciton and bare cavity photon dispersion and on the Rabi splitting. Once these three quantities are known, the polariton properties are completely characterized by the Hopfield coefficients (1.94)-(1.93).

Since we need to perform energy resolved measurements the spectrometer was previously calibrated by shining the laser trough the substrate and imaging the transmitted light on the spectrometer slit (element (12) - figure 2.5). The laser wavelength can be tuned within $0.1\pm$ and has a 50 kHz linewidth which is unresolvable by the adopted 1200 g/mm grating, indeed the spectrometer resolution limiting factor was the 10 μm slit minimal width, we can therefore assume the wavelenght of the laser as an errorless quantity. In figure 3.2-(a) we measured the signal centroid on the CCD at 1 nm steps, the error on the centroid position is roughly 0.02 pixels. The data can be fitted with a simple linear regression $y = mx + q$, the fit is weighted on the pixel centroid error and provides

$$m = (59.20 \pm 0.04)\ pix/nm \quad q = -(49125 \pm 33) pix$$

The centroid energy has then the simple form

$$E(pix) = \frac{hcm}{(pix - q)} \tag{3.1}$$

where h is the Planck constant and c the speed of light. The error associated to this calibration can be extracted from the covariance matrix of the fit $Cov(\sigma_m, \sigma_q)$ since the errors on m and q are completely correlated as

$$\sigma_E^2(pix) = (\nabla_{(m,q)} E(pix))^T Cov(\sigma_m, \sigma_q)(\nabla_{(m,q)} E(pix)) \tag{3.2}$$

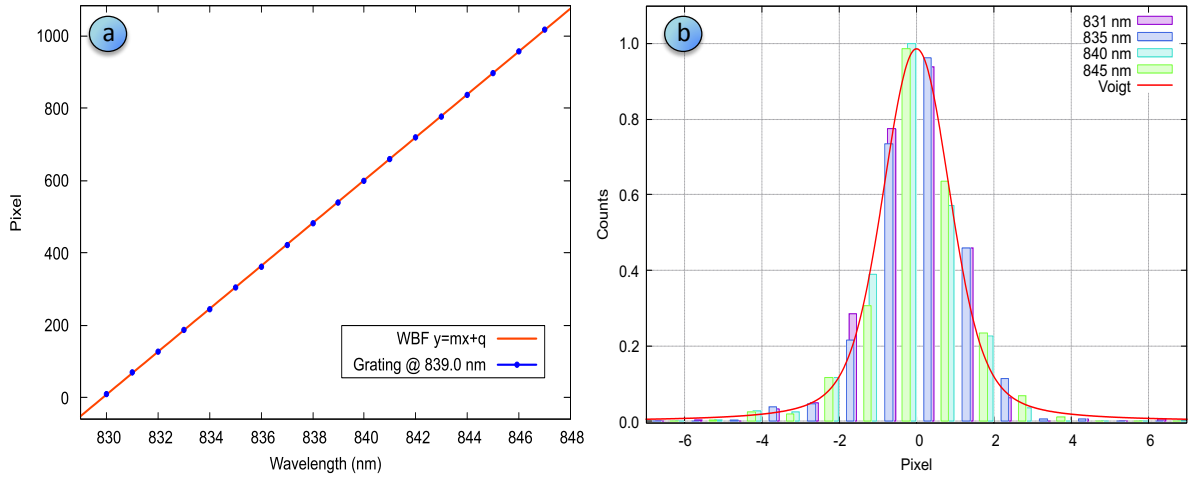

Figure 3.2: Spectrometer calibration (a). Spectrometer point-spread function (b), the experimental data are fitted with a Voigt profile, since the model is nonlinear a maximum Likelihood Markov Chain Monte Carlo (MCMC) approach was adopted.

the calculation is straightforward and one finds that the relative error is almost constant in the whole pixel range $\sigma_E/E \approx 0.0013$. Another important information we can extract is the spectrometer resolution. To address this quantity we projected along the slit direction (i.e. the real space axis) the CCD image, this provides a one dimesional histogram for every wavelength. We superimposed some of these histograms by subtracting the centroid postion and the result is shown in figure 3.2-(b), the FWHM of the peak is the key information to extract the spectrometer resolution. The lineshape of the peak is the convolution of many effects i.e the slit aperture, the grating instrinsic resolution and surface defects, dust and charge diffusion on the CCD. In general some of these effects cause a homogeneous broadening of the line, some other an inhomogeneus one, so the lineshape can be described by a Voigt profile, which results from the convolution of a Gaussian and a Lorentzian distribution. One of the possible Voigt profile representations is

$$V(x,\gamma,\kappa) = \kappa \int \frac{e^{y^2}}{(x-y)^2+a^2}\, dy \tag{3.3}$$

the fit result is shown in figure 3.2-(b) and provides

$$\gamma = (0.35 \pm 0.02)\ pix \quad \kappa = (1.41 \pm 0.05)$$

and the FWHM of the Voigt profile can be calculated as

$$2\gamma_V = 2\alpha_1\gamma + 2\sqrt{\alpha_2\gamma^2+\sigma^2} = (2.07 \pm 0.11)\ pix \tag{3.4}$$

where $\alpha_{1,2}$ are constants which can be easily found in literature and $\sigma = \sqrt{\log(2)}$ and the spectrometer resolution at the central wavelength $\lambda_0 = 839\ nm$ is $R \approx 24000$.

To measure the polariton dispersion we adopted the strategy firstly proposed by Weisbuch and collaborators [7], which relies on the conservation of the in plane momentum between the emitted photon and the cavity polariton due to the optical energy-momentum selection rules imposed by the planar geometry (see section 1.2.3). We imaged the energy and momentum resolved emission of the rectangular cavities in SSP-(1) to SSP-(6). These cavities are not perfect planar cavities due to the finite lateral dimensions however the polariton de Broglie wavelenghth is much smaller than the $200 \times 100\ \mu m$ sides of the cavity and then their dynamics can be regarded in good aproximation as free in the in plane direction. We pump the cavity at its geometrical center nonresonantly, close to one of the reflectivity minima showed in figure 2.4. The pump power is set low enough to neglect all the polariton-polariton interaction terms adopting the setup configuration illustrated in section 2.2-(PHOTOLUMINESCENCE) in reflection geometry. We show the measured polariton dispersion for the cavity SSP-(4) in figure 3.3-(a).

Every CCD frame provides an intensity matrix $I(i,j)$, with $i,j = 1,...,1024$. The row pixel can be turned in a energy value trough equation (3.1). The column pixel can be calibrated using the definition of numerical aperture of the objective which is imaging the sample $NA = n\sin(\theta)$ where n is the refractive index of the medium in which the objective works and θ is the maximal half-angle of the cone of light that can enter or exit the objective. The tails of the dispersion must then be cut at an angle

$$\theta_{MAX} = \sin^{-1}\left(\frac{NA}{n_{air}}\right) \approx 33\ deg \tag{3.5}$$

since the objective (8) (see fig. 2.5) has a nominal $NA = 0.55$. If the left and right end tails are zoomed this maximal angle appears as a vertical line outside of which the intensity fades. The limit of this approach is that one has to trust the nominal value of the numerical aperture, we solved this problem by averaging the pixel calibration over dozens of different dispersions. A more accurate calibration can be done by combining a telescope constituted by two well known lens with equal focal and a slit. From the focal length and the slit aperture an accurate calibration can be done. However this procedure was not necessary to our purposes since a scale error on the calibration only affects the effective mass of the polariton which was not a relavant information for our purposes. We end with an intensity matrix $I(E(i),\theta(j))$ and recalling that $k_{\|} = |k|\sin(\theta)$ we found the dispersion relation for the upper and lower polariton branches.

The intensity map recorded by the CCD was then fitted. To this aim a strategy is to convert the map in a set of points and weights. The first step was to estimate the background $I_B(i,j)$ by covering the laser beam and recording the frame. Once the mean value $\langle I_B(i,j)\rangle$ and the standard deviation σ of the background were known, the mean was subtracted to the signal matrix $I(i,j)$ and all the matrix elements with $I(i,j) < \langle I_B(i,j)\rangle + 3\sigma$ were discarded from the

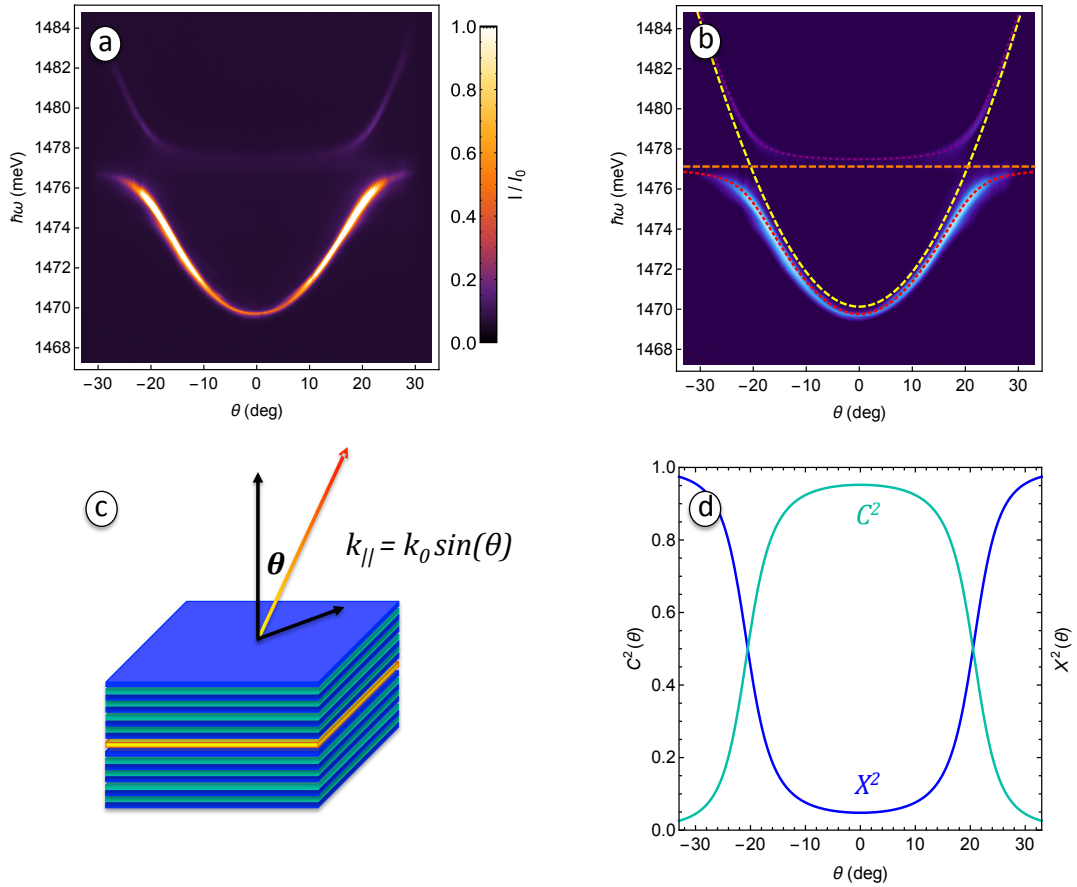

Figure 3.3: (a)-Measured polariton dispersion for the SSP-(4) rectangular planar cavity. (b)-Best fit of the lower and upper polariton branch modeled by equation (1.90)-(1.89) are respectively the red and purple dotted lines. The orange and yellow dashed lines are the bare exciton and bare cavity photon dispersions in parabolic band approximation. Panel (c) is a sketch of the measurement mechanism and panel (d) are the Hopfield coefficients (1.94)-(1.93) associated to the best fit parameters. The zero momentum lower polariton exciton fraction is $C^2(0) \approx 0.05$

matrix. The pixel left from this threshold procedure were given a coordinate in the $(\theta(i), E(j))$ plane and a weight proportional to the counts number of the pixel. If we call Ω_1 the set of all the pixel surviving the threshold procedure which belongs to the lower polariton branch and Ω_2 the ones belonging to the upper polariton branch, the fit routine task is to minimize the quantity

$$\chi^2 = \sum_{(i,j)\in\Omega_1} [\,\hbar\omega_{LP}(j) - E(i,j)\,]^2 I(i,j) + \sum_{(i,j)\in\Omega_2} [\,\hbar\omega_{UP}(j) - E(i,j)\,]^2 I(i,j) \tag{3.6}$$

Where $\hbar\omega_{LP,UP}(j)$ is the upper or lower polariton branch analytical expression (1.90)-(1.89) evaluated for the wavevector $k_0 \sin(\theta(j))$ and $E(i,j)$ is the value $E(i)$ corresponding to the angle $\theta(j)$. The above equation is nothing more than the χ^2 evaluated for Poisson distributed events $E(i,j)$.

The function $\hbar\omega_{LP,UP}(j)$ depends on four parameters $(E_{cav}(0), E_{exc}(0), n_{cav}, 2\hbar\Omega_R)$ which are respectively the bare cavity photon and bare exciton eigenenergy at zero momentum, the effective index of refraction of the cavity and the Rabi splitting. Since the parameter space is huge a method to reconstruct the χ^2 function is to randomly pick the four values in a defined range of parameters with a uniform sampling distribution. This sampling was realized 10^6 times.

To estimate the best fit parameter error a good approximation is to fix three parameters and vary the one left free, since the expected χ^2 for N degrees of freedom and Q fitting parameters is $N-Q \approx N$ and the Chi^2 variance is $2N$, if χ^2_* is the chi squared for best set of fit parameters and x^* the expected value for the free parameter (i.e. $\chi^2(x)|_{x^*} = \chi^2_*$), then $\chi^2(x) = 2\chi^2_*$ implicitly defines the 1σ confidence level. One of the best fit is shown in figure 3.3-(b). We summarize the fit parameters for all the cavities SSP-(1) to SSP-(6) in table

SSP	n_{cav}	$E_{cav}\ (meV)$	$E_{exc}\ (meV)$	$2\hbar\Omega_R\ (meV)$	$X^2(0)$
(1)	3.60 ± 0.11	1469.76 ± 0.09	1476.78 ± 0.16	3.30 ± 0.14	0.048 ± 0.004
(2)	3.66 ± 0.08	1471.48 ± 0.22	1472.12 ± 0.18	3.34 ± 0.16	0.41 ± 0.04
(3)	3.58 ± 0.13	1470.10 ± 0.18	1470.48 ± 0.25	3.35 ± 0.16	0.44 ± 0.04
(4)	3.62 ± 0.09	1470.13 ± 0.06	1477.12 ± 0.15	3.34 ± 0.15	0.048 ± 0.005
(5)	3.54 ± 0.12	1469.42 ± 0.04	1481.22 ± 0.22	3.31 ± 0.09	0.019 ± 0.002
(6)	3.65 ± 0.11	1469.96 ± 0.05	1481.02 ± 0.17	3.33 ± 0.10	0.021 ± 0.001

Table 3.1: Best fit parameters for the rectangular planar cavities in group SSP motifs (1) to (6).

The error on the Hopfield coefficient $X^2(0)$ was propagated assuming negligible correlation in the fit parameters, in this semplified picture the error reads:

$$\sigma^2_{X^2} = \frac{\delta_R^4\left(\sigma^2_{Ec} + \sigma^2_{Ex}\right) + \left(E_{cav} - E_{Exc}\right)^2 \delta_R^2 \sigma^2_{\delta_R}}{4\left(\left(E_{cav} - E_{Exc}\right)^2 + \delta_R^2\right)^3} \tag{3.7}$$

where $\delta_R = 2\hbar\Omega_R$ is the Rabi splitting, and with σ we denote the standard deviation of the quantity reported as pedex label; notice that $C^2 = 1 - X^2$ implies that the error on C^2 must be equal to the X^2 one. As we anticipated in figure 3.1 the detuning gradient is positive along the x axis and also has a minor component along the y axis.

3.2 Micropillars

If we include a 2D confinement term in the driven-dissipative Gross-Pitaevsky equation (1.4.3) describing the polariton dynamics , the first intuitive consequence is the discretization of the polariton states. If we look at the steady state of equation (1.4.3) in absence of nonlinearity (i.e. for a weak pump) and we are interested in the real part of the eigenenergies, the problem becomes equivalent to the solution of a time independent Shrödinger equation in presence of an external potential $V_{ext}(x,y)$. The imaginary part of the eigenstates dictates the linewidth of the corresponding real-valued mode energy, we will address this problem in a second moment. We will focus on the circular micropillar structures in group (SCP) motif (4): thanks to the highly photonic lower polariton ($C^2(0) \sim 0.95$) these structures show a narrow linewidth and an enhanced photoluminescence, allowing very high quality measurements. The time-independent Shrödinger equation describing the confined polariton steady state reads

$$\left[\hbar\omega_0 - \frac{\hbar^2\nabla^2}{2m^*} + V_{ext}(x,y)\right]\psi(x,y) = E\,\psi(x,y) \tag{3.8}$$

where m^* is the effective mass of the polariton, and $\hbar\omega_0$ is the zero-point energy of the polariton states. As we mentioned in section 1.4.3 the confinement in the structures fabricated in C2N is provided by the refractive index mismatch between the semiconductor and the vacuum around the etched structure. Since the refractive index gap is huge, the polaritons get strongly confined by total internal reflection because of their photonic component; for a circular structure a good approximation for the potential well V_{ext} is

$$V_{ext} = \begin{cases} if\ (r \le R) & V_{ext} = 0 \\ if\ (r > R) & V_{ext} = \infty \end{cases} \tag{3.9}$$

where R is the radius of the structure. Thanks to the cylindrical symmetry the eigenfunctions of the probles can be written as the product of a radial part and of an angular part, it is convenient to write equation (3.8) in polar coordinates

$$\left[\hbar\omega_0 - \frac{\hbar^2}{2m^*}\left(\frac{1}{r}\frac{\partial}{\partial r}\,r\,\frac{\partial}{\partial r} + \frac{1}{r^2}\frac{\partial^2}{\partial\theta^2}\right) + V_{ext}(r)\right]u(r)\chi(\theta) = E\,u(r)\chi(\theta) \tag{3.10}$$

The angular part obeys a free particle hamiltonian and the radial part, in analogy with the well-know radial problem for the hydrogen atom, can be solved in terms of the Bessel functions $J_m(x)$, where m is the third component of the angolar momentum. Moreover The eigenenergies can be written in terms of the Bessel functions zeros $J_m(x_{m,n}) = 0$, where (n,m) labels the n-th zero of the m-th order Bessel function [50], as

$$E_{n,m} = \frac{\hbar^2}{2m^*R^2}x_{m,n}^2 + \hbar\omega_0 \tag{3.11}$$

and n is often called the principal quantum number. We also stress that every eigenstate with $m \neq 0$ is doubly degenerate because of the symmetry in $\pm m$ of equation (3.11) and every eigenenergy scales with R^{-2}. This latter property is intersting to our purposes and can be experimentally tested by measuring the spontaneous photoluminescence (PL) of the circular micropillars in group (SCP).

We firstly measured the (SCP) squared planar cavity to have a reference dispersion relation which is useful to understand the single pillar emission properties. The measurement follows the same experimental and postanalysis procedure explained in the previous section 3.1. From the fit of the dispersion

SCP	n_{cav}	$E_{cav}\,(meV)$	$E_{exc}\,(meV)$	$2\hbar\Omega_R\,(meV)$	$X^2(0)$
(4)	3.63 ± 0.08	1471.40 ± 0.09	1477.69 ± 0.19	3.31 ± 0.14	0.054 ± 0.006

The pillar PL was measured in transmission geometry adopting the setup configuration illustrated in section 2.2-(PHOTOLUMINESCENCE), since the in plane wave-vector is ill-defined for polaritons laterally confined in few micron sized structures, we directly imaged the real space PL emission on the spectrometer slit. Therefore the CCD rows and columns correspond to energy and space, since we are mainly interested in the ground state of the pillar, which has a symmetric s-type character, the slit tranverse position was alligned with the pillar center.

We show in figure 3.4 the PL of six micropillars with different diameters, the colorplot allows to appreciate both the modes profile and the discretization of the energy levels, it is clear from the figures that all the modes blueshift as the pillar diameter is decreased. Looking at the eigenmodes linewidth we observe a progressive broadening as the principal and angular quantum number increase, this can be related both to the fact that higher excited states are progressively localized close to the pillar edge experiencing and enhanced overlap with the free space radiative modes and to the fact that as they are blushifted from the bottom of the lower polariton band their excitonic component becomes higher thus resulting in a line broadening since $\gamma_{exc} \gg \gamma_{cav}$ and $\gamma_{LP} = C^2\gamma_{cav} + X^2\gamma_{exc}$. To verify quantitatively some of these statements we need to get informations on the mode shape and centroid. We can project along the spatial direction the colorplot in the bottom part of panels in figure 3.4 to get the energy resolved spectrum of the pillar emission which we show in the top part of the figure 3.4 panels. The eigenmodes energy can be easily retrieved by computing the centroid for the different peaks, but the lineshape and the linewidth related information requires some caution. Indeed what we are measuring is the convolution of the point-spread function of the spectrometer with the effective lineshape of the PL emission. We stress that the PL emission lineshape can be generally different from the true eigenmode lineshape due to the interaction of polaritons and reservoir, however in the very low

power pump regime, which we carefully attained in the experiments, these effects are negligible.

As we discussed in section 3.1 the point-spread function of the spectrometer can be modeled by a Voigt profile which results from the convolution of a Gaussian $\mathscr{G}(\mu,\sigma)$ and a Lorentzian $\mathscr{L}(\mu,\gamma)$ distribution

$$\mathscr{V}_{sp}(\mu,\sigma,\gamma) = \mathscr{G}(\mu,\sigma) \circledast \mathscr{L}(\mu,\gamma) \tag{3.12}$$

where μ is the expected value, σ the gaussian standard deviation and γ half of the lorentzian FWHM. Moreover the polariton lineshape results from the convolution of an homogeneus broadening due to the photonic component and an inhomogeneus term provided by the non-radiative recombination processes which characterize QW excitons (see section 1.4.2). The two terms can again be modeled respectively with a Lorentian and a Gaussian profile, and the polariton lineshape has a Voigt profile character, therefore what we are measuring is

$$\begin{aligned}
\mathscr{V}_{tot}(\mu,\sigma_T,\gamma_T) &= \mathscr{V}_{sp}(\mu,\sigma_s,\gamma_s) \circledast \mathscr{V}_{pol}(\mu,\sigma_p,\gamma_p) \\
&= \mathscr{G}(\mu,\sigma_s) \circledast \mathscr{G}(\mu,\sigma_p) \circledast \mathscr{L}(\mu,\gamma_s) \circledast \mathscr{L}(\mu,\gamma_p) \\
&= \mathscr{G}(\mu,\sqrt{\sigma_s^2+\sigma_p^2}) \circledast \mathscr{L}(\mu,\gamma_s+\gamma_p) \\
&= \mathscr{V}_{tot}(\mu,\sqrt{\sigma_s^2+\sigma_p^2},\gamma_s+\gamma_p)
\end{aligned} \tag{3.13}$$

Were we used the properties of the convolution operation and the fact that both the Lorenzian and Gaussian profiles belong to the Lévy symmetric α-stable distribution with $\alpha = 1$ and $\alpha = 2$ respectively and so their convolution is still a Lorentzian (Gaussian) profile. The Lorenzian profile resulting from the convolution has a FWHM which is the sum of the two convolved FWHMs whereas the Gaussian has a standard deviation which is the sum in quadrature of the two. As we know the convolution of the spectrometer and polariton lineshape, we can easily perform the deconvolution of the two terms once we compute (σ_T,γ_T) with a Voigt profile fit of the single modes in the energy resolved spectrum of the pillar structures.

In figure 3.5-(b) we plot the ground state energy as a function of the pillar radius. To compute the line centroid we fitted the projected spectra of figure 3.4 with a Voigt profile, as motivated by equation (3.13). We computed all the fit on the raw count vs pixel histograms via the Minuit-Fumili minimization libraries of ROOT, this choice allows to correctly propagate the spectrometer calibration error over the computed observables. Since the best fit parameters are often correlated, the error propagation needs to take in account the different covariance matrices. In general if we want to compute the observable $f(x_1,...,x_N)$ error, where $(x_1,...,x_N)$ are correlated variables, the leading error term reads

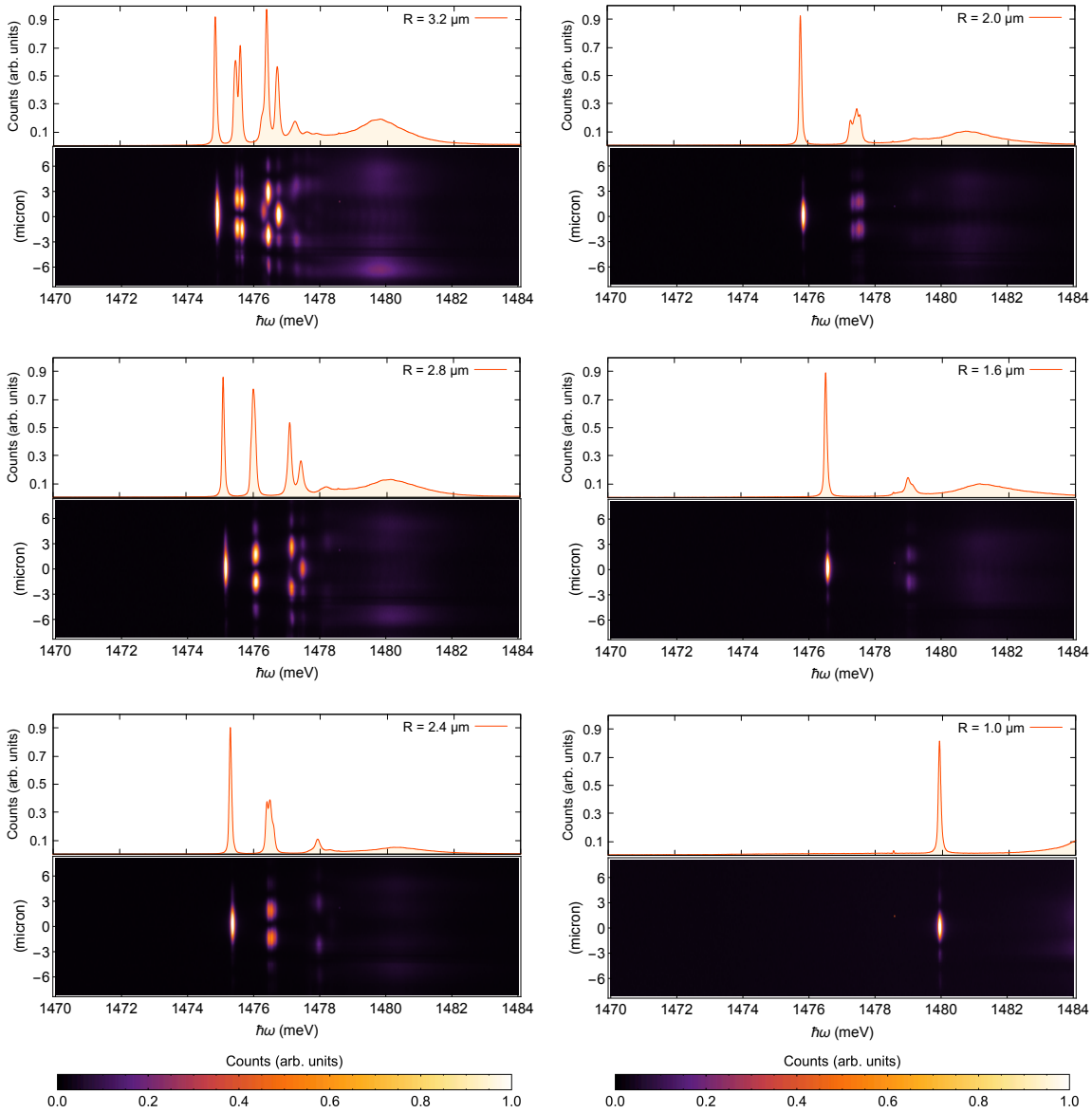

Figure 3.4: Colorplots: Energy and space resolved emission of six micropillars with a radius included between 1.0 and 3.2 μm. The projection along the spatial coordinate of the colorplot is shown on top and highlights the discretization of the polariton modes in the micropillar. These structures can be regarded as artificial hydrogen-like atoms: from the colorplots one can appreciate the s-type character of the ground state and the two lobe profile of the first p-type excited state. Some of the excited modes show a small energy splitting, this happens because if the structure is slightly elliptical a linearly polarized polarized light which is not orthogonal to one of the major ellipse axis can excite both the modes which have a small energy difference proportional to the ellipticity of the micropillar's section, this also breaks the $\pm m$ symmetry of the eigenmodes and may result in an effective spin orbit coupling with the TE-TM energy splitting of the DBRs. However all these features does not influence the ground state because it is maximally symmetric.

$$\sigma_f^2 = \left[\partial_i f(x_1,...,x_N)(Cov(\sigma_1,...,\sigma_N)^i{}_j \, \partial^j f(x_1,...,x_N) \right]_{(x_1,...,x_N)=(x_1^*,...,x_N^*)} \tag{3.14}$$

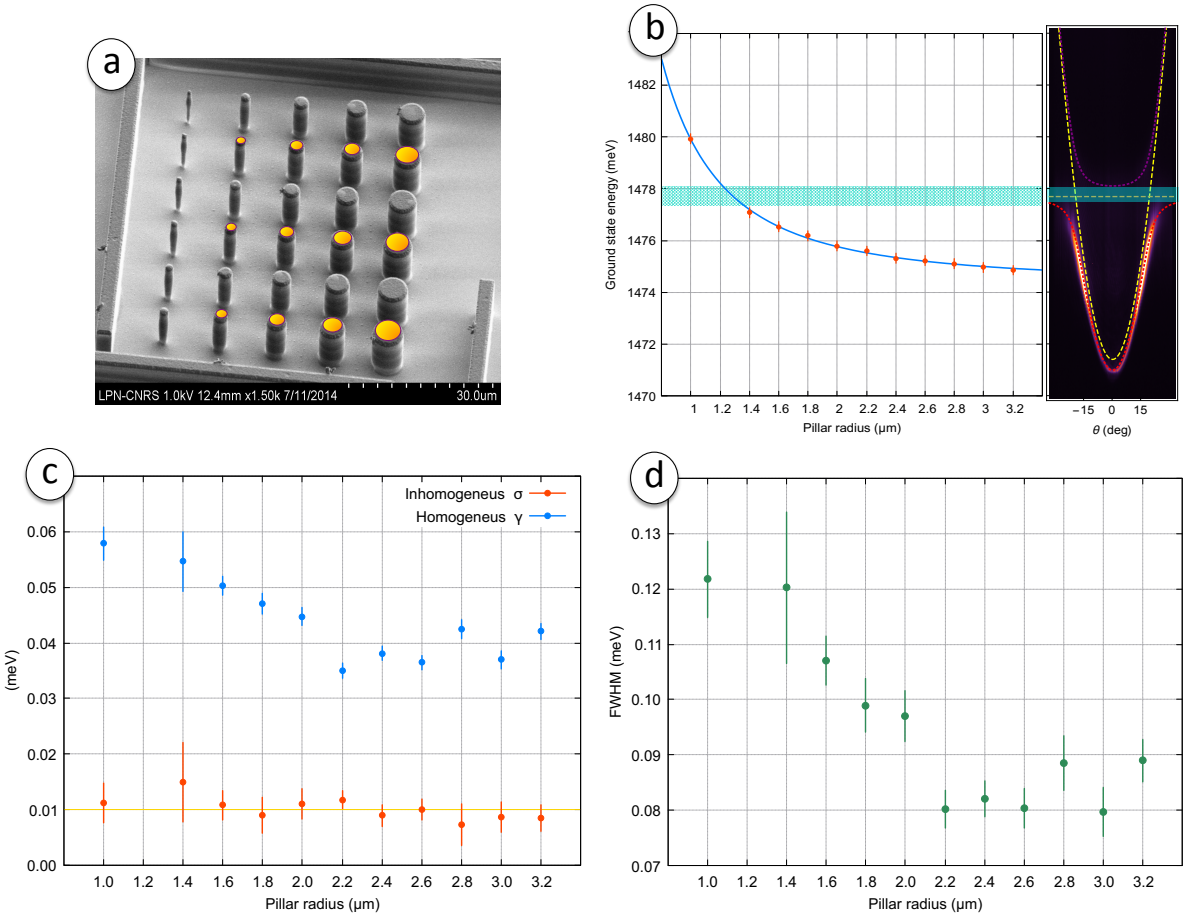

Figure 3.5: (a)-SEM image of the micropillar structures, the orange spots marks the probed structures, the pillars diameter increases left to right and top to bottom. (b) ground state energy blueshift as a function of the pillar radius, the solid blue line is a weighted fit in the form prescribed by equation (3.11) showing good agreement between the theoretical predictions and the experiment. In the right part of the panel the (SCP)-(4) planar cavity dispersion is plotted, the turquoise shaded area corresponds to the upper-lower branch gap where the polariton states density should be ideally null. The pillar having $R = 1.4\ \mu$m had a dark ground state since the mode layed in between the gap. (c)-Deconvolved homogeneus and and inhomogeneus contributions to the ground state linewidth. (d)-Deconvolved FWHM of the ground state line as a function of the pillar radius, the corresponding polariton lifetime varies between 16 and 10 picoseconds.

where $\sigma_1,..,\sigma_N$ are the standard deviations associated to the maximum Likelihood point $(x_1^*,...,x_N^*)$, and $Cov(\sigma_1,...,\sigma_N)^i{}_j$ is the covariance matrix of the $(x_1^*,...,x_N^*)$ parameters and is related to the Likelihood Hessian matrix.

If the Voigt profile best fit to figure 3.4 spectra is $\mathscr{V}_{tot}^*(\mu^*,\sigma_T^*,\gamma_T^*)$ and the centroid position pixel is μ^*, the ground state energy can be computed via equation (3.1), which depends on

the calibration slope m and offset q, which are correlated statistical variables. Since (m,q) are uncorrelated with μ^* the covariance matrix will have the block-diagonal form

$$Cov(\sigma_{\mu^*},\sigma_m,\sigma_q) = \begin{pmatrix} \sigma^2_{\mu^*} & 0 \\ 0 & Cov(\sigma_m,\sigma_q) \end{pmatrix} \tag{3.15}$$

and the computation of the error is straighforward algebra. The result of this analysis is plotted in figure 3.4-(b). The experimental points can be fitted with the infinite circular well eigenstate formula (3.11) letting as free parameters m^* and $\hbar\omega_0$ and from the weighted best fit we obtained

$$\overline{m^* = (3.98 \pm 0.06)\cdot 10^{-5} m_e \quad \hbar\omega_0 = (1474.39 \pm 0.03)\, meV}$$

The good agreement between experimental data and the infinite well model suggests that the hypotesis of complete polariton confinement by total internal reflection of the photonic component is a fair approximation. This measurement is intersting because it allows a precise and direct measurement of the polariton effective mass which otherwise has to be inferred from the effective length L_{eff} of the Fabry-Pérot cavity and from the effective refractive index n_{eff} which are more exotic quantities often carrying a consistent uncertainty.

The linewidth of the ground state can be addressed if the best fit Voigt profile $\mathscr{V}^*_{tot}(\mu^*,\sigma^*_T,\gamma^*_T)$ is deconvolved from the spectrometer poin spread distribution $\mathscr{V}_{sp}(\mu,\sigma_s,\gamma_s)$. The parameters σ_s,γ_s are known from the previous section, and are correlated trough $Cov_s(\sigma_{\sigma_s},\sigma_{\gamma_s})$. The same holds for (σ^*_T,γ^*_T) and the deconvolution -as captured by equation (3.13)- corresponds to the calculation of the quantities

$$\sigma_p = \sqrt{\sigma^2_T - \sigma^2_s} \tag{3.16}$$

$$\gamma_p = \gamma_T - \gamma_s \tag{3.17}$$

which have to be converted in pixel trough the relation

$$f(pix) \approx \frac{hc\, m}{q^2}\, pix \tag{3.18}$$

valid if $pix \ll q$; here h is the Plank's constant and c the speed of light. The composition of equation (3.18) with (3.16) depends on the four parameters (σ_T,σ_s,m,q) or (γ_T,γ_s,m,q). Again the covariance matrix has the block-diagonal form $diag(\sigma^2_{\sigma_T},\ \sigma^2_{\sigma_s},\ Cov(\sigma m,\sigma q))$. The homogeneus and inhomogeneus contribution γ_p, σ_p to the polariton linewidth are plotted in figure 3.5-(c). The constant inhomogeneus contribution $\langle\sigma\rangle \sim (10.4 \pm 0.03)\mu eV$ (solid yellow line) reflects the fact that the QW exciton Bohr radius is much smaller than the pillar size and thus the confinement does not influence the exciton properties. This is only true if the etching procedure does not degrade the QW and if the radius of the pillar is greater than $\sim 0.5\ \mu$m

otherwise sidewalls recombination effects start to play a role in the exciton linewidth. The increasing homogeneus term as the pillar size decreases depends on the increased side to mirror surface ratio

$$\Gamma = \frac{2\pi R L_{eff}}{\pi R^2} = \frac{2L_{eff}}{R} \tag{3.19}$$

which reflects in an enhanced polariton coupling with free space modes trough lateral losses. Finally we can retrieve the confined polariton lifetime by calculating the FWHM of the ground state lineshape, as discussed in the previous section thi can be done trough equation (3.4) once σ_p and γ_p are known. The error computation again relies on equation (3.14), now the variables are six $(\sigma_p, \gamma_p, \sigma_s, \gamma_s, m, q)$ and are correlated in groups of two. The calculated polariton lifetime is between 16 and 10 picoseconds, and degrades as R gets smaller as expected.

Finally we calculated with a finite element approach (via Mathematica's FEM package) the first ten eigenmodes density profile of the pillar, the results are plotted in figure 3.6. We set all the simulation parameters to match the best fit estimators m^* and $\hbar\omega_0$ provided by the fit of (3.11) on the experimental data. Once we have the 2D plot for the mode profiles we can deduce which shape would be imaged on the CCD by the spectrometer. The computed profiles are in good agreement with the experimental ones. The simulation is also able to reproduce the first 4 eigenenergies, however the higher modes does not match the experimental data, this has to do with the fact that the particle mass was fixed in the simulation while the polariton mass runs with the mode-to-lower polariton detuning.

It's noteworthy that the calculated mode profiles have close resemblance with the hydrogen atom electronic orbital density $\rho_{n,l,m} = |\psi^H_{n,l,m}|^2$: mode (a) and $\rho_{1,0,0}$, (b)-(c) and $\rho_{2,1,\pm1}$, (d)-(e) and $\rho_{3,2,\pm1}$, (f) with $\rho_{2,0,0}$, (g)-(h) with $\rho_{4,3,\pm1}$ and (i)-(l) with $\rho_{3,1,\pm1}$. This encourages the analogy between the pillar structures and hydrogen-like atoms, and paves the way to the study of more complex molecules, where the single artificial atom level structure can be engineered trough the pillar shape. The great advantage of working with photonic molecules is that the orbital structure can be directly imaged by means of spatially and energy resolved photoluminescence experiments. Recently the coupling of six equal pillar structures arranged in a hexagon's vertices allowed to emulate a chiral Benzene-like molecule [51].

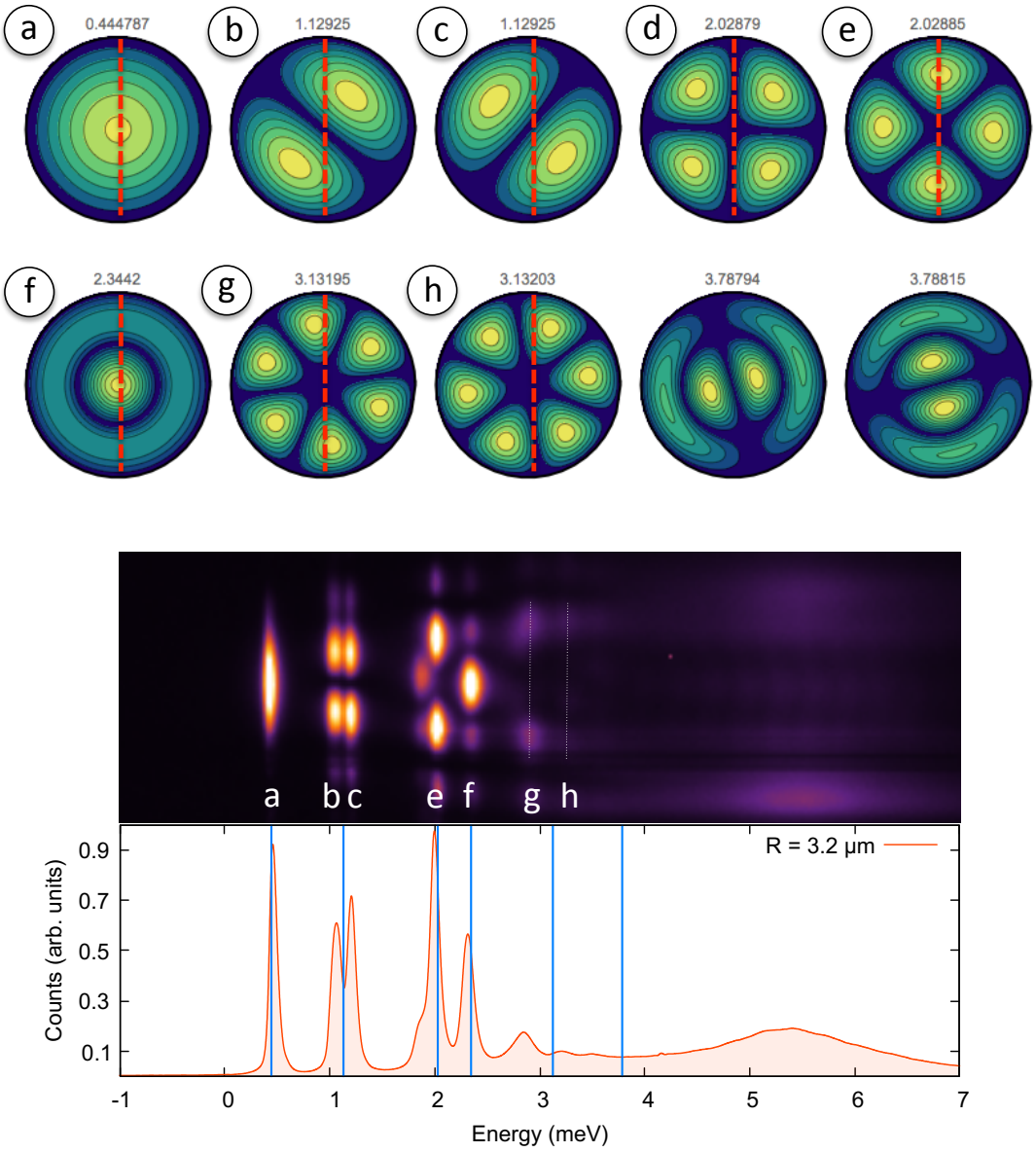

Figure 3.6: (a) to (l): finite element simulation of the first ten eigenmodes density profile (i.e $|\psi_{n,m}(r,\theta)|^2$) of a particle in an infinite circular potential well with $R = 3.2\mu m$: every eigenmode has n radial nodes and $|m|$ nodes on a circle. The red dashed line represents the spectrometer slit position: the energy and space resolved emission reported in the colorplot shows the corresponding mesured mode profile showing good agreement. Notice that the mode (d) is dark because of the slit position in our configuration. On top of every simulated mode density profile we report the blueshift respect to the point-zero energy $\hbar\omega_0$: the theoretical predictions are shown as blue lines in the corresponding experimental energy spectrum. The agreement is again pretty good for the first four modes, the modes (b)-(c) are splitted in the experimental dataset because of the pillar ellipticity and TE-TM splitting, as previously discussed. Concerning the predicted higher eigenmodes blueshift, the bad agreement whith the experiment can be ascribed to the absence in our simulation of an effective mass drift as the mode detuning respect to the lower polariton branch increases. Indeed theory predicts an effective polariton mass running with the Hopfield coefficients which are mode detuning dependent (equations (1.96)-(1.95)) as the parabolic band approximation conditions are not fulfilled (i.e. for large detunings from $\hbar\omega_{LP}(0)$).

3.3 Temperature and Interactions

In this section we address the possibility of tuning the nonlinearity of pillar structures with temperature. As discussed in section 1.4.3 polariton polariton interaction in the lower dispersion band has the form -(1.110)-

$$\Gamma^{LP}_{\sigma,\sigma'}(\mathbf{k}) \approx |X(\mathbf{k})|^4 \Gamma^{XX}_{\rightrightarrows} \tag{3.20}$$

and the polariton dynamics in a planar cavity is described by the driven-dissipative Gross-Pitaevsky equation (DD-GPE) (1.4.3). However in a micropillar structure the in plane wavevector is anymore a good quantum number and the allowed energy states are discretized: within some boundaries these properties allows to greatly simplify the equations describing the polariton dynamics . Indeed if the energy level spacing between the ground state and the first excited state is much bigger than the sum of the two linewidts we can disregard the excited states and substitute to the polariton wavefunction the single mode ansatz

$$\Psi_{LP}(\mathbf{r},t) = \sqrt{N(t)} e^{i\phi(t)} \tag{3.21}$$

and if we are interested in the steady state of the pillar under a coherent driving $E(t) = E_0 e^{i\omega t}$ the above ansatz reduces to

$$\Psi_{LP}(\mathbf{r},t) = \psi_{ss} e^{i\omega t} \tag{3.22}$$

where $\sqrt{N} = \psi_{ss}$, plugging this ansatz in the DD-GPE, (1.4.3) becomes

$$\left(\hbar\omega_{GS} - \hbar\omega - i\frac{\gamma_{GS}}{2}\right)\psi_{ss} + U|\psi_{ss}|^2\psi_{ss} + F = 0 \tag{3.23}$$

which describes a single mode resonator with a nonlinear term $U = \Gamma^{XX}_{\rightrightarrows} X^4_{GS}$ under a coherent driving with amplitude $F = \eta_{LP} E_0$. The ground state energy blueshift induced by the nonlinearity at given pump power is $\propto U|\psi_{ss}|^2$ and $|\psi_{ss}|^2 \propto F/\gamma_{GS}$, since $N = |\psi_{ss}|^2$ is the polariton occupation number in the pillar ground state, the effective Kerr nonlinearity reads

$$\chi^3 = \frac{\Gamma^{XX}_{\rightrightarrows} X^4_{GS}}{S\,\gamma_{GS}} \tag{3.24}$$

where S is the ground state mode section and $\Gamma^{XX}_{\rightrightarrows}$ is the copolarized polariton-polariton Pauli exchange interaction constant described in section 1.4.3. While S and $\Gamma^{XX}_{\rightrightarrows}$ are constants, X^4_{GS} depends on the pillar ground state detuning from the planar cavity lower band at zero momentum $\hbar\omega_L P(0)$. Indeed for a planar cavity is close enough to a pillar structure, so that the exciton-cavity photon gradient is negligible, if $\hbar\omega_L P(k) = \hbar\omega_{GS}$ for $k = k^*$, then $X^2_{GS} = X^2_{LP}(k^*)$. Tuning the pillar ground state detuning from the fundamental planar cavity mode is therefore equivalent to control the nonlinearity of the pillar structure.

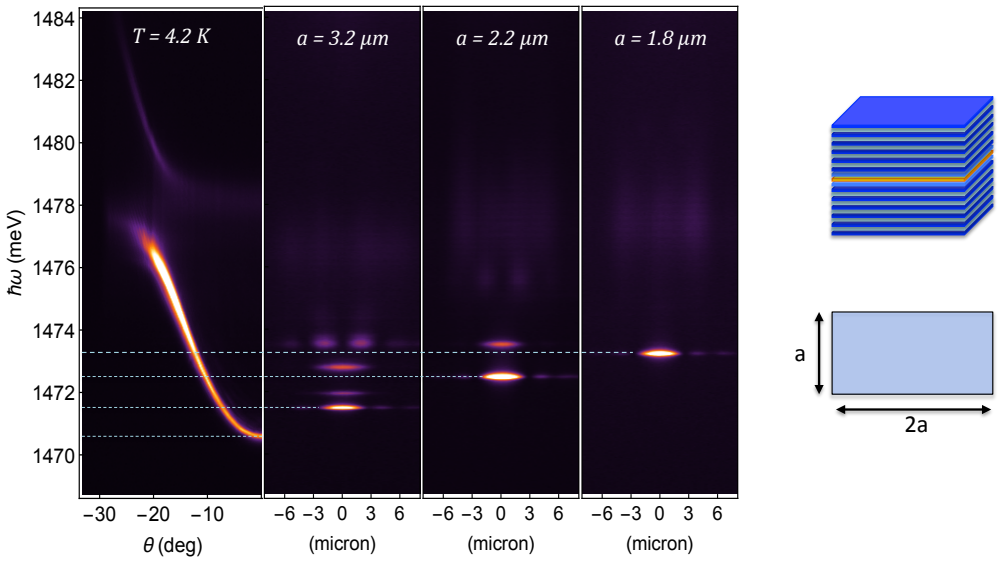

Figure 3.7: From left to right: Energy and momentum resolved PL of the (SSP)-(4) planar cavity at 4.2 K, Energy and space resolved PL of three neighbouring rectangular pillar structures. Decresing the pillar size a reflects in a ground state energy blueshift in analogy with the eigenmodes of a particle in a box $E_n \propto n^2/a^2$. The pillar ground state detunings from the bottom of the lower polariton band are respectively $\Delta E_1 \approx 0.91\ meV$, $\Delta E_2 \approx 1.86\ meV$ and $\Delta E_3 \approx 2.66\ meV$.

A well know property of QW bare excitons is that their emission peak redshifts with temperature [52]-[53]-[54] and the linewidth increases due to enhanced electron-phonon interactions [55]-[56]. If the exciton line redshifts the planar cavity exciton-photon detuning $\delta(T)$ decreases if $\delta_0 < 0$, then $X^2(0)$ increases (equation (1.93)). If the $X^4(0)$ growth rate with T dominates the exciton line broadening, the pillar nonlinearity increases because of equation (3.24) and viceversa. However as the planar cavity exciton shifts, as well the excitonic component of the pillar ground state shifts, and also the index of refraction of the Fabry-Pérot cavity may change with T therefore affecting also the cavity resonant-modes. The interplay of all these factors is quite complex and will be the topic of this section.

In order to have a complete characterization of the different phenomena occurring when the system temperature is modified we will both record the planar cavity dispersion at different temperatures to keep track of the bare exciton and photon dispersion, both keep detailed information of the pillar groundate energy and linewidth. We focused in motif (SSC)-(4) where a $200 \times 100\ \mu$m planar cavity and a set of rectangular micropillars with a fixed 2:1 aspect ratio and variable sectional area We decided to focus our attention on three different pillars with the shortest side a measuring (right part in figure 3.7)

$$a_1 = 3.2\ \mu m \quad a_2 = 2.2\ \mu m \quad a_1 = 1.8\ \mu m$$

As we demonstated in the previous section, confined polaritons in a micron-sized cavity have the lowest linear eigenmodes which can be calculated by means of a time independent Schrödinger equation for a particle having mass $m = m^*_{LP}$ in presence of an infinite well with the shape of the pillar section. The rectangular cavity is equivalent to the solution of a particle in a box eigenmodes

$$E_{n,m} = \frac{\hbar^2\pi^2}{2m^*_{LP}}\left(\frac{n^2}{a^2} + \frac{m^2}{4a^2}\right) \tag{3.25}$$

If the pump beam is linearly polarized along the shorter (longer) rectangle side the $m \neq= 1$ ($n \neq= 1$) modes are dark. The ground state energy shifts with a_i^2, allowing to study the temperature dynamics for different pillar ground state to lower polariton detunings. In figure 3.7 we show the (SSC)-(4) planar cavity dispersion alongside the three PL emissions, showing the ground state blueshift with the pillar side dimension, the measured shift is in good agreement with the predictions calculated using the nominal pillar size within few percent, showing that the etching technique ensures precise control on the pillar size on orders of some dozen nanometers.

Whereas PL measurements are accurate enough to characterize the polariton bands, a precise information on the pillar linewidth with few percent relative error demands for resonant transmission experiments, where the transmission function $T(\omega)$ of the pillar can be probed with a spectral accuracy limited only by the single mode laser step $\Delta\lambda = 0.1\ pm$. Since the transmission $T(\omega)$ is proportional to the steady state dissipated power at a given frequency (i.e. the real part of the transfert function of the pillar), the lineshape of the ground state can be characterized by transmission experiments. The measurement consisted in recording the real space emission of the pillar with the CCD at constant intervals of time while the single mode laser frequency was scanning. When the laser is off resonance with a pillar mode the CCD appears dark, as the laser get resonant with the pillar ground state a bright real space image of the mode profile is visible on the CCD, a Region of Interest (ROI) including the mode profile can be defined on the CCD, and the transmission spectrum $T(\omega)$ can be calculated as

$$T(\omega_k) \propto \sum_{(i,j)\in ROI} I(i,j,k) \tag{3.26}$$

where $I(i,k,k)$ is the (i,j)-th pixel intensity in the frame k corresponding to a pump frequency ω_k. We sketch the process in figure 3.8-(c); the real space emission shown in the figure is the pillar three emission when pumped resonantly on the ground state, a slightly elliptical TEM_{00} mode profile can be appreciated due to the asymmetry of the cavity quantization axes.

In figure 3.8-(a) we show the planar cavity polariton bands as a function of the temperature, it is evident a redshift affecting both the bare exciton and cavity photon mode even if the exciton line shifts at a faster rate. The cavity mode redshifts becuse the refractive index of semiconductor

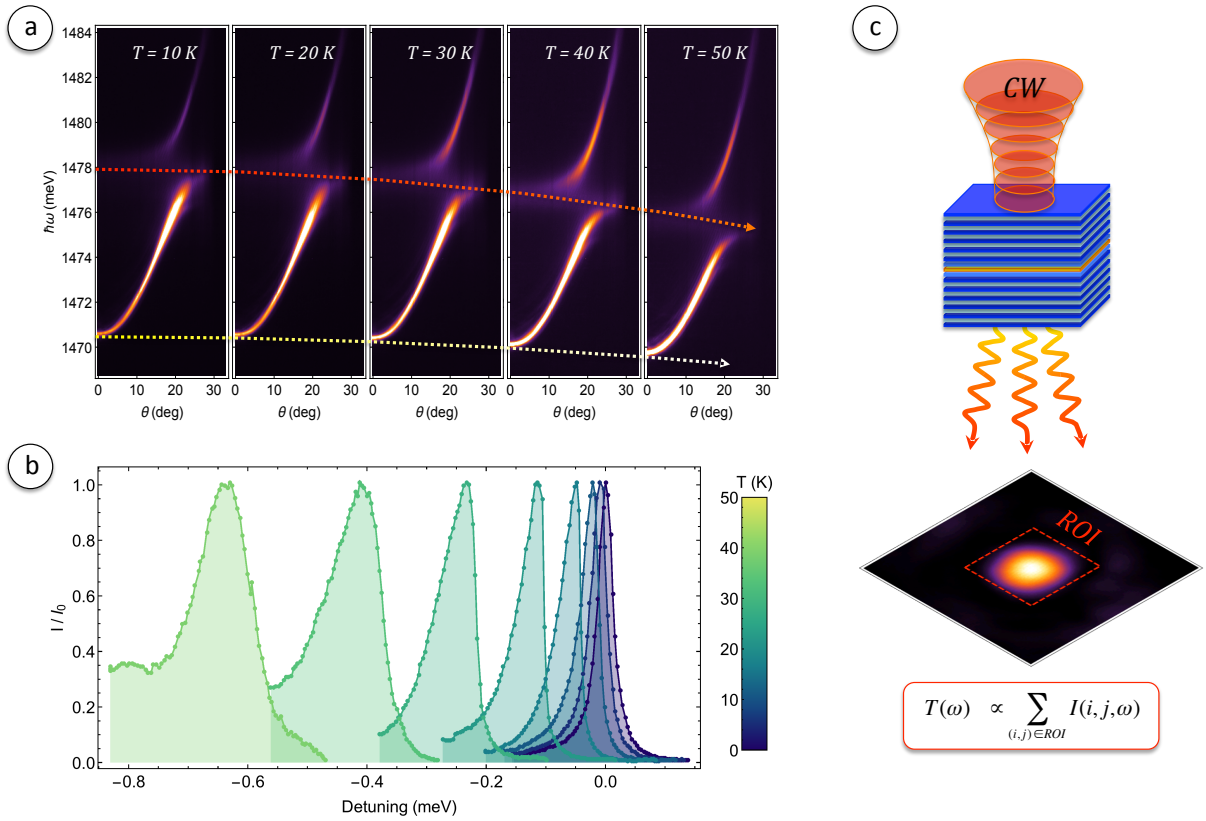

Figure 3.8: (a)-Planar cavity polariton bands as a function of the temperature: both the bare exciton and cavity photon mode are redshifting, but the exciton at a faster rate. (b)-Pillar three, if $\hbar\omega^0_{GS}$ is the ground state energy at $4.2K$ we plot the normalized transmission spectrum $T(\omega-\omega^0_{GS})/T(\omega_{GS})$ from 4 K to 40 K. The lineshape at 4 K is in good approximation symmetric whereas at higher temperature the lower energy tail progressively grow, this effect can be related to the enhanced scattering processes between excitons and phonons which can act as dark state and mediate a transition also for off resonant pump photons.

materials depends on many diffrent factors, among them the fundamental Γ point gap energy which depends on temperature [54]: if the refractive index changes the cavity mode shifts to preserve the Bragg relation.

Figure 3.8-(b) shows the resonant transmission spectra for pillar three for eight different temperatures between 4 and 40 Kelvin degrees. The pillar ground state energy also redshifts because the lower polariton states which occupy the mode can be written in the bare exciton-photon basis trough the Hopfield coefficients (1.94)-(1.93) as demonstrated in section 1.4. One then expects the pillar ground state experiences a redshift proportional to the weighted sum of the bare cavity and exciton redshifts for the Hopfield coefficents. Another clear feature is the broadening of the lineshape: one of the main mechanisms contributing to this effect is electron-phonon interaction which is greatly enhanced at higher temperatures. The cross section of the process is directly

proportional to the phonon density of states, which reads

$$n(\hbar\omega_{pn}) \propto \left(e^{\frac{\hbar\omega_{pn}}{k_B T}} - 1 \right)^{-1} \tag{3.27}$$

which is the Bose-Einstein distribution since phonons can be described as massless bosons. The characteristic Debye temperature in semiconductors is order of some meV, then the phonon density of states is negligible at $4K$ increasing exponentially for higher temperatures. The signature of electron-phonon interactions is the low energy tail of the ground state lineshape which becomes more and more asymmetric as the temperature increases, this happens because the phonon population can mediate trough scattering processes some transitions from optically dark states. For every temperature we recorded the linewidth and the ground state transmission peak position.

Let now describe the different shidts from a euristic but quantitative point of view. The first phenomenon we want to address is the bare exciton redshift with temperature which essentially depends on the Γ point energy gap $E_g$between the valence and the conduction band. Two main mechanism may affect E_g, the first one is originated by the temperature-dependent dilatation of the lattice [52]. This contribution is linear with temperature at high temperatures, whereas at low temperatures the thermal expansion coefficient is nonlinear with T; correspondingly the dilatation effect on the energy gap is also nonlinear. A second contribution comes from the electron-phonon interaction and has to be proportional to the phononic density of states (3.27). For $T < T_D$ where T_D is the Debye temperature of a semiconductor, the exciton peak emission reads [57]-[53]

$$E_X(T) = E_X(0) - \frac{2\kappa_{pn}}{e^{\,\theta/T} - 1} \tag{3.28}$$

where θ is a parameter related to the Debye temperature and κ_{pn} is the exciton-phonon interaction strength. Regarding the cavity resonance redshift, since the eigenmodes are fixed by the bragg relation

$$E_\alpha(n_{cav}) = \frac{hc}{\lambda_\alpha} = \alpha \frac{hc\, n_{cav}}{2L_{eff}} \tag{3.29}$$

if n_{cav} decreases the cavity mode redhifts. The refractive index of a III-V semiconductor has a complex dependence in T which usually can be described in terms of a Sellmeier's equation which derives from the Taylor series expansion of the dielectric function. However at low temperatures the two main mechanisms influencing the change in the refractive index are the termal expansion of the lattice and the energy gap dependence on T, the Penn-Ravidra model [54] suggest the semi-emiprical relation

$$\frac{dn}{dT} = \sigma \frac{dE_g}{dT} \approx \sigma \frac{d E_X(T)}{dT} \tag{3.30}$$

and σ is a coefficient to determine. In first approximation the refractive index changes as

$$n(T) = n(0) + \frac{dn}{dT} T = n(0) - \frac{\alpha}{T(\cosh(\beta/T) - 1)} \tag{3.31}$$

obtained by differentiation of equation (3.28), notice that we called the constants α and β even if an explicit relation with κ_{pn} and θ exists because the QW semiconductor is an InGaAs alloy and the cavity spacer is GaAs so the Debye temperature and phonon-exciton interactions may be different. Finally we end with two functions modeling the bare exciton and cavity photon redshift, we will use hereafter the handy notation

$$f_{exc}(T) = \frac{2\kappa_{pn}}{e^{\,\theta/T} - 1} \tag{3.32}$$

$$f_{cav}(T) = \frac{\alpha}{T(\cosh(\beta/T) - 1)} \tag{3.33}$$

This is enough to model the pillar lower polariton ground state redshift: from the Hopfield relation between the polariton basis and the exciton-cavity photon basis we can fairly assume that the groundtate redshifts as

$$f_{GS}(T) \approx (C_{eff}^2 - 1) f_{exc}(T) - C_{eff}^2 f_{cav}(T) \tag{3.34}$$

where C_{eff}^2 is an effective Hopfield photonic coefficient. We use the term *effective* because in line of principle C^2 also depends on temperature: to get rid in a first order approximation of this contribution we adopt the coefficient $C_e^2 ff$ which will lay somewhere in between $C^2(T_{min})$ and $C^2(T_{max})$. The last term we need to describe is the ground state linewidth broadening, the literature about this topic is generous [55]-[56]-[53], the essence is that the homogeneus linewidth broadens because of the interaction both with acoustic and optical phonons, whereas the inhomogeneus term broadens because of the exciton enhanced scattering with fully ionized impurities and depends on the average binding energy of such impurities. A good approximation for all these contribution has the form

$$\begin{aligned} \gamma(T) &= \gamma_0 + \sigma T + \kappa_{op}(e^{\theta/T} - 1)^{-1} \\ &\approx \gamma_0 + \sigma T + \kappa_{op}\, e^{-\frac{\theta}{T}} \end{aligned} \tag{3.35}$$

valid if $\theta/T \gg 1$, where γ_0 is the temperature independent linewidth, σ and κ_{op} are respectively proportional to the acoustic phonon and optical phonon coupling constant and θ has the meaning of a debye temperature for the optical phonons.

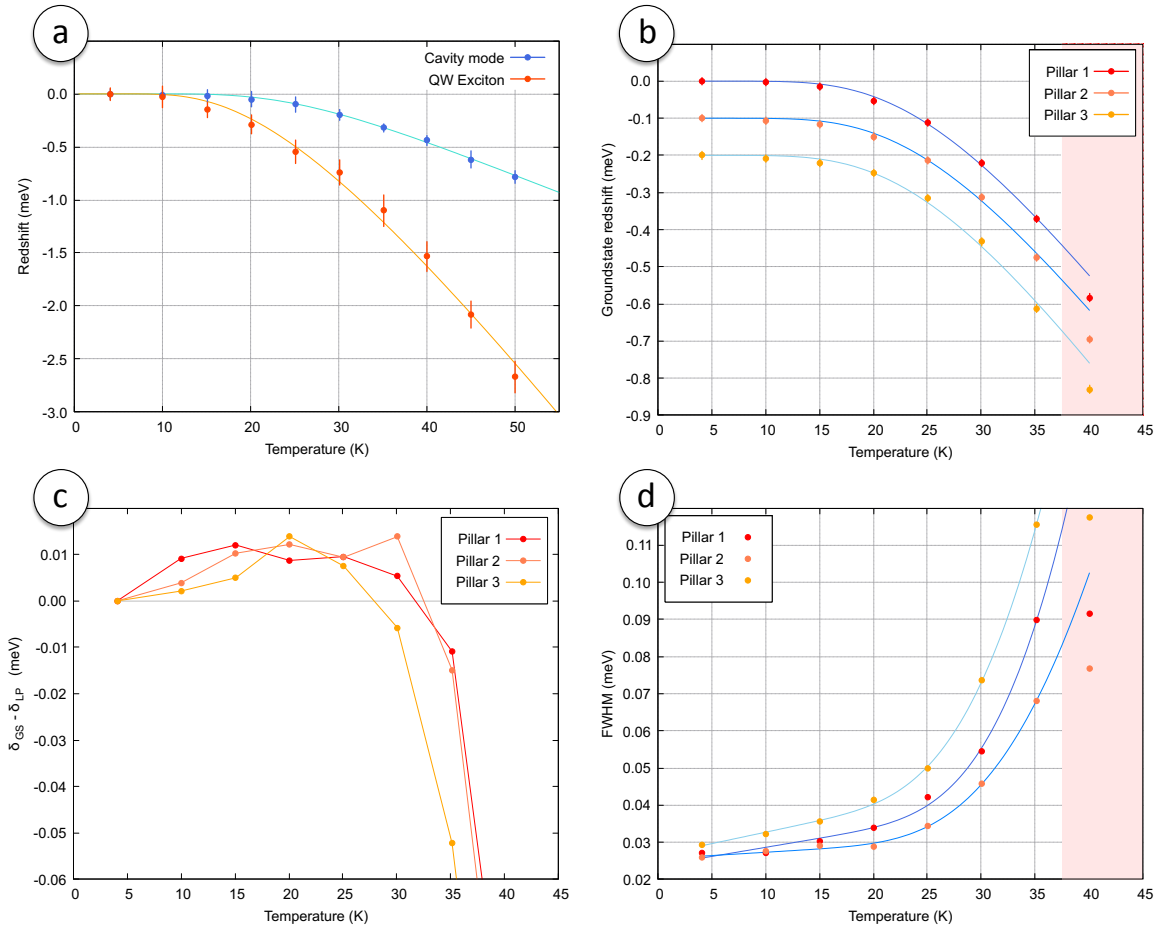

Figure 3.9: (a)-Bare exciton and cavity photon redshift, the experimental data points were derived from the planar cavity dispersion fitting procedure described in section 3.1. The orange and light-blue curves are the weighted best fits of equation (3.32)-(3.33) respectively: the fit reproduces fairly the data. (b)-Pillar ground state redshift, the data correspond to the calculation of the resonant transmission peak, the error on the peak position is dominated by a $\sim 10\ \mu eV$ uncertainty due to the syncronization procedure of the CCD frame autoclick with the laser scan log. The data of the second (third) pillar are shifted by $0.1\ meV$ ($0.2\ meV$), to clearly distinguish the three curves. The solid lines are the best fits of equation (3.34), notice that the only free parameter was C^2_{eff}, being the other parameters fixed by the two fits of (3.32)-(3.33) to the bare exciton and cavity photon in panel (a). The data with $T > 35K$ were excluded from the fit because they were outlayers. (c) Relative detuning from the cavity lower polariton of the pillar ground state, we subtracted the zero temperature detuning to better appreciate the variations which are on orders of tens μeV. (d)-ground state linewidth broadening, the solid lines are fits based on (3.35), as in panel (b) the data with $T > 35K$ were excluded from the fit because they were outlayers.

In figure 3.9 we summarize the experimental results concerning the bare exciton and cavity redshift (a), the ground state resdshift (b) and the linewidth broadening (d). In panel (a) the data relative to the exciton and cavity photon energy at zero wavector were extracted from the joint fit of equation (1.90)-(1.89) with the technique discussed in section 3.1. We fitted the

experimental data with (3.32)-(3.33) obtaining

$\kappa_{pn} = (4.04 \pm 0.21)\ meV$	$\theta = (71.4 \pm 4.7)\ K$
$\alpha = (243 \pm 16)\ meV\ K$	$\beta = (133.9 \pm 3.7)\ K$

with this parameters the curves shows good agreement with the experimental data. In panel (b) the centroid of the resonant transmission spectrum (see figure 3.8-(b)) was calculated for the three pillars. The experimental data were fitted with (3.34), as consistency requirement we assumed in this operation that $f_{cav}(T)$ and $f_{exc}(T)$ were fixed by the above best parameters fit of panel (a). We find the three effective Hopfield coefficients

$$C^2_{eff,1} = (0.945 \pm 0.004) \quad C^2_{eff,2} = (0.929 \pm 0.007) \quad C^2_{eff,3} = (0.916 \pm 0.009)$$

The proposed fitting function interpolates the redshift of the ground state fairly good in the $(0 < T < 35)\ K$ range, but the $40\ K$ experimental data seems to be outlayers: this effect seems to us having nothing to do with artificial systematic errors due to the data analysis, since presents also in panel (d) for the linewidth broadening. Two possible issues are connected to the imperfect termalization of the sample or to some effect which triggers at higher temperatures, being probably ascribable to impurities or defect center activation. In panel (d) we show the full width at half maximum (FWHM) of the three pillars as a function of temperature, the data points were fitted with (3.35)

Pillar	$\gamma_0\ (\mu eV)$	$\sigma\ (\mu eV\,/\,K)$	$\kappa_{op}\ (meV)$	$\theta\ (K)$
1	23.7 ± 1.6	0.49 ± 0.05	15.2 ± 3.1	198 ± 30
2	25.4 ± 0.8	1.78 ± 0.20	7.6 ± 0.9	188 ± 15
3	26.5 ± 1.0	6.18 ± 0.34	11.8 ± 1.7	182 ± 9

again the fits fairly reproduce the experimental data in the $(0 < T < 35)\ K$ range. For high temperatures the releation between the lineshape FWHM and the radiative lifetime of the cavity becomes ill-defined, indeed the low-energy tail of the resonant transmission spectrum increases with T skewing the peak profile -see figure 3.8-(b)-, without complicating the tractation of the temperature dependence to include these effects we can just restict the analysis in the $(0 < T < 35)\ K$ region. From a practical point of view this is also motivated by the progressive worsening of the optical quality of the pillar emission due to thermal effects which becomes critical above $(35 - 40)\ K$, the high temperature region becomes then unintersting because of the overwhelming thermal noise which spoils the quality of the measurements.

Finally we plot in panel (c) the relative detuning of the pillar ground state from the cavity lower polariton: positive values suggests that exists a region $(0 < T \lesssim 35)\ K$ where the ground state has a smaller redshift respect to the lower polariton, correspondingly the grounstate excitonic fraction increases faster than the exciton fraction for the bottom of the lower polariton band.

Finally we propose a model based on equations (3.32)-(3.33)-(3.34) to describe the scaling law of the excitonic Hopfield coefficient (1.93) with temperature, which is the last ingredient we need to predict the dependence of pillar effective Kerr nonlinearity (3.24) with T. The first assumption is that the zero temperature pillar grounstate energy lays in the range of applicability of the parabolic band approximation to the lower polariton branch, which safely holds for all the three pillars we are characterizing, as figure 3.7 demonstrates. Therefore we can write

$$E_{LP}(\theta) \approx E_{LP}(0) + \eta\theta^2 + \mathscr{O}(\theta^3) \tag{3.36}$$

where $n_{cav}k_{||} = k_0 \sin\theta$. Within the same approximation if $E_{LP}(\theta) = E_{GS}$ for $\theta = \theta_*$, then at a given temperature $\eta\theta_*^2 = \delta_{GS-LP}$, where $\delta_{GS-LP} > 0$ is the detuning of the lower polariton respect to the pillar ground state, in general

$$\theta_*^2(T) = \frac{1}{\eta}\delta_{GS-LP}(T) \tag{3.37}$$

Now the Hopfield exciton coefficient within parabolic band approximation reads

$$X^2(\theta,T) = X_0^2(T) + X_2^2(T)\theta^2 + \mathscr{O}(\theta^3) \tag{3.38}$$

where

$$X_0^2(T) = \frac{(E_C(T) - E_X(T)) + \sqrt{(E_C(T) - E_X(T))^2 + (2\hbar\Omega_R)^2}}{2\sqrt{(E_C(T) - E_X(T))^2 + (2\hbar\Omega_R)^2}} \tag{3.39}$$

$$X_2^2(T) = \left(\frac{\pi\hbar^2 c k_0 \Omega_R}{n}\right)^2 \frac{1}{E_C(T)} \left((E_C(T) - E_X(T))^2 + (2\hbar\Omega_R)^2\right)^{-\frac{3}{2}} \tag{3.40}$$

where $E_X(T)$ and $E_C(T)$ are respectively the bare exciton and bare cavity photon energy at zero momentum as a function of T

$$\begin{aligned} E_X(T) &= E_X(0) - f_{exc}(T) \\ E_C(T) &= E_C(0) - f_{cav}(T) \end{aligned} \tag{3.41}$$

and $Rs = 2\hbar\Omega_R \approx 3.3\ meV$ is the Rabi splitting. If we call $\delta_0 = E_C(0) - E_X(0) \approx -7.1\ meV$, then $(E_C(T) - E_X(T)) = \delta_0 + (f_{exc}(T) - f_{cav}(T))$, since $\delta_0^2, Rs^2 \gg (f_{exc}(T) - f_{cav}(T))$ and Rs is approximatively constant in the whole temperature range of interest, the expressions (3.39)-(3.40) can be greatly simplified and written in terms of the functions (3.32)-(3.33) and of the effective photonic hopfield coefficient C_{eff}^2 by means of a Taylor expansion in powers of $\Gamma(T) = (f_{exc}(T) - f_{cav}(T))$. For instance if we define the parameter

$$\Lambda = \frac{\delta_0}{\sqrt{\delta_0^2 + Rs^2}} \tag{3.42}$$

the terms in equation (3.39)-(3.40) reads

$$\sqrt{(E_C(T) - E_X(T))^2 + (2\hbar\Omega_R)^2} \approx \frac{\delta_0}{\Lambda} + \Lambda\Gamma(T) \tag{3.43}$$

$$\left[(E_C(T) - E_X(T))^2 + (2\hbar\Omega_R)^2\right]^{3/2} \approx \left(\frac{\delta_0}{\Lambda}\right)^3 + \frac{3\delta_0^2}{\Lambda}\Gamma(T) \tag{3.44}$$

By substitution and truncation of higher orders is $\Gamma(T)$ the two coefficient of the excitonic Hopfield coefficient (3.38) becomes

$$X_0^2(T) = \frac{1}{2} + \frac{1}{2}\frac{\delta_0 + \Gamma(T)}{\delta_0/\Lambda + \Lambda\Gamma(T)} + \mathcal{O}(\Gamma^2) \tag{3.45}$$

$$X_2^2(T) = \chi\left[\left(\frac{\delta_0}{\Lambda}\right)^3 + \frac{3\delta_0^2}{\Lambda\Gamma(T)}\right]^{-1} + \mathcal{O}(\Gamma^2) \tag{3.46}$$

where χ incorporates all the multiplicative constant terms. The last quantity we need to describe is the pillar grondstate to lower polariton band detuning which reads

$$\delta_{GS-LP}(T) = E_{GS}(T) - E_{LP}(T) \tag{3.47}$$

the ground state energy as a function of temperature reads in terms of (3.34)

$$E_{GS}(T) = E_{GS}(0) - f_{GS}(T) \tag{3.48}$$

then we have the lower polariton band at zero momentum

$$E_LP(T) = \frac{1}{2}(E_X(T) + E_C(T)) - \frac{1}{2}\sqrt{(E_C(T) - E_X(T))^2 + Rs^2} \tag{3.49}$$

and using the same Taylor expansion in terms of $\Gamma(T)$, these last term can be simplified and the pillar grondstate to lower polariton band detuning finally provides

$$\delta_{GS-LP}(T) = \delta_{GS-LP}(0) + \frac{1}{2}(2C_{eff}^2 + \Lambda - 1)\Gamma(T) \tag{3.50}$$

The pillar excitonic hopfield coefficient can be obtained by substitution of the equations (3.37)-(3.45)-(3.46)-(3.50) in (3.38). The final result is

$$X_{GS}^2(T) = \frac{1}{2}\left(1 + \frac{\Lambda(\delta_0 + \Gamma(T))}{\delta_0 + \Lambda^2\Gamma(T)}\right) + \frac{\chi\Lambda^3}{\eta\delta_0^2}\left(\frac{\delta_{GS_LP}(0) + \frac{1}{2}(2C_{eff}^2 + \Lambda - 1)\Gamma(T)}{\delta_0 + 3\Gamma(T)\Lambda^2}\right) \tag{3.51}$$

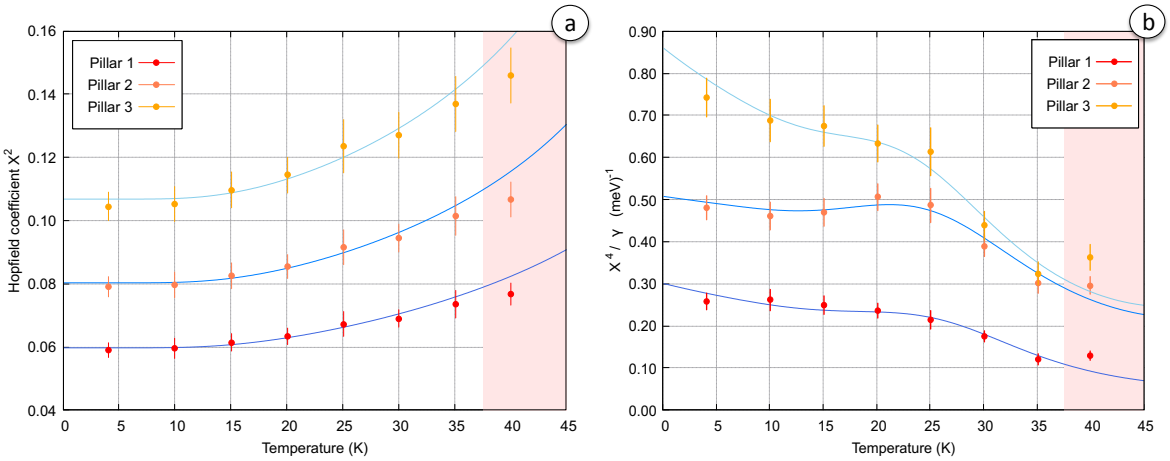

Figure 3.10: (a) Pillar ground state polariton excitonic fraction as a function of the sample temperature. The solid lines are the best fits provided by the model function (3.51). (b)-Temperature dependent factor in the effective Kerr nonlinearity of the pillar stucture, the errors were derived by simple propagation for independent variable from the $X^2_{GS}(T)$ errors, since the experimental uncertainty on the linewidth can be safely neglected. The solid lines are simply the ratio between the squared fitting function of panel (a) and the best fits of (3.35).

Once the parameters defining $\Gamma(T)$ are fixed as the value of C^2_{eff} the function is completely specified. In our case since some of the parameters included in χ and η slightly change with temperature (it depends on higher orders of $\Gamma(T)$), we defined as only free parameter the multiplicative constant $\Omega^* = \chi/\eta$.

In figure 3.10-(a) we plot the dependence of the excitonic Hopfield coefficient which we derived from the experiments along with the best fit of (3.51) for the three pillars. The experimental errorbars are calculated by propagation of the planar cavity best fit parameter uncertainties as prescribed by (3.14), notice that the error on the pillar emission peak position can be safely neglected, being one order of magnitude smaller than the other contributions. We get

$$\Omega^*_1 = (7.18 \pm 0.17)\, meV^2 \quad \Omega^*_2 = (8.89 \pm 0.34)\, meV^2 \quad \Omega^*_3 = (11.0 \pm 0.78)\, meV^2$$

the fit again is good within $(0 < T < 35)K$ as inheritance of the fit quality of $f_{GS}(T)$ above this range of temperatures. In figure 3.10-(b) we finally get the desired answer to our question:

♦ *Yes, the nonlinearity can be tuned by controlling the sample temperature* ♦

We plotted the temperature dependent part of the effective Kerr nonlinearity (3.24), namely $X^4_{GS}(T)/\gamma(T)$, as a function of temperature: for the first two pillars in the region $(0 < T < 25)K$ the nonlinearity has a plateau and remains almost constant, whereas for the third pillar the nonlinearity decreases in a quasi-linear fashion. All the three pillars show a fast drop in the

nonlineartity above 25 K ,this can be ascribed to the exponential term which starts to dominate the linewidth broadening due to the exciton-optical phonon coupling and the enhanced mobility of defects. Around 20 K, pillar two suggests that is even possible to enhance the nonlinearity with temperature, however we stress that the enhancement is within the experimental uncertainty, it is anyhow clear that the dependence of the nonlinearity with temperature depends also on the pillar ground state to lower cavity polariton detuning -so on the pillar size- and it probably depends also on the initial bare exciton to cavity-photon detuning demanding for systematic futher investigations.

We also proposed a semi-empirical but comprehensive model to understand the interplay between the different contributions to the temperature-dependent effective Kerr nonlinearity in a pillar structure, which has the advantage to be analytic. In our tractation we calculated the different reshift contributions by fitting our experimental data, but nothing prevents the calculation of the different coefficients on the basis of microscopic ab initio calculations. Moreover the model can be easily refined to include second order effects on the diffrent energy shift functions f_{exc}, f_{cav} and f_{GS}. The ability to define these functions in a general form recounting also for the pillar size dependence and initial bare exciton-cavity detuning would be a challenging task turning this semi-empirical model in a predictive tool paving the way to an unprecedented control over the system nonlinearity.

Even in the case the nonlinearity cannot be enhanced by means of temperature, this results is intriguing for those who want to address a long lived theoretical prediction for photonic systems which has still never been experimentally observed with Polariton systems: the Unconventional Photon Blockade effect [26]-[27]. This effect should take place in coupled photonic resonators even in presence of a weak nonlinearity $U \ll \gamma$ if a precise ratio between U and the coupling is matched. The smoking gun of a photon blockade effect is a strongly antibunched photon emission, however the magnitude of this effect abruptly decreases if the matching of nonlinearity and coupling is not exact. Since temperature can be easily tuned with a $0.01K$ or better accuracy, this reflects in the ability to control the nonlinearity within a part over 10^3 or better: our results then strongly encourages the search of this intriguing but elusive effect. These results will be the subject of a forthcoming publication.

CHAPTER 4

Two Coupled Microcavities - Hopping and Nonlinearity

In this chapter we address the linear and nonlinear physics of two coupled polariton microcavities. This system represents the essence of every driven-dissipative Bose-Hubbard inspired Hamiltonian since it includes all the fundamental ingredients of the model: hopping, on-site nonlinearity, driving and losses.

When two pillars have a finite overlap, the junction provides an effective tunnel-like coupling term: in the first section we will see how this coupling constant can be tuned by varying the center to center distance between the two pillars. In close analogy with a quantum particle in a double well, the first two eigenstates of the coupled pillars show the so called *Bonding* and *Antibonding* character, we experimentally measure these features and we characterize the linear response spectrum of the dimer.

The second section is devoted to the study of the nonlinear effects arising in the coupled cavities. Depending on the pump detuning the sistem behaves as an optical limiter and shows bi and multistabity. We experiementally test both the optical limiter and the bistable regime, while we refear to [25] for the multistability. The steady state of the system is described within mean field approximation by a set of coupled nonlinear equations which can be deduced from the driven-dissipative Gross-Pitaevsky equation [58], we present the model and compare the simulations with the experimental results.

The third section presents a novel result: if the stability of the steady state is investigated trough the Bogoliubov spectrum of the small fluctuations around the stationary solution a power dependent parametric instability can be identified and results in a self pulsing dynamics of the

steady state. Optical parametric oscillation is a well-known nonlinear phenomenon which was already demonstrated to happen in planar microcavities [18]-[19]-[59] and in single micropillars [20]-[21]. We report the first experimental observation for two coupled cavities. This result is intersting in the perspective of generating entangled polariton pairs as result of the parametric scattering process.

I would like to aknowledge the fruitful collaboration with Said K.R. Rodriguez, a mentor and a friend who teached me all the measurement techniques i used throughout this manuscript, shared his know-how and patiently helped me to face the unavoidable experimental issues i encountered during my internship in C2N. As well i would like to thank Alberto Amo and Jacqueline Bloch for their constant advice, positive criticism and fundamental contribution to the design and discussion of the experiments.

The driven dissipative Bose-Hubbard model can be schematized as in figure 4.1, we introduced in the picture some general notation which will be used hereafter: the coupling strenght J is proportional to the "hopping" rate to nearest neighbour sites, the on-site nonlinear term U has the form (3.24), γ is the characteristic lifetime of the microcavity polariton and $F(t)$ is the coherent laser driving.

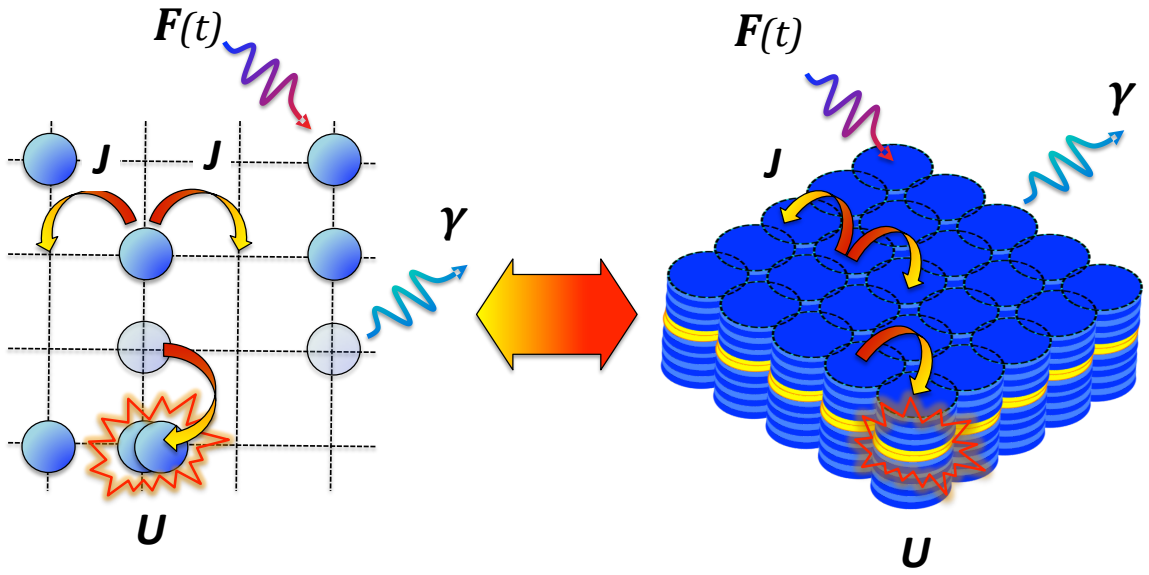

Figure 4.1: Schematic of the Driven Dissipative Bose-Hubbard Model (DDBHM) on a lattice with coordination 4. An analog simulator of the DDBHM Hamiltonian based on coupled polariton microcavities.

4.1 Coupled Microcavities-linear regime

Imagine to take two circular micropillars as the one described in section 3.2 and let them overlap, so that the structure section looks like the black profile in figure 4.2-(b). Let us neglect for the moment the losses, the driving term and the nonlinearity in the Gross-Pitaevsky equation (GPE) (1.4.3) which the polariton eigenfunctions obey: this physically means we are looking at the steady state of a weakly driven coupled pillar structure. The GPE reduces to a time independent Schrödinger equation

$$\left[\hbar\omega_0 - \frac{\hbar^2\nabla^2}{2m^*} + V_{ext}(x,y)\right]\psi(x,y) = E\,\psi(x,y) \tag{4.1}$$

where m^* is the polariton effective mass in parabolic band approximation. Unlike the single pillar case $V_{ext}(x,y)$ shows no continuous symmetry therfore $\psi(x,y)$ cannot be factorized and the eigenfunctions have anymore a closed analytical solution, a finite element method can be employed for this calculation as we will see later.

We would firstly like to draw a parallel between the coupled pillars and the Bose-Hubbard model. As demonstrated in section 3.2 the eigenmodes of a pillar blueshift proportionally to L^{-2} if L is the lateral dimension of the pillar. If we call CC' the center-to-center distance of the two pillars, R the pillar radius and we label with x the coordinate along the dimer axis centered at $CC'/2$ from both the pillar centers, the width L of the structure as a function of x reads

$$L(x) = 2R\sqrt{1-\left(\frac{|x|}{R} - \frac{CC'}{2}\right)^2} \tag{4.2}$$

As long as $L(0) < (CC' + 2R)$ the effect of confinement along the dimer axis is much weaker than the lateral one and blueshift reads

$$\Delta E(x) = \frac{\pi^2\hbar^2}{2m^*L(x)^2} \tag{4.3}$$

Within this coarse approximation the confinement along the dimer axis can be neglected and we can marginalize the transverse coordinate which enters the Hamiltonian only trough its effect on the x-dependent blueshift

$$\hat{H}\psi(x,y) \approx \left[\hbar\omega_0 - \frac{\hbar^2\nabla^2}{2m^*} + \Delta E(x)\right]\psi(x) = E\,\psi(x) \tag{4.4}$$

The problem reduces to the solution of a one dimensional time-independent Schrödinger equation where $\Delta E(x)$ plays the role of an effective external potential. In figure 4.2-(a) we show the function $\Delta E(x)$ for different CC' values, notice that the blueshift has a form alonf the dimer axis which resembles a double well potential.

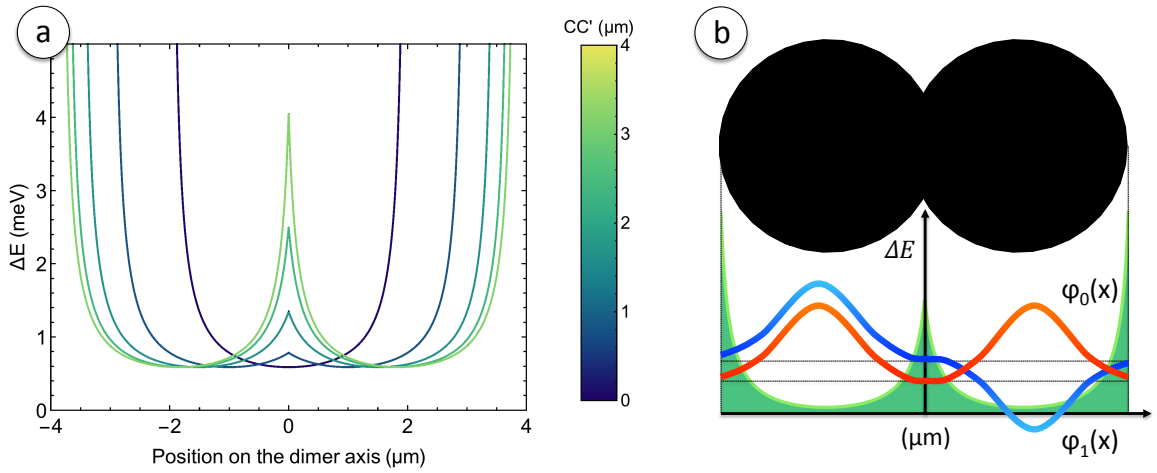

Figure 4.2: (a)-Blueshift due to the lateral confinement along the dimer axis calculated with equation (4.3) for diffrent values of the center to center distance. (b)-Top vision of the coupled pillar section for $CC'/2R = 7/8$, the associated local blueshift due to the lateral confinement is sheded in green and we show the first two eigenfunction calculated for a potential in the form prescibed by equation(4.3), notice the even-(odd) symmetry of φ_0-(φ_1).

Again equation (4.4) has no analytic solutions however, as 4.2-(b) shows, the first two eigenfunctions have almost the same profile but whereas the ground state is even respect to the parity operator the first exited state is odd. Provided that the energy separation between the grounstate and the first excited state $\Delta\varepsilon_{GS,1}$ is much smaller than $\Delta\varepsilon_{GS,2}$, a two-mode approximation is legit and allows to neglect the influence of the higher excited states in the system dynamics. Within this assumption the so-called *left* and *right* bosonic operators can be introduced:

$$\begin{aligned}\varphi_L(x) &= \frac{1}{\sqrt{2}}(\varphi_0(x)+\varphi_1(x)) \\ \varphi_R(x) &= \frac{1}{\sqrt{2}}(\varphi_0(x)-\varphi_1(x))\end{aligned} \tag{4.5}$$

Since $\varphi_0 \approx \varphi_1$ for $x<0$ and $\varphi_0 \approx -\varphi_1$ for $x>0$ this means that in this new basis φ_L is almost null in the right cavity and vice versa: the two-mode bosonic field operator reads

$$\varphi(x) = a_L\varphi_L(x) + a_R\varphi_R(x) \tag{4.6}$$

were a_L, a_R are the destruction operators acting on the left or on the right side of the well. Inserting this two-mode approximation in the GPE equation we end with

$$H = \sum_{i=L,R} \varepsilon_i \, a_i^\dagger a_i - J_{LR} \, a_L^\dagger a_R - J_{RL} \, a_R^\dagger a_L \tag{4.7}$$

which is the two-site Bose-Hubbard hamiltonian in absence of nonlinear terms (U=0). If the two cavities are equal $\varepsilon_L = \varepsilon_R = \varepsilon$ and $J_{LR} = J_{RL} = J$ and

$$H = \varepsilon(N_L + N_R) - J \, (a_L^\dagger a_R - a_R^\dagger a_L) \tag{4.8}$$

this is the second quantization hamiltonian of two coupled harmonic oscillators. Notice that if ε_0 and ε_1 are respectively the ground state and the first excited state eigenenergies then

$$\begin{aligned} \varepsilon - \frac{\Delta\varepsilon_{GS,1}}{2} &= \varepsilon_0 \\ \varepsilon + \frac{\Delta\varepsilon_{GS,1}}{2} &= \varepsilon_1 \end{aligned} \tag{4.9}$$

The quantity $\Delta\varepsilon_{GS,1}/2$ is often labeled with the letter J and is proportional to the tunneling rate between the left and right well. Since Driving, losses and the nonlinear term affects separately the left and right field amplitudes they can be easily derived by substituting the ralation (4.6) in the polariton field for the actions (1.118)-(1.120)-(1.115) we derived in section 1.4.3, and by taking the variations respect to $\varphi_L^\dagger(x)$ and $\varphi_R^\dagger(x)$. The complete mean field equations describing the polariton field in the two coupled cavities under a coherent drive reads

$$\begin{aligned} \left(\varepsilon_L - \hbar\omega - i\frac{\gamma_L}{2}\right) \psi_L + U|\psi_L|^2\psi_L - J\psi_R + F_L = 0 \\ \left(\varepsilon_R - \hbar\omega - i\frac{\gamma_R}{2}\right) \psi_R + U|\psi_R|^2\psi_R - J\psi_L + F_R = 0 \end{aligned} \tag{4.10}$$

were we used the coherent drive ansatz (3.21) as in section 3.3. Notice that since these equations were derived within mean field approximation the quantities $\psi_{R,L}$ are $\mathbb{C}$ numbers and not scalar field operators and physically correspond to the average polariton field amplitude. So we showed that the hamiltonian describing the polariton field in coupled microcavities can be mapped in a driven-dissipative Bose-Hubbard one.

In figure 4.3 we show a finite element simulation of the first ten eigenmodes of the coupled pillar along with the measured energy resolved PL of the structure. In the finite element simulation if $\mathscr{D}$ is the set defining the coupled pillars section, $V(x,y) = 0$ if $(x,y) \in \mathscr{D}$ and $V(x,y) = \infty$ otherwise. As already discussed in section 3.2 this is a good approximation thanks to the huge refractive index mismatch between the semiconductor and air resulting in a step-like effective potential for the photonic component of the exciton because of total internal reflection.

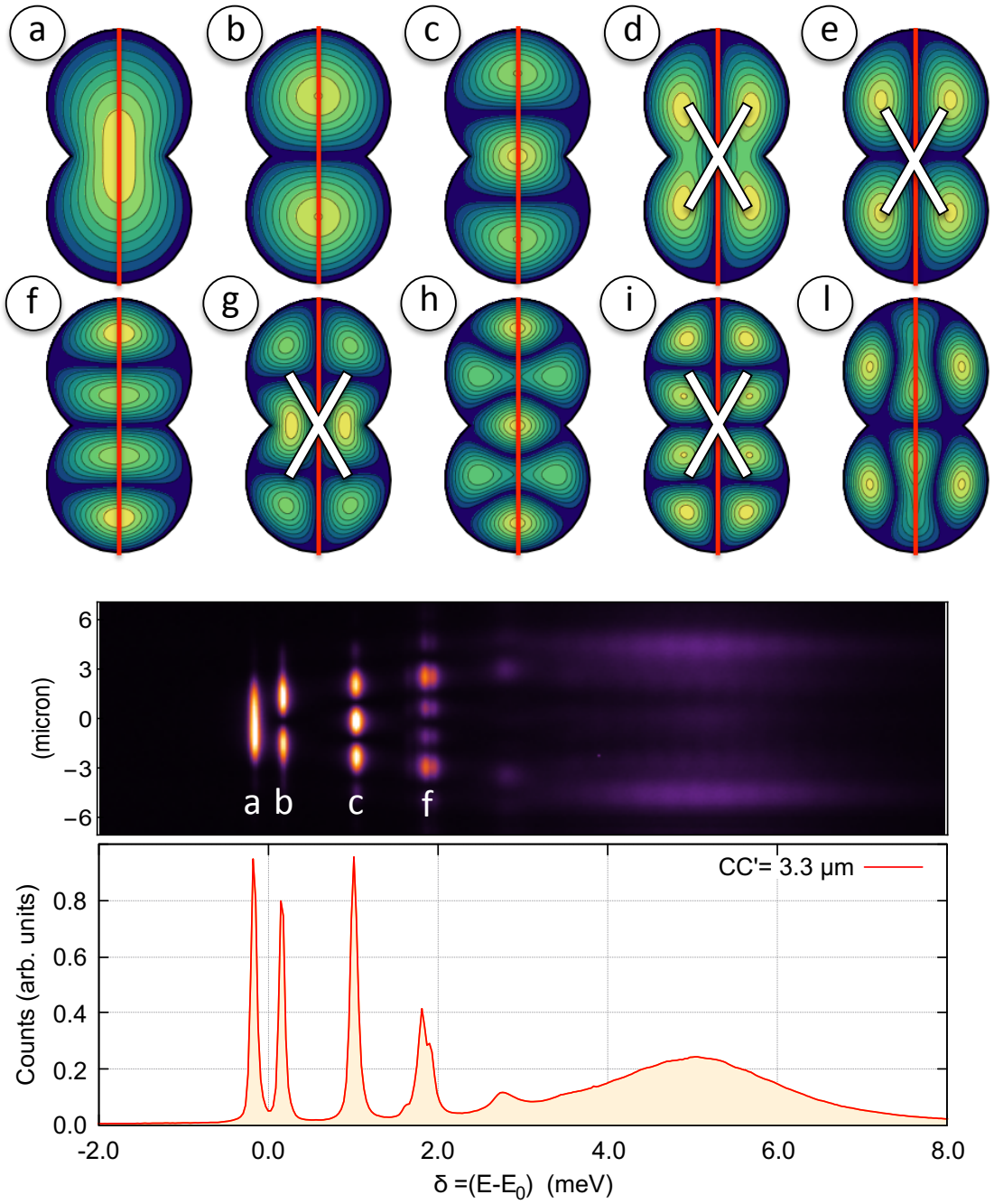

Figure 4.3: (a) to (l): Finite element simulation of the first ten eigenmodes of two coupled pillars, the red line represents the spectrometer slit position respect to the real space image of the dimer molecule luminescence. Some of the modes -the ones marked with a white cross- appear dark in our experiment due to the slit position. In the bottom of the panel we plot the experimental energy and space resolved emission of the coupled pillars: the simulations are in good agreement with the measured mode profiles, $\delta = (E - E_0)$ is the detuning respect to the single pillar ground state energy E_0. In mode (f) the TE-TM splitting inherited by the dielectric mirrors can be clearly resolved, while in the other modes is within to the linewidth, indeed higher modes are more sensitive to these effects in analogy with the fine structure effects in the atomic orbitals, as discussed in section 3.2.

The time independent Scrödinger equation (4.1) for this external potential becomes equivalent to the solution of the Helmoltz equation with the Dirichlet condition $\psi(x,y) = 0$ if $(x,y) \in \partial\mathscr{D}$ and $\partial\mathscr{D}$ denotes the boundary of $\mathscr{D}$. We wrote a Mathematica script to numerically calculate the eigenmodes of the Helmoltz equation above defined: the first ten modes are plotted in figure 4.3-(a) to (l), the pillar diameter was set to $R = 2.0\ \mu m$ and $CC' = 3.3\ \mu m$, the finite element mesh based on a constrained Delaunay triangulation had 10^3 points. The polariton effective mass was set to $m^* \sim 4 \cdot 10^{-5} m_e$ extrapolated from the fit of figure 3.4-(b).

Moving in motif (D-B)-(5) we investigated a structure having the same nominal dimensions of the simulation, the structure PL was measured in transmission geometry adopting the setup configuration illustrated in section 2.2-(PHOTOLUMINESCENCE). The pump power was set low enough to neglect all the nonlinear contributions. We report the energy and space resolved emission in the bottom part of figure 4.3 along with its projection. The abscissa is the detuning $\delta = E - E_0$ respect to the ground state energy E_0 of the single pillar, which lays in between the ground state and the first excited state. This fact can be understood on the basis of our analogy between pillars and atoms. Indeed if we take the grounstate orbital $1s$ of an hydrogen atom, and we put two of them close to each other the orbital overlap results in a hybridization of the $1s$ orbitals and first two eigenstates have a symmetric and antisymmetric wavefunction. The symmetric "*bonding*" orbital corresponds to the grounstate and if E_0 is the H ion $1s$ energy, the bonding energy is $E_B = E_0 - \Delta E$ if ΔE is the H_2 molecule binding energy. On the contrary the antibonding mode is antisymmetric respect to the H_2 molecule center of mass, correspondingly the electrons wavefunction has a node: this cannot be a bound state since the electron clouds of the two hydrogen atoms are separated and $E_{AB} > E_0$. If now we look at the equations (4.9) we can think φ_0 to be the H_2 bonding mode and φ_1 to the antibonding mode.

This analogy is supported by the experiment: if we look at the first two measured eigenmode profiles a respectively symmetric and antisymmetric character is evident. This can also be understood in terms of classical CHOs as discussed in section 1.1: the first two eigenmodes of the system correspond respectively to the in-phase (symmetric) and π-dephased (antisymmetric) vibration of the two oscillators. The simulated profiles of the higher modes are in good agreement with the experimental results, the experiment also legitimates the two-mode approximation employed in the derivation of the DDBH Hamiltonian, since $\gamma_{E_2} + \gamma_{E_1} \ll \Delta E_{2,1}$.

The peak in the PL spectrum corresponding to the third eigenmode is splitted (fig. 4.3), suggesting another important feature characterizing the coupled pillars: due to the absence of rotational symmetry in the structure the TE and TM modes are anymore degenerate in the coupled pillar structures as inheritance of the dielectic nature of the DBRs. Back in section 3.2 we pointed as some pillar structures showed a lifted degeneracy of the energy levels with $m \neq 0$ ascribable to the slight ellipticity of the pillar. Here $\mathscr{D}$ is symmetric only under reflections along the dimer

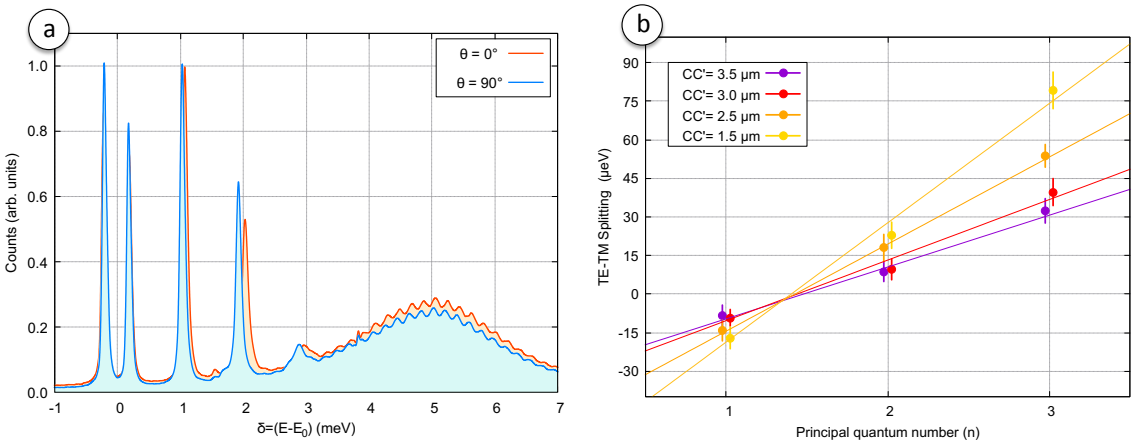

Figure 4.4: (a)-Energy and Polarization resolved measurement of the PL emission, the abscissa is rescaled by subtracting the ground state energy of a single pillar with nominal radius matching the coupled pillar ones. (b) TE-TM mode splitting as a function of the principal quantum number and of the center to center spacing, and approximatively linear dependence of the splitting can be inferred for the lower modes.

axis, thus the TE-TM degeneracy of the energy levels which can be observed in structures with a rotational symmetry is lost. If the laser is polarized along the dimer axis just one mode among the TE and TM couples to the coherent pump and the other is dark, this is fundamental in the resonant transmission experiments in order to work with a proper two level system. On the contrary in PL measurements, since the hot electrons created by the blue detuned pump relax and recombinate before populating all the allowed polariton states, they keep no information on the pump polarization and both the TE and TM modes can be appreciated. If the fourth eigenmode shows a splitting (fig. 4.3) also the other modes must be splitted, but we cannot resolve the two contributions because they are smaller than the linewidth.

In order to resolve the two contribution a polarizer -(P1) in fig. 2.5- was included in the collection line. If $\theta = 0^o$ denotes the position of the polarizer axis parallel to the dimer axis we collected the PL spectrum for four diffrent coupled pillars with $R = 2.0\mu m$ and different center-to-center spacings both at $\theta_{\|} = 0^o$ and $\theta_{\perp} = 90^o$, allowing to detect the separately the luminescence of the TE and TM modes. We report the measured PL spectra for a dimer with $CC' = 3.0\mu m$ in figure 4.4-(a). The TE-TM splitting can be calculated if the centroid of the of the $\theta_{\|}$ and $\theta_{\perp}$ peaks is known: we defined $\delta_{Sp}(n) = E_n(\theta_{\|}) - E_n(\theta_{\perp})$ as a function of the principal quantum number n. The results is plotted in figure 4.4-(b), a typical value for the TE-TM splitting is roughly $(10 \div 20)\mu eV$ for the ground state and grows linearly with the principal quantum number. We also notice that the splitting grows as the center-to-center spacing diminishes affecting the slope of the linear dependence of $\delta_{Sp}(n)$ on the principal quantum number. This may be understood because for CC' values close to $2R$ the overlap with the second pillar

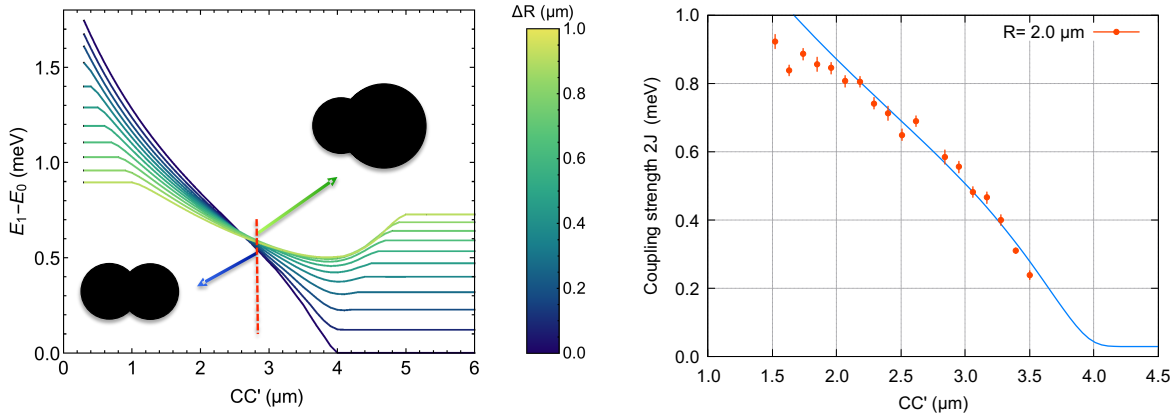

Figure 4.5: (a)-Simulated value of the coupling streghth $2J = E_1 - E_0$ as a function of the center-to-center distance and of the difference between the radii of the two pillars constituting the dimer ΔR. (b)-Measured coupling strength $2J$ as a function of the center-to-center distance CC'; the solid blue line is the simulation for two coupled pillars with $\Delta R = 0.04\mu m$ and $m^* = 3.74 \cdot 10^{-5} m_e$ which is in good agreement (within 5%) with the polariton effective mass we deduced in section 3.2.

is small and the cylindrical symmetry of the pillar boundary is slightly perturbed but the magnitude of the perturbation increase rapidly with CC'^{-1}.

Tough crude, the assumption adopted in (4.4), allows to comprehend another interesting feature of coupled pillar cavities. Indeed if we look at figure 4.2-(a) the blueshift $\Delta E(x)$ shows a relative maximum in $x = 0$ which strongly depends on CC' and acts as a potential barrier between the two sites: since the area of the barrier is somehow inversely proportional to the coupling strength J, this suggests the possibility of changing the coupling constant by tuning the center-to-center distance of the two pillars [60].

In order to turn this consideration in something quantitative we both addressed the problem numerically and with a set of measurements. In figure 4.5-(a) we calculated the first two eigenvalues of the Helmholtz equation with the Dirichlet condition $\psi(x,y) = 0 \ \ \forall (x,y) \in \partial\mathscr{D}$ as a function of CC' and ΔR, the diffrence between the two pillar's radii. We studied the dependence in ΔR because the fabrication process may be imperfect, resulting in an asymmetric pillar size, notice that for $CC' > R_1 + R_2$ the quantity $E_1 - E_0$ can't be anymore identified with the coupling strength $2J$ but simply represent the diffrence between the ground state energy of the two pillars. The pillar diameters were $R_1 = 2\ \mu m$ and $R_2 = \Delta R + R_1$, the polariton effective mass was set to $4 \cdot 10^{-5} m_e$. This simulation confirms the qualitative consideration discussed in the above paragraph: the coupling strength increses as CC' becomes smaller, and if $\Delta R \ll R$ the dependence is quasi-linear in CC'. In figure 4.5-(b) we report the measured coupling strength: a double Voigt profile was employed to fit the bonding and antiboning mode profiles of some of the (D-B)-(5) coupled micropillars. The spectra were recorded again by energy resolved measurements of the

dimers' photoluminescence; the collection line polarizer angle was set to $\theta = \theta_{\|}$. If $\overline{E}_0$ and $\overline{E}_1$ were respectively the ground and first excited state peak centroids, the coupling strength was $2J = \overline{E}_1 - \overline{E}_0$ according to equation (4.9); the data point errors were calculated propagating the centroid uncertainties as prescribed by equation (3.14). The solid blue line in 4.5-(b) is somehow a best fit of the simulated $2J(CC')$ relation: we calculated $4 \cdot 10^2$ curves for different values of m^* and ΔR and we found the one minimizing the χ^2. From this postselection

$$\Delta R \approx 0.04\ \mu m \qquad m^* \approx 3.74 \cdot 10^{-5} m_e$$

The value of ΔR is compatible with the etching technique resolution and m^* is within 5% of the value we extrapolated in section 3.2. The best fit $2J(CC')$ curve reproduces quite well the experiental results down to $CC' \sim 2\ \mu m$ however a systematic deviation for lower values of CC' is evident: the theoretical prediction overestimates the experimental data. This can be understood if we recall that the identification of the coupling strength $2J$ with $\overline{E}_1 - \overline{E}_0$ is justified only within the two-level approximation, however for small values of CC' since $\Delta E_{0,1} \sim \Delta E_{1,2}$ the higher modes start to play a role and the above identification is anymore good.

The remarkable result of this section is that by tuning the center-to-center distance of two pillars we can control the coupling strenght between the two cavities. As discussed in section 3.1-3.2-3.3 we can also control the on-site nonlinearity by etching the pillar structures in a part of the sample with a higher or lower excitonic fraction, by changing the pillar radius or finely tuning the sample temperature. Moreover the pillar level structure can be engineered by controlling the size and aspect ratio of the structure. This complete control over the coupled cavity network parameters is the essential strength of the exciton-polariton framework.

4.2 Coupled microcavities-Nonlinear regime

In the sections 1.4.3-3.2-3.3 we already discussed the origin of the polariton Kerr nonlinearity and we demonstrated how it can be tuned, however any nonlinear effect was up to here investigated: on the contrary we always worked in a low power regime in order to safely neglect the nonlinear contribution in the driven-dissipative GPE. Indeed working with linear equations in most of the cases results in a tractable problem with closed analytical solutions, whereas if a nonlinear term is summed up in the equations many mathematical tools we are used to work with cease to be exploitable, i.e. the superposition principle, the methods of linear algebra, many uniqueness theorems. Actually the nonlinearity of Einstein equations is one of the fundamental obstacles to the quantization of Gravity.

In this section address some of the exquisitely nonlinear properties of our coupled nonlinear cavities: the optical limiter phenomenon, and the steady state bistability. In nonlinear phenomena the physics is sometimes counterintuitive, as suggested by Fermi a numeric simulation has the role of leading the physicist where complexity overwhelms intuition. To this aim let us first re-write the equations we derived within a two-level mean-field approximation for the polariton field in the coupled cavities

$$\begin{aligned}\left(\varepsilon_L - i\frac{\gamma_L}{2}\right)\psi_L(t) + U|\psi_L(t)|^2\psi_L(t) - J\psi_R(t) + F_L(t) = i\hbar\partial_t\psi_L(t)\\ \left(\varepsilon_R - i\frac{\gamma_R}{2}\right)\psi_R(t) + U|\psi_R(t)|^2\psi_R(t) - J\psi_L(t) + F_R(t) = i\hbar\partial_t\psi_R(t)\end{aligned} \tag{4.11}$$

Which is the general form of (4.10) without casting the coherent drive ansatz. These equations are essentially nonlinear-Schrodinger equation describing the time dynamics of the two-mode field amplitude and was firstly adopted by Milburn and collaborators to describe the physics of a Josephson junction [61]. A recent work by D. Sarchi et al. [58] demonstrated how this model, tough simple ($\psi_{L,R}(t)$ are $\mathbb{C}$ numbers and not scalar fields), is able to reproduce the same results obtained with the driven-dissipative GPE for the polariton field $\psi_{L,R}(t,x,y)$.

In absence of pumping and nonlinearity $U = 0$ (i.e the pillars are excited by a weak femtosecond pulse with) the equations have the form of the time dependent Schödinger equation for the Non Hermitian Hamiltonian (NHH) (1.17) we introduced as quantum mapping of the classical Coupled Harmonic Oscillators (CHOs) in section 1.1. In analogy with the results of section 1.1 the the eigenvalues of the linear equations are

$$E_{+,-} = \frac{1}{2}(\hbar\omega_R + \hbar\omega_L) - \frac{1}{2}(\gamma_R + \gamma_L) \pm \frac{1}{2}\sqrt{[\hbar(\omega_L - \omega_R) - i(\gamma_L - \gamma_R)]^2 + 4J^2} \tag{4.12}$$

The linear coupling J splits the unperturbed levels $\hbar\omega_{L,R}$ into a pair of mixed eigenmodes

with energies $E_{+,-}$, for zero complex detuning ($\omega_L = \omega_R$ and $\gamma_L = \gamma_R$) the energy splitting is $E_+ - E_- = 2J$, and the two corresponding eigenmodes are the symmetric and antisymmetric modes introduced in the previous section 4.1 within the Bose-Hubbard model. Under a symmetric pump ($F_R = F_L$) only the symmetric mode ψ_- is excited, while for an atisymmetic pump ($F_R = -F_L$) only the antisymmetric ψ_+ mode is excited (see for the details section 1.1). To prepare the system in a superposition of ψ_+ and ψ_- we can arbitrarily set F_L or F_R equal to zero; hereafter $F_R = 0$.

This simple linear analysis is made richer by the presence of nonlinear terms: the effective Kerr nonlinearity of the micropillars introduces an intensity-dependent shift of the effective energy levels and can be responsible for dynamical instabilities. The standard definition of the eigenvalues becomes ill defined for nonlinear systems, therefore the effective eigenmodes $\psi_{+,-}$ if $U \neq 0$ can no longer be expected to be the symmetric and the antisymmetric ones, unless $F/\gamma \ll UN/\gamma$ (i.e the nonlinearity can be regarded as a small perturbation) and we denoted with $N_{L,R} = |\psi|^2$ the average occupation number of the left or right oscillator.

In the following experiments we are interested in the steady state amplitudes of $\psi_{L,R}$ under a coherent driving with amplitude $F_L = F$ and $F_R = 0$. If we plug again the ansatz (3.22) in (4.11), we find

$$\begin{aligned} \left(\varepsilon_L - \hbar\omega - i\frac{\gamma_L}{2}\right)\psi_L + U|\psi_L|^2\psi_L - J\psi_R + F = 0 \\ \left(\varepsilon_R - \hbar\omega - i\frac{\gamma_R}{2}\right)\psi_R + U|\psi_R|^2\psi_R - J\psi_L = 0 \end{aligned} \tag{4.13}$$

which reduces the coupled nonlinear ODEs (4.11) to a system of coupled nonlinear equations in $\psi_{R,L}$. We are interested on the solutions of these nonlinear equations as a function of the driving strength F and of the pump detuning $\delta_{LR} = \varepsilon_L - \hbar\omega$. Since we found an average standard deviation from the nominal size of the coupled pillar structure which is order of some tens of *nm* (section 4.1) and both the bare pillar ground state energy and linewidth variation can be safely neglected on such small scales (section 3.2), we can safely assume $\varepsilon_L = \varepsilon_R = \hbar\omega_0$ and $\gamma_L = \gamma_R = \gamma$.

Since we have two equations in two variables, once the detuning $\delta = \hbar(\omega_0 - \omega)$, the pump intensity F, the coupling strength J, the linewidth γ and the nonlinearity U are specified, the solutions can be uniquely determined; δ and F can be set externally but the values of J, γ, U needs to be measured.

Wheras J can be deduced with a simple PL mesurement, the spectrometer resolution does not allow a precise enough information on γ. The strategy is of course to move to a resonant

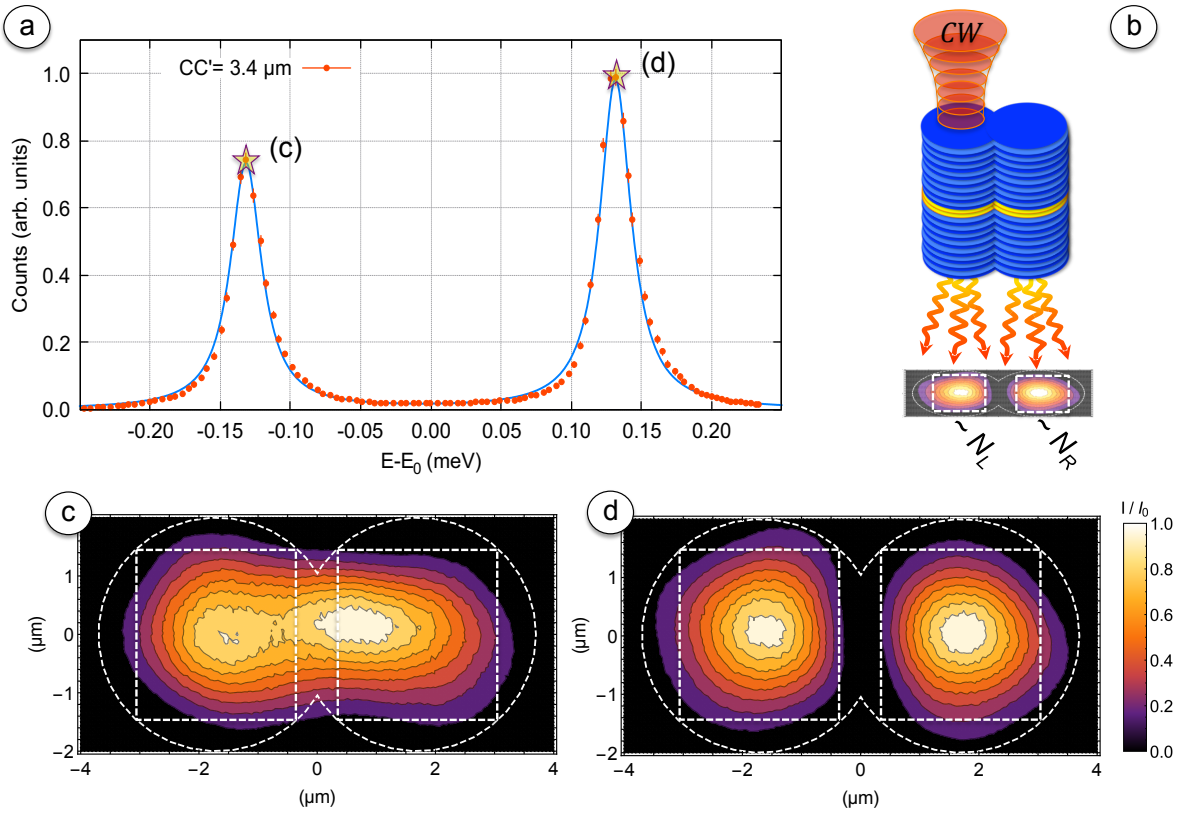

Figure 4.6: (a)-Coupled pillars in motif (D-B)-(5): resonant transmission as a function of the cavity ground state to pump detuning, the ordinate of the data points is proportional to the sum of $N_L + N_R$, the solid blue line is the best fit of equation (4.14). (b)-Sketch of the measurement; the left cavity is pumped and the real space emission is recorded for different pump detunings, a quantity proportional to the left and right populations $N_{L,R}$ can be calculated by integrating the real space emission within the dashed boundaries.(c)-(d) Imaging of the transmitted intensity for a pump frequency resonant with the ψ_+ and ψ_- modes marked with two stars in panel (a). The white dashed lines correspond to the boundaries $\partial\mathscr{D}$ of the dimer section and to the two integration ROI used for the calculation of $N_{L,R}$.

transmission experiement where our spectral resolution is limited only by the laser wavelength tuning accuracy $\Delta\lambda = 0.1pm$. If we weakly pump the system $NU \approx 0$ and the algebraic equation system (4.13) becomes equivalent to the equation modeling the driven dissipative CHOs of section 1.1. Since the loss rate γ is constant the transmitted intensity has to be proportional to the steady-state power dissipated spectrum of the two oscillators. Using an analogue of equation (1.9) to fit the experimental data we can therefore estimate γ and J.

In figure 4.6-(a) we show the resonant transmission $N_L + N_R$ of a test dimer as a function of the pump detuning respect $\hbar\omega_0$. The pump beam power was set lower than a microwatt and the beam polarization was set parallel to the dimer axis in order to inhibit the polarization splitting of the modes (see section 4.1). At least of a coefficient $N_{L,R}$ can be calculated by integrating

the intensity map within the boundaries defined by the two region of interest dashed in the panels (b), (c) and (d). The resonant transmission spectrum shows two marked resonances which correspond to the bonding and antibonding mode: we report the spatial resolved emission for a pump frequency resonant with the two peaks in figure 4.6-(c,d). The ground state of the coupled pillars shows a symmetric (bonding) profile and the first excited state shows as expected the characteristic antisymmetric (antibonding) profile in perfect agreement with the Bose-Hubbard model assumptions and with the numerical simulation of the previous section i.e. figure 4.3-(a,b).

We shall comment the height of the two peaks: in section 1.1 we have seen that for $F_1 = F$ and $F_2 = 0$ the steady state power dissipated spectrum (1.9) for two strongly coupled oscillators shows two peaks with a splitting proportional to the coupling sstrength Ω and equal heights. To understand the measured asymmetry we have to recall that the coupling of the laser pump with the $\psi_{+,-}$ modes is proportional to the overlap of the beam intensity profile with the mode profile: its clear looking at 4.6-(c,d) that the overlap of a gaussian beam centered on the left pillar is enhanced for the antibonding mode. A second artifact depends on the shape of the region of intrests we used to calculate $N_{L,R}$ which favours the antibonding-like profiles since it cuts the central region were the bonding mode shows a density maximum while the antibonding mode is zero due to the odd symmetry of the ψ_+ eigenfunction.

To model this effects we have just to allow a finite pump intensity F_R coherent with the left driving on the right pillar which enhances the symmetric mode coupling with the pump. Adding this new term and assuming $\omega_L = \omega_R = \omega_0$ and $\gamma_L = \gamma_R$ the stady state power dissipated spectrum can be calculated solving the inhomogeneus system of coupled equations (4.13) alike section 1.1, after some trivial algebra one gets

$$P(\delta, J, \gamma, F_L, F_R) = \frac{\gamma\left((F_L^2 + F_R^2)(\gamma^2 + \delta^2)\delta^2 - 4F_L F_R \delta^2 J^2 + (F_L^2 + F_R^2)\delta^4\right)}{\delta^4(\gamma^2 + \delta^2)^2 + 2\delta^2 J^4(\gamma^2 - \delta^2) + J^8} \tag{4.14}$$

where $\delta = \hbar(\omega_0 - \omega)$. We fitted this function to the measured transmission spectrum finally obtaining for the tested coupled pillar structure obtaining

$$J = (131.5 \pm 0.9)\ \mu eV \qquad \gamma = (27.1 \pm 1.2)\mu eV$$

the best fit is shown as a solid blue line in figure 4.6-(a) and smoothly fits the experimental data points, this again confirms the liceity of the simple model adopted to describe within mean field approximation the steady state of two coupled cavities.

The last constant to determine is the nonlinear coefficient $U \approx \Gamma^{XX}_{\rightrightarrows} X^4_{GS}$, ehere Γ^{XX} is specified by the exciton Bohr radius in the QW (see section 1.4.2) and X^2_{GS} is defined implicitly by the relation $X^2(k^*) = X^2_{GS}$ if k^* satisfies $\hbar\omega_{LP}(k^*) = \hbar\omega_0$ as discussed in section 3.3. Our pillar

belongs to motif (D-B)-(5) which lays in between the planar cavities in motifs (SSP)-(5) and (SSP)-(4). We therfore estrapolated the $\hbar\omega_{LP}(k)$ relation from a linear regression of the bare exciton to cavity photon detuning gradient measured in section 3.1, we can use the relations (3.38)-(3.36)-(3.37) derived in section 3.3 within parabolic band approximation to estimate X_{GS}^2. The nonlinear coeffient results for a dimer with $CC' = 3.4\ \mu m$ and $R = 2\ \mu m$

$$U \sim 0.03\ \mu eV \tag{4.15}$$

The relative uncertainty of this value is roughly $(15 \div 20)\%$, which can be derived by propagating for correlated variables the error on X_{GS}^4 which depends on the dispersion fit parameters errors trough (3.14) and correspond to the lower error bound. This purely statistical error is somehow an optimistic estimate since we considered only the dominat exciton-exciton Pauli scattering channel and we are neglecting density dependent effect which may play a role in small pillar structures when the pump intensity becomes high and the occupation number $N_{L,R}$ of one of the two cavities satisfies $(N_{L,R}\ a_B^2 \gtrsim R^2)$ where a_B is the $2D$ exciton bohr radius in the QW. Anyhow to have a better estimation of U the criticality to solve would be to refine the detection technique of the polariton dispersion.

We can finally compute the solutions of the set of algebraic coupled nonlinear equation (4.13). The solutions as a function of $\delta = \hbar(\omega_0 - \omega)$ and F can be computed by means of the continuation-homotopy numerical methods implemeted in Mathematica. We developed a complete suite to simulate the nonlinear steady state solution of (4.13), which can be easily extended to more complex structures (i.e. trimers and exagonal pillar rings). For simplicity we start by fixing $\delta \sim J + \gamma$, so we are pumping the left pillar at an energy two linewidths smaller than the bonding line, and we are interested in calculating the occupation numbers $N_{L,R}$ as a function of the pump power F. In absence of nonlinearity one would expect to abserve $N_{L,R}$ growing linearly with F^2, since the overlap of the beam line with the tails of the $\psi_{+,-}$ modes does not change with F. On the contrary in presence of a Kerr-type nonlinearity, since the pump is redshifted respect both the bonding and antibonding resonances and the effect of the nonlinear term is to blueshift the energy levels by an amount $\propto U N_{L,R}$ we expect the overlap of the pump line with the tails of the $\psi_{+,-}$ resonances to diminish as the onlinear eigenmodes are pushed away by the nonlinear blueshift. We would expect a sublinear dependence of $N_{L,R}$ in F^2, this is often called an optical limiter since the transmitted intensity saturates as the pump power grows.

We schematize this situation in figure 4.7-(e), in panel (a) we plot the measured total transmission $N_{Tot} = N_L + N_R$ in units of million of pixel counts (Mcts) as a function of the pump power incident on the left pillar, $\delta = J + \gamma$: the expected sublinear behaviour is evident as soon as $P \gtrsim 0.1\ mW$. In panel (d) we show the corresponding numerical simulation obtained from the solutions of the nonlinear equation set (4.13), the same qualitative behavior of the experiemnt

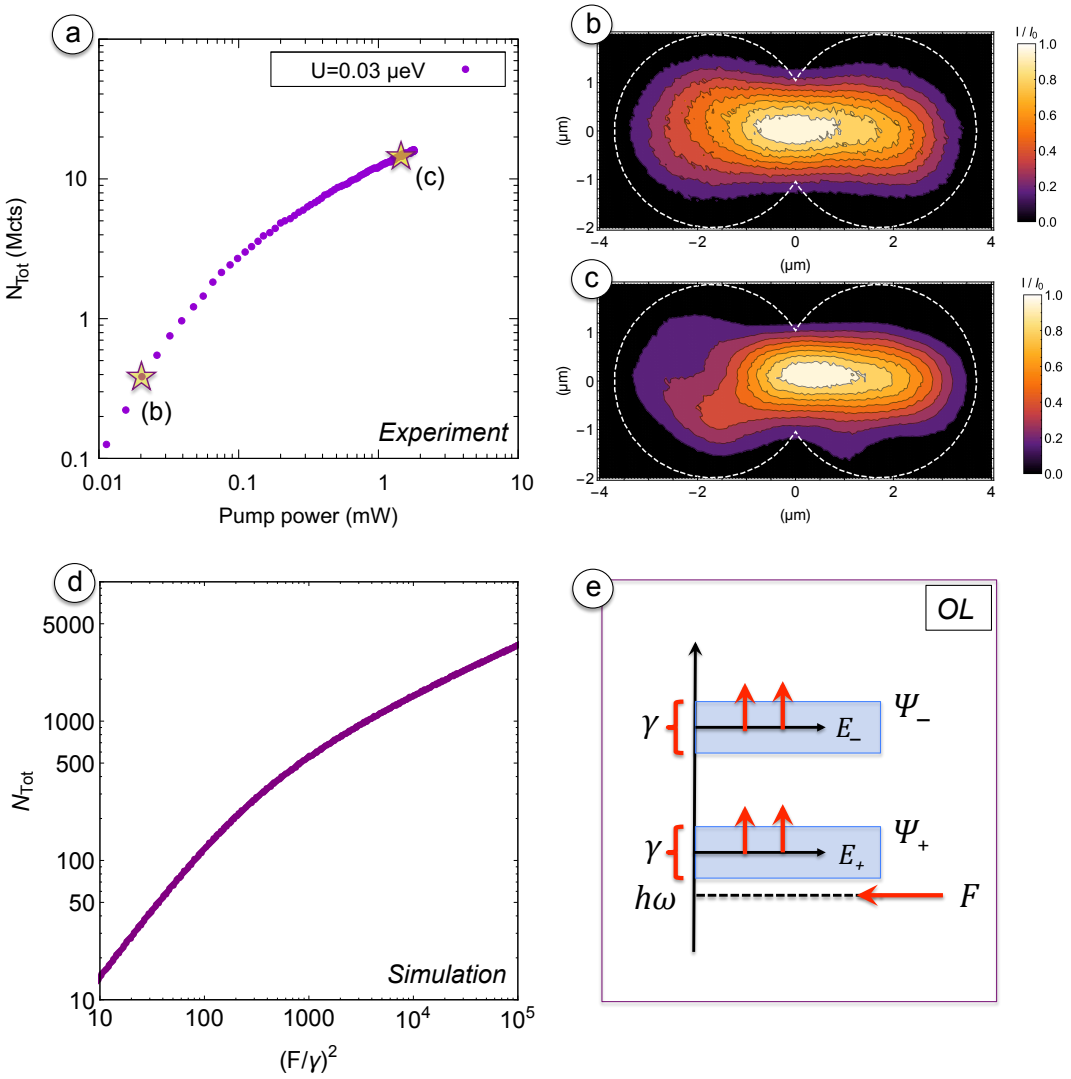

Figure 4.7: (a)-Measured total transmission $\propto N_L + N_R$ as a function of the incident pump power, $J \approx 131.5\ \mu eV$, $\gamma \approx 27.1\ \mu eV$, $U \sim 0.03\ \mu eV$ and $\delta = J + \gamma$. (b-c)-Imaging of the transmitted intensity for the two pump powers marked in panel (a) with two stars, a bonding-like profile can be appreciated in both the frames, the white dahed lines correspond to the coupled pillars section boundaries. (d)-Numeric solution of the set of nonlinear equations (4.13), we plot $N_L + N_R$ as a function of the adimensional incident power $(F/\gamma)^2$. (e)-Sketch of the Optical Limiter mechanism.

can be appreciated, notice for low pump powers $(F/\gamma)^2 \lesssim 10^2$ tthat he nonlinear shift is negligible and $(F/\gamma)^2 = \kappa N_{Tot}$ which is the expected linear response of the system. An absolute calibration of the experimental N_{Tot} and (F/γ) values so the plot reproduces the effective occupation number of the cavities is possible once all the collection line losses, the back mirror reflectivity, the pump coupling efficiency and the quantum efficiency of the CCD are known. However the coupling efficiency depends from structure to structure and is sensitive to the piezo positioning vibrations, the task becomes then rather difficult: since we are mainly interested in this section in testing qualitatively the physics of nonlinear coupled cavities the experimen-

tal plot axis have to be interpreted at least of the proportionality constants (α,β) defined by $F^2 = \alpha P_{Pump}$ and $N_{exp} = \beta N_{sim}$. In figure 4.7-(b,d) we show an imaging of the transmitted irradiance for two different pump powers, both of them show a bonding-like shape. This is the straighforward consequence of the strong overlap of the pump line with the boning mode $\hbar(\omega_B - \omega_{Pump}) \approx \gamma$ whereas $\hbar(\omega_A B - \omega_{Pump}) \approx \gamma + 2J \gg \gamma$ and the overlap with the antibonding mode is strongly inhibited. Notice that while at low power the mode profile is a smooth bonding mode, for an higer pump power the profile is deformed this tells us that the linear bonding mode is anymore a good eigemode of the nonlinear Schrödinger equation system (4.11). The fact that for every value of the pump power, the nonlinear "bonding" mode ψ_+ is dominating the pillar transmission, is equivalent to the statement that the solutions of equation (4.13) in the Optical Limiter (OL) regime are stable for every pump power. As we are going to discuss this can be anymore the case for detunings smaller than J, were single mode instabilities and parametric instabilities can emerge.

The stability of the solutions can be assessed by evaluating the spectrum of small fluctuations around the stationary solution [58], if

$$\psi_{L,R}(t) = \left(\sqrt{N_{L,R}} e^{i\varphi_{L,R}}\right) e^{i\omega t} = \psi^{ss}_{L,R} e^{i\omega t} \tag{4.16}$$

which is the ansatz form of the steady state solutions of (4.11) under a coherent driving, a small perturbation has the form

$$\psi_{L,R}(t) = \left(\psi^{ss}_{L,R} + \delta\psi_{L,R}(t)\right) e^{i\omega t} \tag{4.17}$$

the equations of motion can be linearized around the steady state solution by substituting (4.17) in (4.11) and dropping all the terms $\mathscr{O}(\delta\psi^2)$, after some algebra one gets

$$\frac{d\delta\psi_{L,R}}{dt} = \left(\delta - i\frac{\gamma}{2}\right)\delta\psi_{L,R} + 2U|\psi^{ss}_{L,R}|^2\delta\psi_{L,R} + U(\psi^{ss}_{L,R})^2\delta\psi^*_{L,R} - J\delta\psi_{R,L} \tag{4.18}$$

where $\delta = \hbar(\omega_0 - \omega)$ and ψ^* denotes the complex conjugate of ψ. Now one can substitute in (4.18) the time evolution ansatz

$$\delta\psi_{L,R}(t) = e^{-\frac{i}{\hbar}Et}\mathscr{U}_{L,R} + e^{\frac{i}{\hbar}E^*t}\mathscr{V}^*_{L,R} \tag{4.19}$$

expressed as the sum of two counterpropagating waves carrying an excitation energy E with a fluctuation amplitude $\mathscr{U}_{L,R}$ and $\mathscr{V}_{L,R}$. The linearized equations of motion for the fluctuation can be cast thanks to the time evolution (4.19) in the form of a secular equation

$$\mathscr{B}\cdot\delta\Psi = E\delta\Psi \tag{4.20}$$

where $\delta\Psi$ is the vector $(\mathscr{U}_L, \mathscr{V}_L, \mathscr{U}_R, \mathscr{V}_R)^T$ and the matrix $\mathscr{B}$ has the form

$$\mathscr{B} = \begin{pmatrix} \left(\delta - i\frac{\gamma}{2}\right) + 2UN_L & U(\psi_L^{ss})^2 & -J & 0 \\ -U(\psi_L^{ss\,*})^2 & -\left(\delta + i\frac{\gamma}{2}\right) - 2UN_L & 0 & J \\ -J & 0 & \left(\delta - i\frac{\gamma}{2}\right) + 2UN_R & U(\psi_R^{ss})^2 \\ 0 & J & -U(\psi_R^{ss\,*})^2 & -\left(\delta + i\frac{\gamma}{2}\right) - 2UN_R \end{pmatrix} \tag{4.21}$$

The eigenvalues of this Bogolibov matrix encodes all the informations about the spectrum of the small fluctuation an therefore about the steady state solution stability. If we call E_α with $\alpha = 1,..,4$ the comlex eigenvalues of $\mathscr{B}$, three different scenarios can be spotted

- If the imaginary part satisfies $\Im[E_\alpha] < 0 \ \forall\alpha$, the normal modes of the fluctuations $\delta\Psi_\alpha$ are damped over time, and the solution is STABLE.
- If $\exists\alpha$ so that $\Im[E_\alpha] \geq 0$ and $\Re[E_\alpha] = 0$ a small perturbation gets amplified over time and the steady state solution is called (Single mode) UNSTABLE.
- If $\exists\alpha$ so that $\Im[E_\alpha] \geq 0$ and $\Re[E_\alpha] \neq 0$ a small perturbation gets amplified over time and since $\Re[E_\alpha] \neq 0$ the perturbation has a fluctuating behaviour; the steady state solution is called PARAMETRICALLY UNSTABLE.

In this section we are mainly interested in single mode instabilities of the solutions, butin the next section we will see how a parametric instability originates a self pulsing dynamics of the steady state solution. With this information about the solution stability we can finally address the intersting phenomenon of optical bistabilities in coupled nonlinear cavities.

The intuitive description of the phenomenon is the following: imagine to pump the left pillar at an energy which is slightly redshifted respect to antibonding mode, as the power is increased the nonlinear shift of the modes is able to push the "bonding" energy E_+ in resonance with the pump. Correspondingly the initial antibonding-like mode becomes unstable and the system jumps to the nonlinear "bonding" mode. When the pump power is gradually decreased the system stays in the "nonlinear" bonding mode up to a threshold where the mode becomes unstable and the coupled pillar nonlinear eigenmode jumps back to the antibonding-like one. The occurrence of regions of one-mode instability for energies higher than a mode resonance is a well studied subject in the general literature on instabilities. Concerning nonlinear optical systems, it has been extensively studied both in the simplest case of single cavities [62] as well as in more complex cases of coupled optical cavities [63]-[64]. The above described mechanism often results in the coexistence of two or more stable solution for the same values of the incident pump

power and detuning, these phenomena are called respectively bistability and multistability. In the simplest case of bistability an hysteretic cycle appears: as the pump amplitude F increases from zero, the system moves along the lower branch of stable solutions until its end point is reached. Only at this point the system jumps on the upper branch. If the pump amplitude is then decreased, the system keeps moving along the upper branch of stable solution until its end point is reached, where it jumps back to the lower branch.

The bistabile regime of the two coupled nonlinear oscillator is the starting point for our futher studies on the parametric instabilities, we threfore investigated both numerically and experimentally this phenomenon, while we refear to the recent work of S. Rodriguez et al. for the regime where multistability occurs[25].

In figure 4.8-(a,b) we show the site resolved transmitted intenisty as a function of the incident pump power for the same pillar investigated for the optical limiter experiment but with a pump detuning $\delta = \gamma - J$ as schematized in the inset of panel (a). The measured N_L and N_R shows a clear hysteretic cycle due to the bistability occuring when $(5 \lesssim P \lesssim 44)mW$. The two points which are in between the two branches of the cycle in correspondence of the jumps triggered by the single mode instabilities occurring at $P \sim 5\ mW$ and $P \sim 44\ mW$ are artifacts due to the finite exposure time of the CCD (here $0.4\ s$). Indeed close to the jumps even the smallest power fluctuation may trigger in between the CCD integration time the transition to the upper or lower branch. An interesting feature of the driven cavity is that N_L starts to grow as N_R with P but a certain point has a relative maximum and then decrease as P is increased forming a dip before the first threshold is reached, this feature was demonstrated [25] to be ascribable to an interaction induced hopping phase $\Delta\phi_{LR}(F) = (\varphi_L - \varphi_R)$. Indeed if a polariton hopping back and forth from the left site acquires a round trip phase equal to π it destructively interferes with the polaritons injected by the pump. The signature of this effect is an almost complete darkening of the driven pillar when pump power is such that $\Delta\phi_{LR} \approx \pi/2$.

In figure 4.8 panels (1) to (4) we plot an imaging of the mode profiles corresponding to four different pump powers along the four branches. Panel (1) corresponds to one of the frames recorded at low power and shows an antibonding-like character since the pump energy is close to the linear E_- eigenvalue of (4.11). Panel (2) still belongs to the lower branch of the hysteresis cycle and corresponds to the point were the destructive interference condition $\Delta\phi_{LR} \approx \pi/2$ is matched, correspondingly the driven pillar becomes dark, the weak residual emission is due to the scattered light from the pillar sides. Panel (3) corresponds to the coupled pillar emission after the power exceeds the lower branch threshold, unlike panel (1) and (2) the density profile of the emission resembles the bonding mode, since a bright emission from cavities overlap region is clear signature of the symmetric character of the nonlinear ψ_+ eigenmode. The emission plotted in (4) still belongs to the upper branch but for a pump power close to the downward

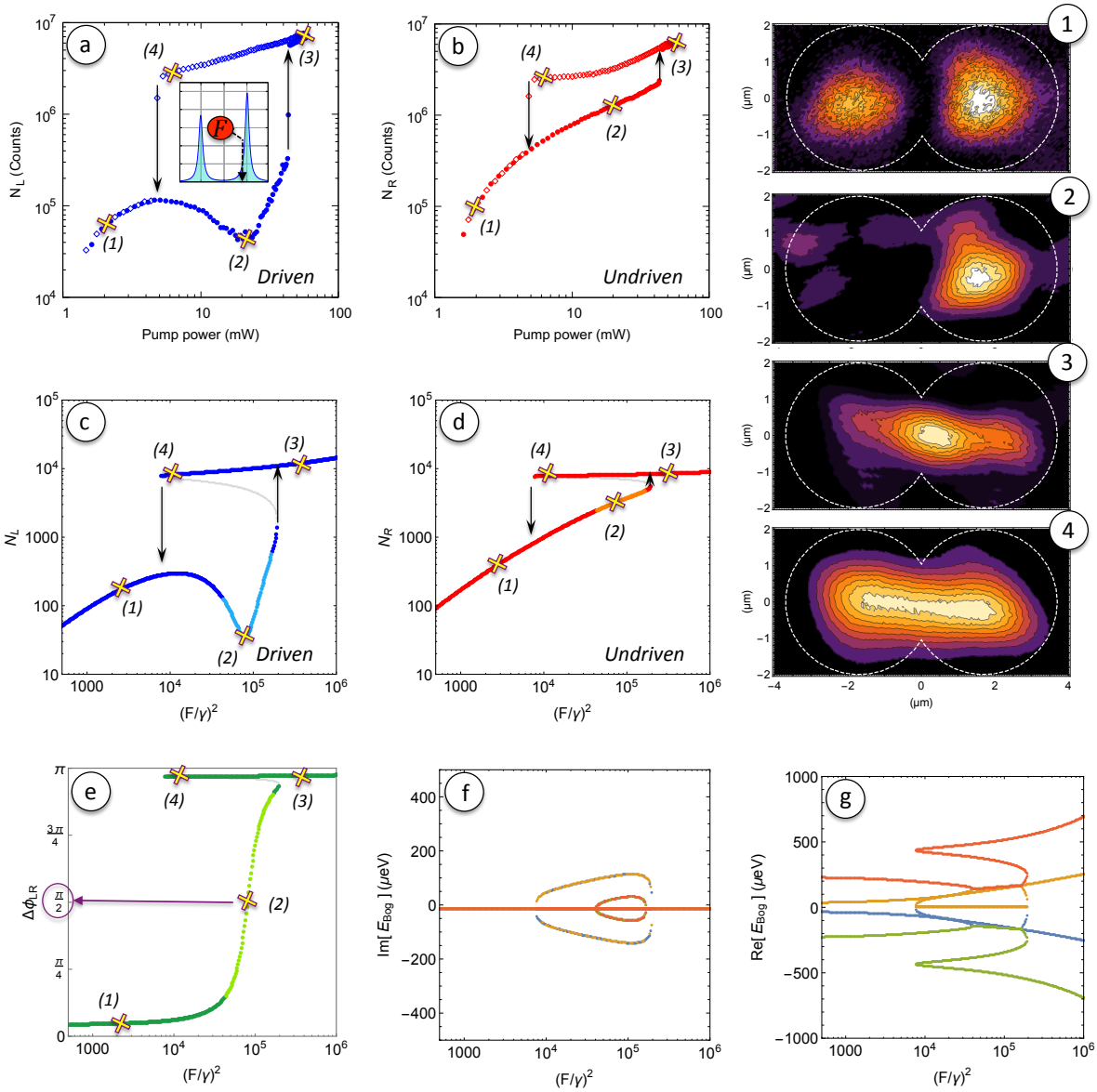

Figure 4.8: (a)-(b) Measured N_L and N_R as a function of the incident pump power on the left pillar, the pump detuning is $\delta = \gamma - J$ as depicted in the inset of panel (a). The filled circles represents the data points recorded for an increasing pump power while the hollow diamonds represent the corresponding backward process; an hysteretic cycle is evident as consequence of the system bistability. (c)-(d) Simulation of the experiment: the blue and red points are stable solution of (4.13), the cyan and orange points correspond to parametrically unstable solutions and the gray points correspond to single mode instabilities. (e)-Interaction induced hopping phase $\Delta\phi_{LR} = (\varphi_L - \varphi_R)$, notice that if $\Delta\phi_{LR} = \pi/2$ a polariton hopping back and forth experience a round trip phase difference of π thus interfering destructively with the polaritons injected by the pump beam. (f)-(g) Imaginary and real part of the bogoliubov matrix $\mathscr{B}$ eigenvalues. (1-4) Imaging of the transmitted irradince density profiles corresponding to data points marked with a cross in panels (a),(b). The plots (1) and (2) belongs to the lower branch of the hysteretical cycle and shows an antibonding-like character, while (3) and (4) belongs to the upper branch of the cycle and shows an bonding-like character. The left site in (2) is dark beacuse of the inteaction induced interference.

threshold, since the power is pretty low the ψ_+ eigenmode profile closely resembles the linear bonding mode. The overall picture resulting from the panel (1) to (4) supports the euristic interpretation of the bistability mechanism discussed few paragraphs ago.

In figure 4.8-(c,d) we show the corresponding simulations which are in qualitative agreement with the experimental results. Notice that from a theoretical point of view the hysteretic cycle is just apparent, indeed if we take the first equation of the set it parametrizes a manifold $\mathscr{M}$ embedded in $\mathbb{C}^2$ and the second equation in this picture can be regarded as a constraint folding $\mathscr{M}$ to a complex curve in $\mathbb{C}^2$ (since the folding polynomials are analytic, the curve is unique and analytic itself). Moreover since a parametric curve in (F,δ) defines a unique point $\mathscr{P}$ in $\mathbb{C}^2$ once the dring power and detuning are fixed, the bistabilities are the result of the projection of $\mathscr{P}$ into the real parts $\sqrt{N_{L,R}}$.

In figure 4.8-(c,d) the darker colors represents stable solutions, the lighter colors denotes the parametrical instabilities and the gray dots marks the single mode unstable solutions, the hysteretic cycle happens beacuse the lower branch becomes unstable and the only allowed state for an higher pump power belongs to the upper branch, and the same happens in the downward threshold, if we follow the solution disregarding the stability of the solution our simulation allows to appreciate the uniqueness and analyticity of the $N_{L,R}$ curve as a function of F.

We shall comment the fact that in the simulation of N_L a more pronounced dip appears respect to the experiment, this happens beacuse of an admixture of diffrent effects: the first is scattered light from the pillar sides which becomes disturbing when a pillar gets dark but the pump power is high as in figure 4.8 panel (2), another effect depends on the size of the pump gaussian beam spot $2\sigma \sim 2\mu m$, which results in a small coherent driving also on the right pillar; this of course spoils the efficiency of the destructive interference mechanism. Another subtle effect comes out of the parametrically unstable nature of the solutions close to the dip, as we mentioned such an instabilities happens if $\exists\alpha$ so that $\Im[E_\alpha] \geq 0$ and $\Re[E_\alpha] \neq 0$, meaning the perturbations are amplified and since $\Im[E_\alpha] \geq 0$ they induce a self pulsing dynamics of the steady state solution (dynamic equilibrium) [58]. However nothing tells us that the average population $N_{dyn} = \langle|\psi_{LR}^{dyn}(t)|^2\rangle_t$ in the self pulsing dynamics of the perturbed dynamical stady state, equals the unperturbed solution $N_{ss} = |\psi_{LR}^{ss}|^2$ of (4.13). Since noise is ubiquitous in experiments what we measured in panel (a) is N_{dyn}, whereas we plot N_{ss} in the simulation of panel (c). In the 2008 paper by D. Sarchi et al. -[58]-fig. (7,c)- the time dynamics of the left and right population was obtained by solving the steady state nonlinear Shrödinger equations (4.11) and by adding a small femtosecond pulse probe triggering the parametric instability: the simulation supports our experimental observation since $N_{L,dyn} > N_{L,ss}$.

Panels (f,g) in fig 4.8 show respectively the imaginary and real part of the eigevalues of the

Bogoliubov matrix (4.21). In the linear regime $N_{L,R} \to 0$ the frequency and damping rates tends to the linear eigenvalues ones encoded in (4.12) and $\Re[E_{1,3}] = -\Re[E_{2,4}] = \pm J - \delta$ and $\Im[E_\alpha] = -\gamma/2 \ \forall \alpha$. The positive or negative weight of the $\alpha = (1,3)$ or $\alpha = (2,4)$ modes is determined by the Bogoliubov metric η of $\mathscr{B}$, where $\eta = diag(1,1,-1,-1)$. As a consequence of the metric η signatures the $\Re[E_{1,3}]$ modes are blueshifted as the pump power increases and vice versa for the $\Re[E_{2,4}]$, this results in pairwise intersections where $\Re[E_{2(4)}] = \Re[E_{1(3)}]$ as the power increases. Correspondingly the imaginary part of two of the $\mathscr{B}$ eigenvalues damping rate decrease $\Im[E_1] = \Im[E_4] < -\gamma/2$ or increase $\Im[E_2] = \Im[E_3] > -\gamma/2$, once one of the eigenvalues crosses the zero an instability appears which parametric nature depends on the nonm zero magnitude of the corresponding real part. Notice in panel (f) that the instabilities correspond to a couple of imaginary eigenvalues which imaginary part bifurcates, this phenomenon in the language of dynamical systems is often called an Hopf bifurcation.

The last panel we shall comment is 4.8-(e) where the phase difference between the left and right polariton field is plotted as a function of the pump intensity, this interaction induced hopping phase was experimentally measured in the 2016 by S. Rodriguez et al. [25]. This tunable phase has both the merit of explaining in terms of a interference process the driven site darkening, both paves a way to implement density-dependent artificial gauge fields and nontrivial hopping phases in bidimensional lattices of coupled microcavities. Indeed a particle acquiring a nonzero phase ϕ along a closed-loop trajectory implies the existence of a nonzero vector potential $\mathbf{A}(\mathbf{q})$, since

$$\phi_{i,j} = \int_{\mathbf{q}_i}^{\mathbf{q}_j} \mathbf{A}(\mathbf{q}) \cdot d\mathbf{q} \tag{4.22}$$

Once this phase can be tuned arbitrarily, topologically non-trivial states can be achieved opening very interesting scenarios in the photonics community. In particular this feature tells us that a polariton field confined in a network of coupled cavities not only simulates a driven-dissipative Bose-Hubbard model but also manifests a richer physics as a consequence of these interaction-induced hopping phases which turns the real valued coupling $J_{i,j} = J$ of the Bose-Hubbard model in a driving dependent complex term $J_{i,j} = Je^{i\Delta\phi(F_i)}$.

4.3 Tunneling Induced Parametric Instability

When we addressed the stability of the solutions of (4.13) by calculating the spectrum of the small fluctuations around the steady state, an intersting class of dynamical instabilities emerged. In the simulations (c)-(d) in figure 4.8 a parametrical instability was predicted to characterize the steady state dynamics of the coupled micropillars when driven in a region of detuning $-J < \delta < 0$ for a power close to the lower branch upward threshold, where the interaction-induced hopping phase results in a destructive interference process with the pump (fig. 4.8 panel (2)). We used this information to explain a posteriori the measured shallower dip respect to the simulated data points recalling the results present in the theoretical work of D. Sarchi et al. [58]. In this section we show the first experimental evidence of the predicted interaction-induced parametric instability in a photonic molecule.

The parametric scattering process we are looking at depends on the interplay of hopping and nonlinearities. As already discussed the intuitive effect of the on-site Kerr nonlinearity is to blueshift the two linear eigenmodes, for a pump detuning $-J < \delta < J$ a bistable regime is observed, however no parametric instability is observed if $0 < \delta < J$, see for instance figure 4.9-(a,b) where we plot the simulated steady state solutions of N_L as a function of the pump power respectively for a pump detuning $\delta = 3\gamma < J$ and $\delta = -3\gamma > -J$, this simple observation is the key to understand the parametric instability phenomenon. Indeed if $-J < \delta < 0$ it will exist a pump power F_0 such that

$$E_+(F_0) + E_-(F_0) = 2\hbar\omega \tag{4.23}$$

where $E_\pm(F)$ are the pump power-dependent nonlinear eigenenergies associated to the eigenmodes $\Psi_\pm$, vice versa if $0 < \delta < J$ this condition will never be satisfied since the energy level blueshift but the pump is redshifted respect to the Ψ_- mode.

If the relation (4.23) is fulfilled two polaritons injected at the pump frequency ω have a resonant scattering channel where the final states are a signal field with $E_S = E_-(F_0)$ and an idler field field with $E_I = E_+(F_0)$. If the losses of the system are taken in account the detuning range where this parametric process happens is $-J + U N_R < \delta < -\gamma$ [58], where the stationary solutions are stable for small pump amplitudes but become parametrically unstable as soon as the parametric gain is able to overcome the losses $U N_R > \gamma$, notice that the N_L contribution to the nonlinear blueshift of the levels can be safely neglected in this analysis since $N_R \gg N_L$ in the region where the parametric process may take place i.e. see 4.8-(c,d).

In figure 4.9-(c) we schematize the parametric instability mechanism. The reason why the losses have to be included -$\delta < -\gamma$ instead of $\delta < 0$- is that for $-\gamma < \delta < 0$ the power at which the res-

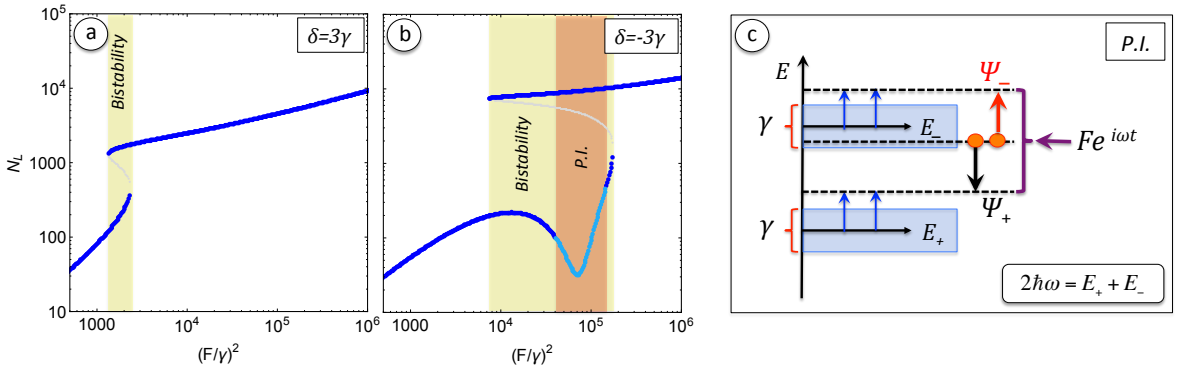

Figure 4.9: (a)-N_L calculation for a positive detuning $\delta = 3\gamma$, an hysteresis cycle due to the bistability can be observed, however only stable (blue dots) and single mode unstable (gray dots) solutions can be observed since any F satisfies (4.23). (b)-Same of panel (a) but for a negative detuning $\delta = -3\gamma$, parametrically unstable solutions (light blue dots) appears in the region corresponding roughly to the N_L dip induced by the hopping phase interference mechanism. The calculations adopted J, U and γ matching the previous section calculations. (c)-Schematic of the parametric scattering mechanism.

onant condition $E_+(F_0) + E_-(F_0) = 2\hbar\omega$ is satisfied is such that $U N_R < \gamma$ thus implying the rate at which the signal and idler fields are created is smaller than the losses and the amplification of the perturbations is inhibited. On the contrary if the rate of the scattering process exceeds the losses a strong amplification of fluctuations around the stationary solution eventually results in a self-pulsing dynamics of the steady state where the system keeps on oscillating for indefinite times. These oscillation in the three mode picture of a pump, signal and idler field can be interpreted as the result of the interference of the three fields since $\omega_P \neq \omega_S \neq \omega_I$, a similar description is often encountered in literature when discussing the physics of Optical Parametric Oscillator (OPO).

An OPO is a well-known device since the 1965 seminal work of J. Giordmaine and B. Miller [65] and it is now widely used to generate squeezed states and entangled states of light in the continuous variables regime. The generation of a parametric scattering process was already observed in planar microcavities [19] as Optical Parametric Amplification (OPA) due to bosonic stimulation [18]-[59], an OPO was also realized with single pillar structures with an engineered level structure [20]-[21], but was never observed in coupled cavities where the phenomenon emerges as a natural consequence of the interplay of hopping and nonlinearities and manifests himself in a self-pulsing dynamical steady state of the pillar.

This tunneling-induced parametric instability of the coupled cavities steady state can be found also in the region where $\delta < -J$ (i.e. the pump is blueshifted both respect to the linear $\Psi_\pm$ modes) however $\delta < -J$ regime is characterized by complex multistable behaviours of the solutions thus complicating the interpretation of the observations. Hereafter we focus on the

$-J+UN_R < \delta < -\gamma$ regime and we let the case of parametric instabilities in the multistability for future investigations. For those who are interested in a global perspective on the stability of the steady state solutions of the coupled oscillators, we performed a set of simulations where the plots of fig 4.8-(c,d,e,f,g) were calculated for 130 different detuning values ranging between $\delta \approx 4J$ and $\delta \approx -6J$ in steps of $\Delta\delta = 10\ \mu m$; J, U and γ were chosen to match the parameters derived for the (D-B)-(5) pillar investigated in the previous section. The different panels were assembled in a video were time runs the detuning from $4J$ (OL regime) to $-6J$ (Multistable regime). The below hyperlink allows the download of the simulation

♦ COUPLED PILLAR STEADY STATE & STABILITY ♦

The experimental investigation of this process can be done in two ways, the first one involves the direct imaging of the pillar population resolved in time; such a measurement involves a streak-camera which allows a 1D imaging with a temporal resolution of few picoseconds ($2 \div 4\ ps$). The characteristic timescale over which the $N_{L,R}$ dynamics evolves over a full cycle is set by the beatings periods of the pump, signal and idler fields $\omega_{P,S,I} \gg (\omega_S - \omega_I) \approx (J/\hbar)$ which entails $\tau_{OPO} \sim 1/\Delta\omega \sim (\hbar/J) \sim 6\,ps$ for a coupling energy $J = 100\mu eV$. These timescales are close to the temporal resolution of the best commercial streak cameras suggesting that a different measurement strategy is needed. Indeed the creation of a signal and idler field can be easily detected from it's spectral signature: when the pump power is enough to trigger the parametric process the creation of $\Psi_{S,I}$ must manifest as two side peaks in the energy resolved emission of the coupled pillars. The only limiting factor in this measurement is the spectrometer resolution, in our case $2\gamma_V = \Delta E \sim 60\mu eV$ (e.g. see section 3.1), the side peaks can be therefore resolved if $J > 2\gamma_V$ which is safely satisfied by almost all the dimer structures present on the sample.

In the following measurements we moved from motif (D-B)-(5) to motif (D-A)-(4) the reason of this choice is that most of the parametric processes have an efficiency which strongly depends on the nonlinear coefficient; for instance the efficiency of an OPO process in multiple planar microcavities was observed to depend on the eighth power of the Hopfield coefficient [66]. While the pillars in motif (5) have a very small exciton component, motif (4) offers an enhanced nonlinearity still preserving a good photonic component which ensures small linewidths and good optical properties of the structure (here $X^2_{GS,4} \approx 0.16$ whereas $X^2_{GS,5} \approx 0.07$). As discussed in section (1.4.3) the main contribution to exciton exciton interactions corresponds to co polarized Pauli scattering channel [44]-[46]-[45] where two excitons exchange the electrons or the holes, however the cross section of this process critically depends on the exchanged momentum q decreasing roughly a factor of two at $qa_B = \hbar$ [67] i.e. when the inverse of the scattered wave vector is order of the QW exciton Bohr radius. This suggests that the efficiency of the process decrease as J is increased. We chose a pillar having

$$J = (178.4 \pm 1.4)\ \mu eV \quad \gamma = (37.5 \pm 1.2)\ \mu eV \quad U \sim 0.07\ \mu eV$$

So that the coupling is roughly three times the spectrometer resolution (minimal to resolve clearly the eventual side peaks) and the nonlinear coefficient is roughly two times the one of the pillars in motif 5. We set a pump detuning slightly reshifted respect to the anti-bonding line $\delta = \gamma - J$ and we recorded the space and energy resolved emission of the coupled pillar while scanning the power in the resonant transmission configuration. The dimer emission was imaged so that the $10\mu m$ slit was aligned with the dimer axis and the pump linear polarization was parallel to the slit.

In figure 4.10-(a) to (e) we show five illustrative frames of the energy and spatially resolved emission, the ordinate corresponds to the position along the dimer axis and the abscissa is the energy we calculated trough the calibration (3.1). Figure 4.10-(g) reports a calculation of N_L based on the new values of U, J and γ which is useful to understand the y-profiles of the dimer's emission (a) to (e) in relation with the bistability experiment of the previous section, the red (green) arrow denotes the *forward* (*backward*) power scan direction. Panel (a) corresponds to $P = 0.7mW$, here the nonlinear blueshift is still weak and an antibonding-like profile can be deduced from the emission in analogy with figure 4.8-(1). Notice that the energy of the emission corresponds to the pump energy $\hbar\omega_P \approx 1476.73\ meV$. In panel (b) the profile shows still an antibonding-like profile but a progressive darkening of the left pillar can be observed according to the interference mechanism discussed in the previous section e.g. fig. 4.8-(2). As the power is slightly increased from (b) two symmetrically spaced side peaks emerges (panel c): the parametrical process threshold is reached and the the creation of the signal and idler modes becomes resonant. We can measure the energy separation respect to the pump line to find $\Delta E \approx J$, this is the clear signature of the a parametric scattering process of the pump into the nonlinear $\Psi_\pm$ modes. Increasing even further the pump power the side peaks are progressively washed out as the resonance condition (4.23) is left, the upward threshold is reached and the system jumps to the upper branch. In both panel (d) and (e), corresponding to a very high pump power and a pump power slightly higher than the downward threshold, the bonding-like profile characteristic of the upper branch can be appreciated, this again is in agreement with the observations of the previous section. The small dark line cutting around $0.5\mu m$ the nonlinear bonding mode profiles in panel (d)-(e) is caused by a dust particle which deposited during the measurement on the slit knifes, the bright emission spot close to the center of the dimer (d-e) is probably originated by a localized point defect in the QW since its emission is localized in space and slightly blueshifted respect to the QW polariton emission.

The energy and space resolved emission of the pillar was recorded for 110 values of the pump power, both scanning forward $P_0 \rightarrow P_{max}$ and backward $P_{max} \rightarrow P_0$. Every frame was then projected along the ordinates, obtaining an intensity profile corresponding to the spectrum of the dimer emission for every pump power P_i, $i = 1, ..., 110$. In figure 4.10-(f,h) the spectra recorded at different P_i are meshed in a energy and power resolved emission. In the forward scan map as

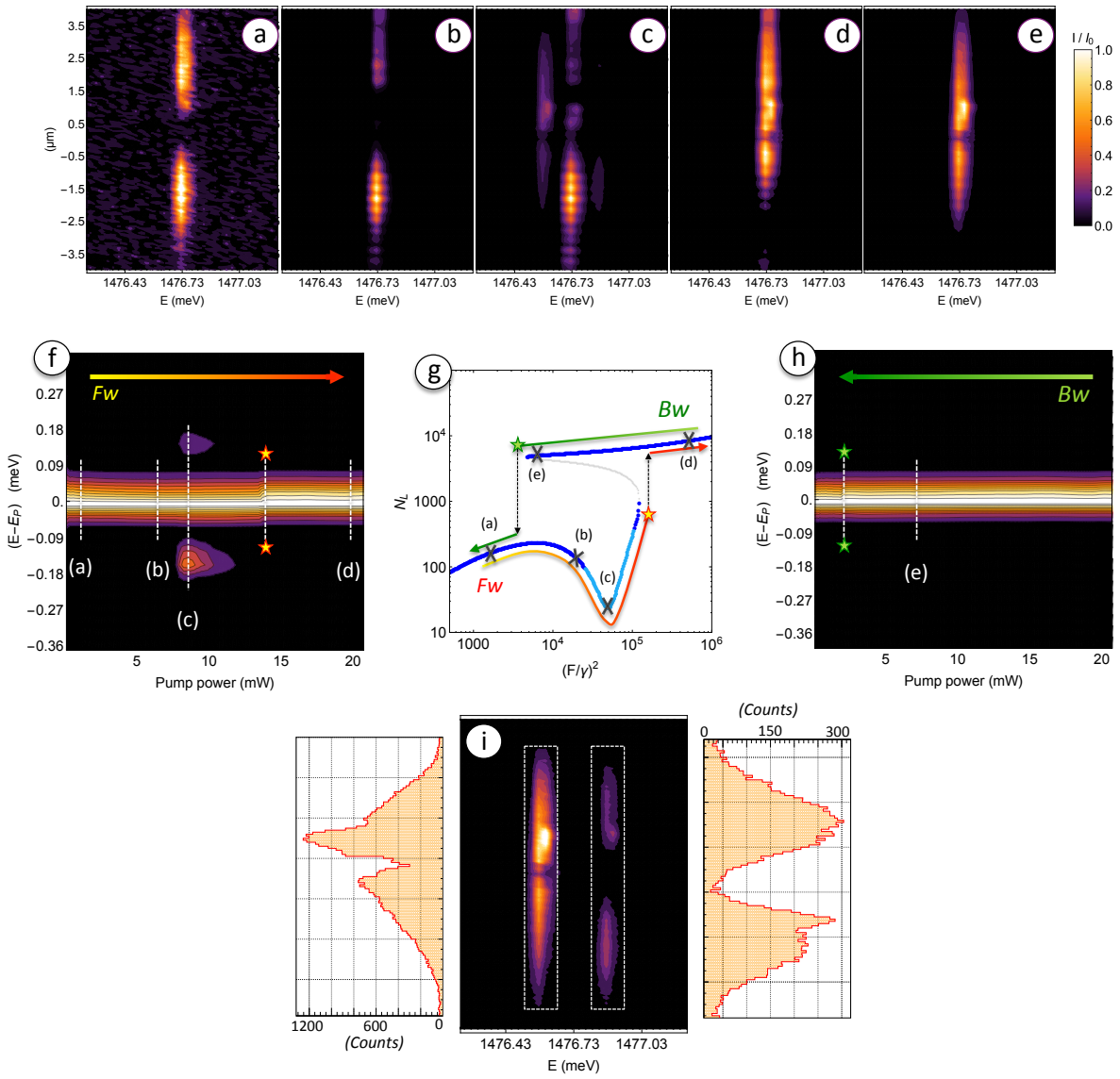

Figure 4.10: (a,b,c,d,e)-Resonant transmission of the dimer resolved in energy and space for different pump powers, the ordinates runs along the dimer axis. (a,b,c) Belongs to the lower branch, the antibonding-like profile of the pump emission can be appreciated, $P_{(a)} \approx 0.8\,mW$, $P_{(b)} \approx 7.0mW$ and $P_{(c)} = P_{res} \approx 8.6\,mW$. (c) shows two side emission lines corresponding to the signal and idler mode. (d,e) Belongs to the upper branch showing the expected bonding-like profile. (f,h)-Spectral resolved emission of the dimers as a function of the pump power respectively for the forward and downward scan; the white dashed lines corresponds to the projection along the ordinates of the spectra (a) to (e), the stars denotes the upward and downward thresholds. (g)-Calculation of the N_L population highlighting the different (in)stability regions, the gray cross corresponds qualitatively to the position on the upper and lower branch of the panel (a) to (e). (i)-Cross polarized resonant transmission of the dimer, the orange side profiles results from the projection along the abscissae of the mode profiles. A clear identification of the signal with Ψ_- and of the idler with Ψ_+ can be deduced.

the power reach the value of $P \approx 7.3mW$ the parametric process threshold is reached and two side peaks can be resolved, when increasing the power to $P \approx 8.5mW$ the parametric process becomes resonant and is slowly washed out as $P > 8.5mW$. The upward threshold can be detected in the spectrum as a small kink in the contour lines and is marked by the red stars. The width of the power window where the parametric process can be observed is related to the finite linewidth of the $\Psi_{\pm}$ modes, allowing the signal+idler scattering process within $-\gamma \lesssim 2E_P - E_S - E_I \lesssim \gamma$. In panel (h) the backward scan evidences any side peak, this is consistent with the prediction of the simulation (g), we mark again the small kink in the emission corresponding to the downward threshold with two green stars. The reason of this small kink in the contour lines when jumping between on branch and the other is that the inhomogeneus broadening term in the polariton linewidth depends on the surface exciton density in the QW: when the population has a discontinuity as in the jumps from one branch to the other, the linewidth has a small discontinuity itself. Since the spectra meshed in the color plot are normalized so that the peak height is 1 the contourplots show a kink.

The parametric scattering process efficiency strongly depends on the polarization of the signal and idler final states once the pump polaritons are assumed to be linearly co-polarized. In particular the dominant scattering channel is trough final states which have a polarization orthogonal to the initial states' one [67]. Since the emission coming from the pump polaritons is almost completely polarized along the dimer axis we can take advantage of the mainly orthogonal polarization of the signal and idler by cross-polarizing the transmitted light along the collection line. This results in a strong suppression of the pump emission allowing a clean resolution of the signal and idler mode profiles. In figure 4.10-(i) we show the cross polarized emission measured corresponding to a pump power matching the resonant condition of the parametric process. The signal mode profile closely resembles the antibonding one, whereas the idler field shows a bonding-like profile deformed by the bright emission from the point-like defect in the QW and by the dust particle deposited on the slit. One can further convince himself that the signal and idler modes correspond to the nonlinear Ψ_- and Ψ_+ modes comparing figure 4.10-(a,e) with 4.10-(i).

In figure 4.11 we report the energy resolved transmission of the dimer for the three different pump powers which are representative of the three possible steady states characterizing the system in the window $-J + U N_R < \delta < -\gamma$: a low power stable solution P_L belonging to the lower branch of the hysteretical cycle, a parametrically unstable solution P_{Res} corresponding to the resonant condition (4.23), and a high power stable solution P_H belonging to the upper branch. The spectra corresponding to these three classes of solutions are respectively plotted in red, blue and orange. The experiment was repeated for a pump detuning ranging between $\delta = -J$ and $\delta = 3\gamma - J$ in steps of γ and the results corresponds to the four graphs in the leftmost column of figure 4.11. From these graphs its clear that the efficiency $\varepsilon_{S,I}$ of the parametric scattering

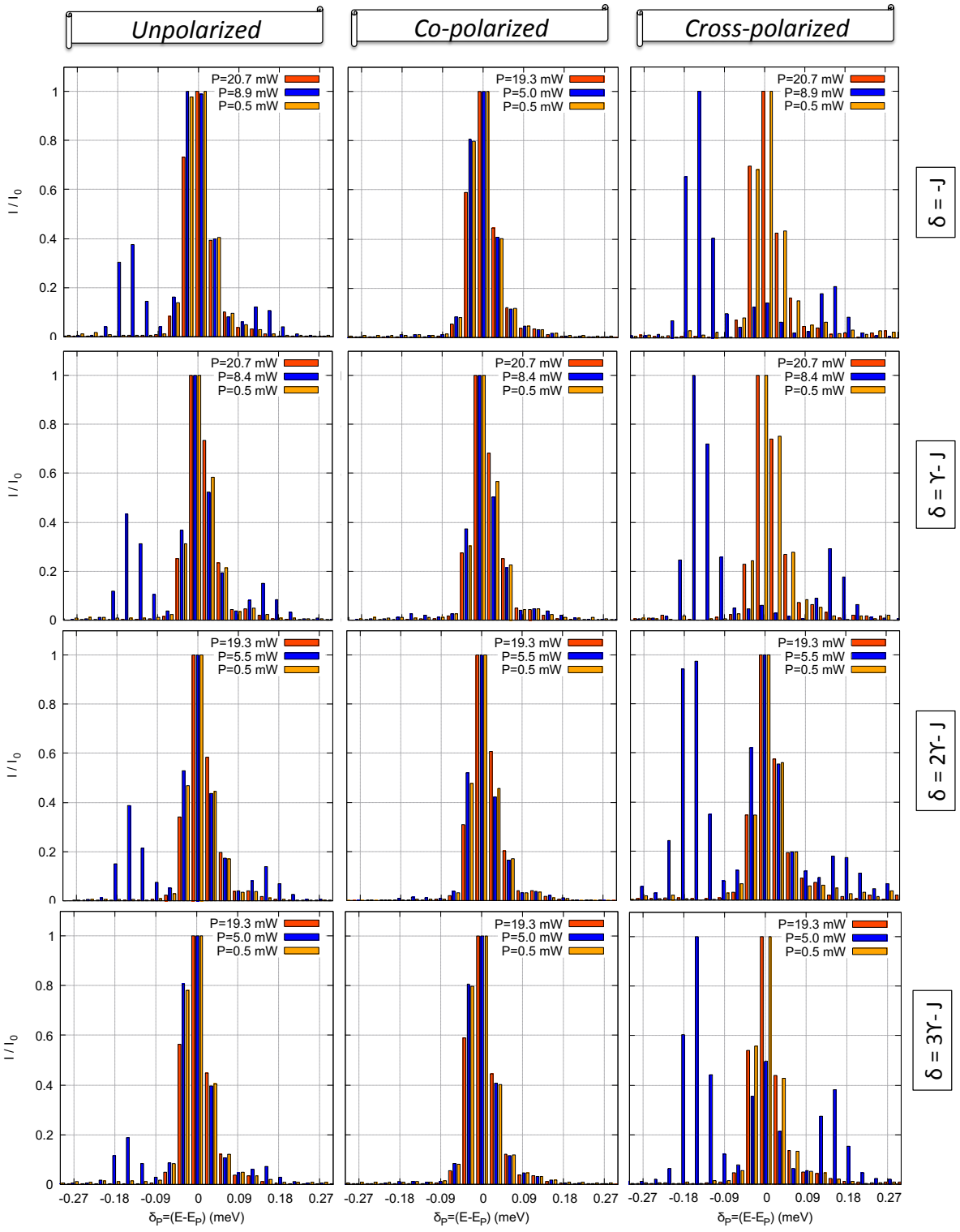

Figure 4.11: (First column)-Energy resolved transmission of the coupled pillars at a low power (red), at the parametric resonant condition (blue) and high power (orange), the pump detuning is varied between $\delta = -J$ i.e. resonant with the antibonding mode and $\delta = 3\gamma - J$ in steps of γ. (Second column)-The transmission is filtered with a high quality polaroid with the axis aligned with the pump linear polarization. (Third column)-The polaroid axis is orthogonal respect to the pump.

process depends on δ, in particular it decreases as the detuning is increased toward $\delta = -\gamma$, the higher values of efficiency are found for a pump one linewidth redshifted respect to the linear antibonding mode where $\varepsilon_I \approx 0.42$ and $\varepsilon_S \approx 0.17$. This can be qualitatively explained recalling that the scattering rate is proportional to the square of the exciton density in the structure, since the Pauli exchange interaction is a s-wave scattering channel mediated by a contact interaction and the exciton density grows as the detuning becomes closer to the antibonding line. This argument however does not explain why ε has a maximum around $\delta = \gamma - J$ rather than in $\delta = -J$, the development of a more quantitative model is currently still a work-in progress. We can also observe that the resonant condition (4.23) is matched at lower pump powers as the detuning gets closer to $\delta = -\gamma$ this is in perfect agreement with the UN_2 proportionality of the effective nonlinear modes blueshift, for a detuning closer to the linear antibonding line the shift has to be greater than for a detuning close to the bare cavity eigenfrequency (i.e. $\delta \to 0$), thus for $\delta \to -\gamma$ the pump threshold gets lower.

In the second and third column we report the co and cross-polarized spectra corresponding to the left-most panel of the row. When the emission is polarized along the dimer axis (i.e. parallel to the pump linear polarization) the three spectra corresponding to the three different pump powers P_L, P_{Res} and P_H can be perfectly superimposed: the side peaks for $P = P_{Res}$ are washed out. On the contrary if the transmission is cross-polarized the central peak corresponding to the pump is strongly inhibited whereas the side peaks for $P = P_{Res}$ dominates the spectrum. This fact collimates with the theoretical predictions [67]-[45] suggesting that the dominant dipole scattering matrix element for the s-wave exchange interaction for a linearly co-polarized $J_z = \pm 1$ excitons is the one producing two final states with an orthogonal polarization respect to the initial states. This still does not explain why the relative height of the signal and idler beam is different and changes with δ. We are now working on a model for the polarization and detuning-dependent values of $\varepsilon_{S,I} = I_{S,I}/I_P$ based on the calculation of the steady state of a coupled set of rate equations recounting for all the possible scattering channels between the two pump states, a pump state and the final state of another scattering and between the products of two scattering processes, however the project is still in a preliminary form.

The main result of this section is the experimental evidence of a tunneling induced parametric instability characterizing the steady state of two coupled nonlinear oscillators. For a pump detuning $-J + UN_R < \delta < -\gamma$ and a pump power satisfying (4.23) the creation of signal and idler field becomes resonant. This process was detected by means of energy and resolved measurements of the coupled pillars transmission. The imaging of the signal (idler) mode profiles allowed their identification with $\Psi_{-,(+)}$ and the parametric scattering of two pump polaritons in a signal and idler one was demonstrated to be highly selective in terms of the final state polarization. These results will be the subject of a forthcoming publication.

CHAPTER 5

Summary and Perspectives

In this thesis we presented an experimental study on the properties of 0D confined polaritons in InGaAs/AlGaAs based heterostructures. The confinement is provided by the abrupt refractive index mismatch between the air and the semiconductor when a pre existing planar cavity is etched down to the substrate to form a micron-sized pillar structure. The spectrum of the pillar structure becomes discrete and the lower polariton ground state energy depends quadratically on the side of the pillar structure section. Since polaritons are mixed light-matter states, the excitonic component provides an effective Kerr nonlinearity whereas the photonic component provides a finite coupling term two pillars have a finite overlap, as we discussed in section 1.4.3-4.2-4.1. The system is intrinsically lossy due to the radiative coupling to the free space modes mediated by the photonic component and because of the non-radiative processes inherited from the excitonic component.

All these ingredients allows to map a N-site network of coupled pillars into a driven dissipative Bose-Hubbard model. One of the principal advantages of the polariton framework is the extreme scalability of the pillar network, which geometry can be arbitrarily defined with a precision in the etching technique of few tens of nanometers. A second advantage is the extreme flexibility which can be achieved on the parameters characterizing the Bose-Hubbard model: the site ground state energy, the coupling among the sites and the on-site nonlinearity.

In section 3.2 we have shown that the ground state energy can be finely tuned by controlling the pillar size, proposing a simple method to measure the effective polariton mass.

In section 3.1 we show how the bare exciton to cavity photon detuning can be used to change

the excitonic X^2 and photonic C^2 component of the mixed polariton states, this can be used as a coarse grain knob to change the interaction constant $\propto X^4$ at the cost of an increased linewidth. In section 3.3 a novel result was presented: the sample temperature can be used to finely tune the effective Kerr nonlinearity in the pillar structures. A simple but comprehensive model was proposed to explain the interplay of temperature with the excitonic and photonic component of the confined polaritons. This result is interesting because since it prospects a way to control with an extraordinary accuracy the nonlinearity of the system, thus encouraging the search for unconventional photon blockade in photonic systems, a long lived theoretical prediction still never experimentally observed due to the extreme sensitivity of the phenomenon on the absolute value of the nonlinearity. This results will be the subjects of a forthcoming publication.

In section 4.1 we show how the coupling of two pillars results in the hybridization of the pillar ground state in analogy with the solutions of a quantum particle in a double well. The first two eigenmodes of the pillars were directly imaged in resonant transmission and can be identified with the so-called bonding and antibonding solutions of the double well hamiltonian. Within a two level approximation the energy splitting between the bonding and the antibonding modes is twice the coupling constant. We measured the dependence of coupling on the center to center spacing between the two pillars.

Trough these experiments a complete characterization of two coupled pillars was obtained. Since two pillars already comprehend all the fundamental ingredients of the driven dissipative Bose-Hubbard model, this work sets the basis for the design and implementation of an arbitrary network of coupled cavities.

In the last two sections 4.2-4.3 we investigate the nonlinear phenomena characterizing the steady state population of the two coupled cavities. When the pump power is swept for different detuning values, an optical limiter regime is observed when the pump is redshifted respect both the linear bonding and antibonding modes of the dimer as a consequence of the nonlinear blueshift of the coupled pillar eigenmodes induced by the Kerr nonlinearity. When the pump detuning is in the window $-J < \delta < J$ a bistable regime was observed, in particular a flashy darkening of the driven pillar population can be observed before the bistability threshold is reached which can be explained in terms of an interference process induced by a interaction dependent hopping phase. This specific result enriches the physics of the coupled cavities as it can be interpreted as a complex and power-dependent coupling in the driven dissipative Bose-Hubbard model. A non-trivial phase along a closed loop corresponds to a non-zero vector potential, this feature opens interesting perspectives on the realization of power-dependent artificial gauge fields on a network of driven pillars. Moreover when characterizing the stability of the steady state solutions belonging to the lower branch, a parametrical instability is predicted and we hereby report the first experimental evidence of the phenomenon. When the pump sat-

isfies a well defined resonance condition the effective polariton-polariton interactions result in a parametric scattering process which creates a signal and idler fields with an energy separated by $\pm J$ respect to the pump: the process can be detected from spectral resolved resonant transmission of the dimer emission. Interestingly the interference of the pump, signal and idler field results in a self-pulsing dynamics of the steady state. The scattering process was demonstrated to be highly selective in terms of the initial and final states polarization. This tunneling-induced parametric instability opens interesting perspectives on the generation of squeezed and entangled polariton states. This result will be the subject of a forthcoming publication.

The natural continuation of this work would be to address the steady state of more complex structures as three coupled pillars, arrays of pillars arranged on a ring or one and two dimensional lattices. In particular we already have some simulations suggesting the possibility of observing an interaction-induced symmetry breaking when pumping the middle site of three coupled pillars in a row. In ring topologies we expect to observe artificial gauge fields and some proposal to break the Lorentz reciprocity are currently being discussed. On the lattice structures the major challenge would be to implement a single site-resolved pump and detection in the setup. Moreover some recent theoretical works suggests the possibility of exploring the physics beyond mean field even for weak single particle nonlinearities, which are currently the main limiting factor towards quantum simulation with polariton microcavities.

Bibliography

[1] I. Bloch, J. Dalibard, and S. Nascimbene. “Quantum simulations with ultracold quantum gases”. In: *Nature Physics* 8 (4 2012) (cit. on p. 2).

[2] R. Blatt and C. F. Roos. “On-chip quantum simulation with superconducting circuits”. In: *Nature Physics* 8 (4 2012) (cit. on p. 2).

[3] A. A. Houck, H. E. Tureci, and J. Koch. “On-chip quantum simulation with superconducting circuits”. In: *Nature Physics* 8 (4 2012) (cit. on p. 2).

[4] A. Aspuru-Guzik and P. Walther. “Photonic quantum simulators”. In: *Nature Physics* 8 (4 2012) (cit. on p. 2).

[5] W. S. Bakr et al. “A quantum gas microscope for detecting single atoms in a Hubbard-regime optical lattice”. In: *Nature* 462 (7269 2009), pp. 74–77 (cit. on p. 2).

[6] J. W. Britton et al. “Engineered two-dimensional Ising interactions in a trapped-ion quantum simulator with hundreds of spins”. In: *Nature* 484 (7395 2012) (cit. on p. 2).

[7] C. Weisbuch et al. “Observation of the coupled exciton-photon mode splitting in a semiconductor quantum microcavity”. In: *Phys. Rev. Lett.* 69 (23 Dec. 1992), pp. 3314–3317. DOI: 10.1103/PhysRevLett.69.3314 (cit. on pp. 2, 6, 40, 69).

[8] I. Carusotto and C. Ciuti. “Quantum fluids of light”. In: *Rev. Mod. Phys.* 85 (1 Feb. 2013), pp. 299–366. DOI: 10.1103/RevModPhys.85.299 (cit. on pp. 2, 3, 36, 38, 42, 43, 45, 50).

[9] J. Kasprzak et al. “Bose-Einstein condensation of exciton polaritons”. In: *Nature* 443 (7110 2006). ISSN: 0028-0836 (cit. on p. 2).

[10] J. D. Plumhof et al. “Room-temperature Bose–Einstein condensation of cavity exciton–polaritons in a polymer”. In: *Nature Materials* 13 (3 2014). ISSN: 1476-1122 (cit. on p. 2).

[11] A. Amo et al. “Superfluidity of polaritons in semiconductor microcavities”. In: *Nature Physics* 5 (11 2009). ISSN: 1745-2473 (cit. on p. 2).

[12] M. Milićević et al. “Edge states in polariton honeycomb lattices”. In: *2D Materials* 2.3 (2015), p. 034012 (cit. on p. 2).

[13] G. Nardin et al. “Hydrodynamic nucleation of quantized vortex pairs in a polariton quantum fluid”. In: *Nature Physics* 7 (8 2011). ISSN: 1745-2473 (cit. on p. 2).

[14] A. Amo et al. “Polariton Superfluids Reveal Quantum Hydrodynamic Solitons”. In: *Science* 332.6034 (2011), pp. 1167–1170. ISSN: 0036-8075. DOI: 10.1126/science.1202307. eprint: http://science.sciencemag.org/content/332/6034/1167.full.pdf (cit. on p. 2).

[15] M. Sich et al. “Observation of bright polariton solitons in a semiconductor microcavity”. In: *Nature Photonics* 6 (1 2011). ISSN: 1749-4885 (cit. on p. 2).

[16] C. Leyder et al. “Observation of the optical spin Hall effect”. In: *Nature Physics* 3 (9 2007). ISSN: 1745-2473 (cit. on p. 2).

[17] A. Kavokin, G. Malpuech, and M. Glazov. “Optical Spin Hall Effect”. In: *Phys. Rev. Lett.* 95 (13 Sept. 2005), p. 136601. DOI: 10.1103/PhysRevLett.95.136601 (cit. on p. 2).

[18] P. G. Savvidis et al. “Angle-Resonant Stimulated Polariton Amplifier”. In: *Phys. Rev. Lett.* 84 (7 Feb. 2000), pp. 1547–1550. DOI: 10.1103/PhysRevLett.84.1547 (cit. on pp. 3, 94, 116).

[19] R. M. Stevenson et al. “Continuous Wave Observation of Massive Polariton Redistribution by Stimulated Scattering in Semiconductor Microcavities”. In: *Phys. Rev. Lett.* 85 (17 2000), pp. 3680–3683. DOI: 10.1103/PhysRevLett.85.3680 (cit. on pp. 3, 94, 116).

[20] L. Ferrier et al. “Polariton parametric oscillation in a single micropillar cavity”. In: *Applied Physics Letters* 97.3, 031105 (2010). DOI: http://dx.doi.org/10.1063/1.3466902 (cit. on pp. 3, 94, 116).

[21] C. Diederichs et al. “Parametric oscillation in vertical triple microcavities”. In: *Nature* 440.7086 (2006), pp. 904–907 (cit. on pp. 3, 94, 116).

[22] J. P. Karr et al. “Squeezing in semiconductor microcavities in the strong-coupling regime”. In: *Phys. Rev. A* 69 (3 Mar. 2004), p. 031802. DOI: 10.1103/PhysRevA.69.031802 (cit. on p. 3).

[23] T. Boulier et al. “Polariton-generated intensity squeezing in semiconductor micropillars”. In: *Nature Communications* 5 (2014) (cit. on p. 3).

[24] A. Baas et al. “Optical bistability in semiconductor microcavities in the nondegenerate parametric oscillation regime: Analogy with the optical parametric oscillator”. In: *Phys. Rev. B* 70 (16 Oct. 2004), p. 161307. DOI: 10.1103/PhysRevB.70.161307 (cit. on p. 3).

[25] S. R. K. Rodriguez et al. “Interaction-induced hopping phase in driven-dissipative coupled photonic microcavities”. In: *Nature Communications* 7 (12 2016), p. 125324 (cit. on pp. 3, 93, 111, 114).

[26] T. C. H. Liew and V. Savona. “Single Photons from Coupled Quantum Modes”. In: *Phys. Rev. Lett.* 104 (18 May 2010), p. 183601. DOI: 10.1103/PhysRevLett.104.183601 (cit. on pp. 3, 65, 91).

[27] M. Bamba and C. Ciuti. “Counter-polarized single-photon generation from the auxiliary cavity of a weakly nonlinear photonic molecule”. In: *Applied Physics Letters* 99.17 (2011). DOI: http://dx.doi.org/10.1063/1.3656250 (cit. on pp. 3, 65, 91).

[28] L. S. Collaboration and V. Collaboration. “GW151226: Observation of Gravitational Waves from a 22-Solar-Mass Binary Black Hole Coalescence”. In: *Phys. Rev. Lett.* 116 (24 June 2016), p. 241103. DOI: 10.1103/PhysRevLett.116.241103 (cit. on p. 5).

[29] C. Cohen-Tannoudji, B. Diu, and F. Laloe. “Mécanique quantique Tome 2.” In: Hermann, 1997 (cit. on p. 6).

[30] R. J. Thompson, G. Rempe, and H. J. Kimble. “Observation of normal-mode splitting for an atom in an optical cavity”. In: *Phys. Rev. Lett.* 68 (8 Feb. 1992), pp. 1132–1135. DOI: 10.1103/PhysRevLett.68.1132 (cit. on p. 6).

[31] L. Novotny. “Strong coupling, energy splitting, and level crossings: A classical perspective”. In: *American Journal of Physics* 78.11 (2010), pp. 1199–1202. DOI: http://dx.doi.org/10.1119/1.3471177 (cit. on p. 7).

[32] L. C. Andreani. “Exciton-polaritons in bulk semiconductors and in confined electron and photon systems”. In: Singapore: World Scientific, 2013 (cit. on pp. 7, 37).

[33] S. R.-K. Rodriguez. “Classical and quantum distinctions between weak and strong coupling”. In: *European Journal of Physics* 37.2 (2016), p. 025802 (cit. on p. 7).

[34] K. B. Lipkowitz et al. “Kohn-Sham Density Functional Theory: Predicting and Understanding Chemistry”. In: vol. 15. Wiley Online Library, 2007 (cit. on p. 17).

[35] P. Y. Yu and M. Cardona. “Foundamentals of Semiconductors”. In: Springer-Verlag Berlin, Heidelberg, New York, 2001 (cit. on pp. 17–20, 23–25).

[36] S. Richard, F. Aniel, and G. Fishman. “Energy-band structure of Ge, Si, and GaAs: A thirty-band $\mathbf{k}\cdot\mathbf{p}$ method”. In: *Phys. Rev. B* 70 (23 Dec. 2004), p. 235204. DOI: 10.1103/PhysRevB.70.235204 (cit. on pp. 19, 20).

[37] K. H. Goetz et al. “Optical and crystallographic properties and impurity incorporation of InGaAs grown by liquid phase epitaxy, vapor phase epitaxy, and metal organic chemical vapor deposition”. In: *Journal of Applied Physics* 54.8 (1983), pp. 4543–4552. DOI: http://dx.doi.org/10.1063/1.332655 (cit. on p. 19).

[38] G. Bastard et al. “Exciton binding energy in quantum wells”. In: *Phys. Rev. B* 26 (4 Aug. 1982), pp. 1974–1979. DOI: 10.1103/PhysRevB.26.1974 (cit. on p. 27).

[39] J. D. Joannopoulos et al. *Photonic crystals: molding the flow of light*. Princeton university press, 2011 (cit. on p. 29).

[40] M. A. Afromowitz. “Refractive index of GaAlAs”. In: *Solid State Communications* 15.1 (1974), pp. 59–63. ISSN: 0038-1098. DOI: http://dx.doi.org/10.1016/0038-1098(74)90014-3 (cit. on p. 32).

[41] G. Bastard. *Wave mechanics applied to semiconductor heterostructures*. New York, NY (USA); John Wiley and Sons Inc., 1990 (cit. on pp. 38, 54).

[42] V. Savona et al. “Optical properties of microcavity polaritons”. In: *Phase Transitions* 68.1 (1999), pp. 169–279. DOI: 10.1080/01411599908224518 (cit. on pp. 38, 43).

[43] J. J. Hopfield. “Theory of the Contribution of Excitons to the Complex Dielectric Constant of Crystals”. In: *Phys. Rev.* 112 (5 Dec. 1958), pp. 1555–1567. DOI: 10.1103/PhysRev.112.1555 (cit. on p. 40).

[44] M. Combescot, M. A. Dupertuis, and O. Betbeder-Matibet. “Polariton-polariton scattering: Exact results through a novel approach”. In: *EPL (Europhysics Letters)* 79.1 (2007), p. 17001 (cit. on pp. 44, 45, 117).

[45] M. M. Glazov et al. “Polariton-polariton scattering in microcavities: A microscopic theory”. In: *Phys. Rev. B* 80 (15 Oct. 2009), p. 155306. DOI: 10.1103/PhysRevB.80.155306 (cit. on pp. 45, 117, 122).

[46] M. Vladimirova et al. “Polariton-polariton interaction constants in microcavities”. In: *Phys. Rev. B* 82 (7 Aug. 2010), p. 075301. DOI: 10.1103/PhysRevB.82.075301 (cit. on pp. 45, 117).

[47] U. Weiss. *Quantum dissipative systems*. Vol. 10. World Scientific, 1999 (cit. on p. 50).

[48] A. Cho and J. Arthur. “Molecular beam epitaxy”. In: *Progress in Solid State Chemistry* 10 (1975), pp. 157–191. ISSN: 0079-6786. DOI: http://dx.doi.org/10.1016/0079-6786(75)90005-9 (cit. on p. 54).

[49] E. Wertz et al. “Spontaneous formation and optical manipulation of extended polariton condensates”. In: *Nature Physics* 6 (11 1975), pp. 860–864. ISSN: 1745-2473. DOI: http://dx.doi.org/10.1038/nphys1750 (cit. on p. 57).

[50] C. Cohen-Tannoudji, B. Diu, and F. Laloe. “Mécanique quantique Tome 1.” In: Hermann, 1997 (cit. on p. 72).

[51] V. G. Sala et al. “Spin-Orbit Coupling for Photons and Polaritons in Microstructures”. In: *Phys. Rev. X* 5 (1 Mar. 2015), p. 011034. DOI: 10.1103/PhysRevX.5.011034 (cit. on p. 78).

[52] Y. Varshni. "Temperature dependence of the energy gap in semiconductors". In: *Physica* 34.1 (1967), pp. 149–154. ISSN: 0031-8914. DOI: http://dx.doi.org/10.1016/0031-8914(67)90062-6 (cit. on pp. 81, 84).

[53] G. Perna et al. "Temperature dependence of the red shift and broadening of the exciton line in CdSe/GaAs laser ablated heterostructures". In: *Journal of Luminescence* 76 (1998), pp. 534–539. DOI: 10.1016/S0022-2313(97)00291-3 (cit. on pp. 81, 84, 85).

[54] N. Ravindra, P. Ganapathy, and J. Choi. "Energy gap refractive index relations in semiconductors - An overview". In: *Infrared physics & technology* 50.1 (2007), pp. 21–29 (cit. on pp. 81, 83, 84).

[55] S. Rudin and T. L. Reinecke. "Temperature-dependent exciton linewidths in semiconductor quantum wells". In: *Phys. Rev. B* 41 (5 Feb. 1990), pp. 3017–3027. DOI: 10.1103/PhysRevB.41.3017 (cit. on pp. 81, 85).

[56] V. Srinivas et al. "Intrinsic linewidths and radiative lifetimes of free excitons in GaAs quantum wells". In: *Phys. Rev. B* 46 (16 Oct. 1992), pp. 10193–10196. DOI: 10.1103/PhysRevB.46.10193 (cit. on pp. 81, 85).

[57] S. Logothetidis et al. "Temperature dependence of the dielectric function and the interband critical points of CdSe". In: *Phys. Rev. B* 34 (4 Aug. 1986), pp. 2458–2469. DOI: 10.1103/PhysRevB.34.2458 (cit. on p. 84).

[58] D. Sarchi et al. "Coherent dynamics and parametric instabilities of microcavity polaritons in double-well systems". In: *Phys. Rev. B* 77 (12 Mar. 2008), p. 125324. DOI: 10.1103/PhysRevB.77.125324 (cit. on pp. 93, 103, 109, 113, 115).

[59] M. . Skolnick et al. "Polariton–polariton interactions and stimulated scattering in semiconductor microcavities". In: *Materials Science and Engineering: C* 19.1 (2002), pp. 407–416 (cit. on pp. 94, 116).

[60] S. Michaelis de Vasconcellos et al. "Spatial, spectral, and polarization properties of coupled micropillar cavities". In: *Applied Physics Letters* 99.10, 101103 (2011). DOI: http://dx.doi.org/10.1063/1.3632111 (cit. on p. 101).

[61] G. J. Milburn et al. "Quantum dynamics of an atomic Bose-Einstein condensate in a double-well potential". In: *Phys. Rev. A* 55 (6 June 1997), pp. 4318–4324. DOI: 10.1103/PhysRevA.55.4318 (cit. on p. 103).

[62] P. N. Butcher and D. Cotter. *The Elements of Nonlinear Optics:* Cambridge Studies in Modern Optics. Cambridge University Press, July 1990. ISBN: 9781139167994. DOI: 10.1017/CBO9781139167994 (cit. on p. 110).

[63] L. A. Lugiato et al. "Modulational instabilities and cavity solitons in semiconductor microcavities". In: *Journal of Optics B: Quantum and Semiclassical Optics* 1.1 (1999), p. 43 (cit. on p. 110).

[64] I. Carusotto and G. L. Rocca. “Nonlinear optics of coupled semiconductor microcavities”. In: *Physics Letters A* 243.4 (1998), pp. 236–242. ISSN: 0375-9601. DOI: http://dx.doi.org/10.1016/S0375-9601(98)00230-8 (cit. on p. 110).

[65] J. A. Giordmaine and R. C. Miller. “Tunable Coherent Parametric Oscillation in $LiNbO_3$ at Optical Frequencies”. In: *Phys. Rev. Lett.* 14 (24 June 1965), pp. 973–976. DOI: 10.1103/PhysRevLett.14.973 (cit. on p. 116).

[66] T. Lecomte et al. “Polariton-polariton interaction potentials determination by pump-probe degenerate scattering in a multiple microcavity”. In: *Phys. Rev. B* 89 (15 Apr. 2014), p. 155308. DOI: 10.1103/PhysRevB.89.155308 (cit. on p. 117).

[67] C. Ciuti et al. “Role of the exchange of carriers in elastic exciton-exciton scattering in quantum wells”. In: *Phys. Rev. B* 58 (12 Sept. 1998), pp. 7926–7933. DOI: 10.1103/PhysRevB.58.7926 (cit. on pp. 117, 120, 122).